CORA Cork Open Research Archive
Cartlann Taighde Oscailte Chorcaí

Title	Fabrication and characterisation of semiconductor nanowires and metal interconnects
Authors	O'Regan, Colm
Publication date	2013
Original Citation	O'Regan, C. P. 2013. Fabrication and characterisation of semiconductor nanowires and metal interconnects. PhD Thesis, University College Cork.
Type of publication	Doctoral thesis
Rights	© 2013, Colm P. O'Regan - http://creativecommons.org/licenses/by-nc-nd/3.0/
Download date	2026-11-17 04:43:30
Item downloaded from	https://hdl.handle.net/10468/1378



UCC
University College Cork, Ireland
Coláiste na hOllscoile Corcaigh

Fabrication and Characterisation of Semiconductor Nanowires and Metal Interconnects

Colm Patrick O'Regan, B.Sc. (Hons.)

Department of Chemistry

University College Cork, Ireland
Coláiste na hOllscoile Corcaigh

University College Cork

Ireland

Presented for the degree of Doctor of Philosophy to the National University of Ireland

Supervisors: Prof. Justin D. Holmes

Dr. Nikolay Petkov

Head of Department: Prof. Michael A. Morris

September 2013

I, Colm Patrick O’Regan, certify that this Thesis is my own work and I have not obtained a degree in this University, or elsewhere, on the basis of this thesis.

_____

Colm Patrick O’Regan

Abstract

One-dimensional semiconductor nanowires are considered to be promising materials for future nanoelectronic applications. However, before these nanowires can be integrated into such applications, a thorough understanding of their growth behaviour is necessary. In particular, methods that allow the control over nanowire growth are deemed especially important as it is these methods that will enable the control of nanowire dimensions such as length and diameter (high aspect ratios). The production of nanowires with high-aspect ratios is vital in order to take advantage of the unique properties experienced at the nanoscale, thus allowing us to maximise their use in devices. Additionally, the development of low-resistivity interconnects is desirable in order to connect such nanowires in multi-nanowire components. Consequently, this thesis aims to discuss the synthesis and characterisation of germanium (Ge) nanowires and platinum (Pt) interconnects. Particular emphasis is placed on manipulating the nanowire growth kinetics to produce high aspect ratio structures. The discussion of Pt interconnects focuses on the development of low-resistivity devices and the electrical and structural analysis of those devices.

Chapter 1 reviews the most critical aspects of Ge nanowire growth which must be understood before they can be integrated into future nanodevices. These features include the synthetic methods employed to grow Ge nanowires, the kinetic and thermodynamic aspects of their growth and nanowire morphology control.

Chapter 2 outlines the experimental methods used to synthesise and characterise Ge nanowires as well as the methods used to fabricate and analyse Pt interconnects.

Chapter 3 discusses the control of Ge nanowire growth kinetics via the manipulation of the supersaturation of Ge in the Au/Ge binary alloy system. This is accomplished through the use of bi-layer films, which pre-form Au/Ge alloy catalysts before the introduction of the Ge precursor. The growth from these catalysts is then compared with Ge nanowire growth from standard elemental Au seeds. Nanowires grown from pre-formed Au/Ge alloy seeds demonstrate longer lengths and higher growth rates than those grown from standard Au seeds. In-situ TEM heating on the Au/Ge bi-layer films is used to support the growth characteristics observed.

Chapter 4 extends the work of chapter 3 by utilising Au/Ag/Ge tri-layer films to enhance the growth rates and lengths of Ge nanowires. These nanowires are grown from Au/Ag/Ge ternary alloy catalysts. Once again, the supersaturation is influenced, only this time it is through the simultaneous manipulation of both the solute concentration and equilibrium concentration of Ge in the Au/Ag/Ge ternary alloy system. The introduction of Ag to the Au/Ge binary alloy lowers the equilibrium concentration, thus increasing the nanowire growth rate and length. Nanowires with uniform diameters were obtained via synthesis from Au_xAg_{1-x} alloy nanoparticles. Manifestation of the Gibbs-Thomson effect, resulting from the dependence of the mean nanowire length as a function of diameter, was observed for all of the nanowires grown from the Au_xAg_{1-x} nanoparticles. Finally, in-situ TEM heating was used to support the nanowire growth characteristics.

Chapter 5 details the fabrication and characterisation of Pt interconnects deposited by electron beam induced deposition of two different precursors. The fabrication is conducted inside a dual beam FIB. The electrical and structural characteristics of interconnects deposited from a standard organometallic precursor and a novel carbon-free precursor are compared. The electrical performance of the carbon-free interconnects is shown to be superior to that of the organometallic devices and this is correlated to the structural composition of both interconnects via in-situ TEM heating and HAADF-STEM analysis. Annealing of the interconnects is carried out under two different atmospheres in order to reduce the electrical resistivity even further.

Finally, chapter 6 presents some important conclusions and summarises each of the previous chapters.

Acknowledgments

First and foremost, I would like to thank my supervisors Justin Holmes and Nikolay Petkov for allowing me the opportunity to work in such an exciting area of science. I realise opportunities like this are rare, and even scarcer are supervisors with the talent and skills to guide someone through a PhD relatively unscathed. I have heard horror stories of students with supervisors who don't keep up to date with their work, who don't publish and who require years of slavery before being finally awarding the doctorate. Therefore, I consider myself very fortunate (and a little lucky) to have worked for Justin and Nikolay. Thank you.

Additionally, sincere gratitude must go to the guys who helped me through the difficult times and guided my research to make sure I actually finished on time! I would like to thank Richard Hobbs for always lending a helping hand (before and during my PhD), even though he had no obligation to do so. Gratitude must also go to Sven for introducing me to the field of nanowires and the very awkward supercritical fluid method. Mostly however, I should thank him for his patience, as unlike Richard, he was very much obliged to put up with me during that tedious first year. Most importantly, I would like to thank Subhajit for his guidance during the majority of my studies and without whom, I probably would have had a much rougher time of it. Thank you Subha!

On the microscopy side, I would like to express my thanks to Nikolay (again), Michael and Pat for their exceptional training on the TEM, SEM and FIB. A group is only as good as its characterization and analysis staff and the EMAF lads are outstanding in this field. My interest in TEM specifically was fostered as a direct result of being around these very talented individuals.

The lads who I started with in lab 115 helped me transition smoothly into the sometimes turbulent world of postgraduate research and to them, I am grateful. Justin, JV, Gill, Keith, Paul, Dave, Kamil, Sven, Tim, Mark, Richard, Ritchie Phelan, Ciara, Arun, John O'Callaghan and Olan, you guys were a laugh and I couldn't think of a better group to be a part of. To the guys who came after: John, Subha, Angelica, Brenda, Ritchie Farrell, Colm, Elaine, and Mike, you made sure the banter kept flowing. Thanks for the good times!

The lads upstairs gave us a good run for our money, making sure our regular coffee breaks were never boring: Tandra, Pete, Tom, Eile, Raj, Atul, Atul eile, Sankar, Dipu, Hugh, Will, Cian, Eileen, Ivan, Elsa, Charlie, Parvaneh, Ben and Tim. Thanks guys!

A special thanks must also go to my fellow Tyndall mates; Roisin, Yordan, Anushka and Barbara along with the dudes from the ERI: Joe, Paul (again) and Eoin.

To everyone who I've worked with in the chemistry department: Chrissie, Tina, Johnny, Mick, Tony and Matty, I would like to thank you guys for providing an immensely enjoyable work environment. A long overdue thank you must go to Terry, who was always up for some mischief and always seemed to be in a festive mood! The banter won't be forgotten Terry!

Finally, profound gratitude must go to my parents, Pat and Genie, whos guidance and support over the last 4 years I can never repay.

Dedicated to my parents, Pat and Genie

Table of Contents

Declaration ii

Abstract iii

Acknowledgments v

Table of contents..... viii

Chapter 1 Recent Advances in the Growth of Germanium Nanowires: Synthesis, Growth Dynamics and Morphology Control 1

1.1 Abstract.....2

1.2 Introduction……..3

1.2.1 Nanotechnology……...3

1.2.2 Top-down and Bottom-up Approaches……...5

1.2.3 One-dimensional Semiconductors and Quantum Confinement……..7

1.3 Nanowire Synthesis……..9

1.3.1 Seeded Growth in Vapour and Liquid Media……...10

1.3.2 Alternative Catalysts for Metal Assisted Nanowire Growth…….18

1.3.3 Seedless and Self-seeded Nanowire Growth…….21

1.3.4 Nanowire Synthesis Outlook…….24

1.4 Kinetics and Thermodynamics of Ge Nanowire Growth……...25

1.4.1 The Au/Ge System……25

1.4.2 Thermodynamic Considerations……28

1.4.3 Kinetic Considerations……..34

1.5 Morphology Control in Ge Nanowires…….39

1.5.1 Diameter and Length Control……41

1.5.2 Growth Orientation……43

1.5.3 Heterostructures……45

1.6 Conclusion and Outlook…….48

1.7 References……...51

Chapter 2 Experimental Methods……...66

2.1 Synthesis of Ge Nanowires from Bilayer Films……...67

2.1.1 Si Substrates and Preparation of Diphenylgermane Solution……67

2.1.2 Germanium Nanowire Synthesis……...67

2.1.3 Electron Microscopy Characterisation of Germanium Nanowires……..….69

2.2 Synthesis of Ge Nanowires from Evaporated Films……70

2.2.1 Evaporation of Au, Ag and Ge Films……70

2.2.2 Preparation of Au and $Au_{0.75}Ag_{0.25}$ Particles……70

2.2.3 Electron Microscopy Characterisation of Germanium Nanowires……71

2.3 Pt Interconnect Deposition……72

2.3.1 Rapid Thermal Annealing……73

2.3.2 Electrical Characterisation……73

2.4 References……...75

Chapter 3 - Engineering the Growth of Germanium Nanowires by Tuning the Supersaturation of Au/Ge Binary Alloy Catalysts……...76

3.1 Abstract……...77

3.2 Introduction……78

3.3 Results and Discussion……...80

3.3.1 The Use of Bi-layer Films to Influence Ge Nanowire Growth……81

3.3.2 SEM and TEM Characterization……...83

3.3.3 Kinetic Studies of Ge Nanowires……..88

3.3.4 In-situ TEM Studies of Bi-layer Films……..98

3.4 Conclusion……105

3.6 References……106

Chapter 4 – Controlled Growth of Germanium Nanowires from Ternary Alloy Catalysts……109

4.1 Abstract……110

4.2 Introduction……111

4.3 Results and Discussion……114

4.3.1 Growth of Ge Nanowires from Au/Ag/Ge Tri-layer Films……114

4.3.2 Manipulation of the Equilibrium Concentration……118

4.3.3 Simultaneous Manipulation of both Solute and Equilibrium Concentration……120

4.3.4 Growth of Ge Nanowires from Au_xAg_{1-x} Nanoparticles……122

4.3.5 Diameter Dependent Studies and the Gibbs-Thomson Effect……130

4.3.6 In-situ TEM Heating and the Gibbs-Thomson Effect……132

4.4 Conclusions……137

4.5 References……138

Chapter 5 - Electrical Properties of Platinum Interconnects Deposited by Electron Beam Induced Deposition of the Carbon-free Precursor, $Pt(PF_3)_4$……141

5.1 Abstract……142

5.2 Introduction……143

5.3 Results and Discussion……146

5.3.1 Pt Interconnect Deposition and Initial Electrical Characterization……146

5.3.2 Maximum Current Density Measurements……151

5.3.3 Annealing Studies under Nitrogen on Deposited Pt……152

5.3.4 Annealing Studies under Forming Gas……153

5.3.5 Elemental and Compositional Analysis of the Carbon-free Pt……157

5.4 Conclusions……166

5.5 References……167

Chapter 6 Conclusions……..171

References……..176

Appendix: Dissemination…….178

Appendix 2: Calculation of Ge atomic %……...182

Real knowledge is to know the extent of one's ignorance

- Confucius

Recent Advances in the Growth of Germanium Nanowires: Synthesis, Growth Dynamics and Morphology Control

1

[This chapter has been published as a peer-reviewed article in the Journal of Materials Chemistry C. Consequently, certain sections of the chapter such as the abstract and introduction may contain repeating paragraphs and concepts]

O'Regan, C.; Biswas, S.; Petkov, N.; Holmes, J.D. (2013) ***J. Mater. Chem. C****, DOI: 10.1039/C3TC31736F*

1.1 Abstract

One-dimensional semiconductor nanostructures have been studied in great depth over the past number of decades as potential building blocks in electronic, thermoelectric, optoelectronic, photovoltaic and battery devices. Silicon has been the material of choice in several industries, in particular the semiconductor industry, for the last few decades due to its stable oxide and well documented properties. Recently however, Ge has been proposed as a candidate to replace Si in microelectronic devices due to its high charge carrier mobilities. A number of various 'bottom-up' synthetic methodologies have been employed to grow Ge nanowires, including chemical vapour deposition, thermal evaporation, template methods, supercritical fluid synthesis, molecular beam epitaxy and solution phase synthesis. These bottom-up methods afford the opportunity to produce commercial scale quantities of nanowires with controllable lengths, diameters and crystal structure. An understanding of the vapour-liquid-solid (VLS) and vapour-solid-solid (VSS) mechanism by which most Ge nanowires are produced, is key to controlling their growth rate, aspect ratio and morphology. This chapter highlights the various bottom-up growth methods that have been used to synthesise Ge nanowires over the past 5-6 years, with particular emphasis on the Au/Ge eutectic system and the VLS mechanism. Thermodynamic and kinetic models used to describe Ge nanowire growth and morphology control will also be discussed in detail.

1.2 Introduction

1.2.1 Nanotechnology

Nanotechnology is rapidly becoming one of the leading topics in scientific research today. Ever since Richard Feynman gave his famous talk "There's plenty of room at the bottom"[1] in 1959, scientists have been discussing a future where they would be able to manipulate and control materials on a tiny scale. Today, Feynman's proposed future has become a reality with nanoscale structures being designed and controlled via top-down lithographical methods and bottom-up self-assembly techniques. The time when the word "nano" was just a scientific theory has passed and nowadays the term has entered the micro-industrial consciousness and public perception. With nanotechnology affecting and influencing the lives of almost everyone, it is no surprise that it has generated widespread acclaim.

The radically different properties that materials exhibit on the nanoscale (as opposed to their bulk counterparts) have generated a great deal of interest from researchers worldwide. This is due, in part, to the quantum confinement effects and their potential in nanoelectronic devices. Chemists and physicists are continually looking for new ways to shrink nanomaterials down to smaller sizes in order to take advantage of these effects. Nowhere is this more evident than in the micro-electronics industry where the number of transistors being placed on a silicon chip is ever increasing. This is in accordance with Moore's law which simply states that the number of transistors per chip doubles every 18 months [2] , see figure 1.1.

As transistor sizes continue to decrease, top-down lithographical techniques are becoming increasingly problematic due to physical limitations. Hence the next few years will see a large increase in the research being carried out into various bottom-up techniques. Not only will this help reduce the cost of chip manufacture but it will also aid in solving the problem of size limitation [3].

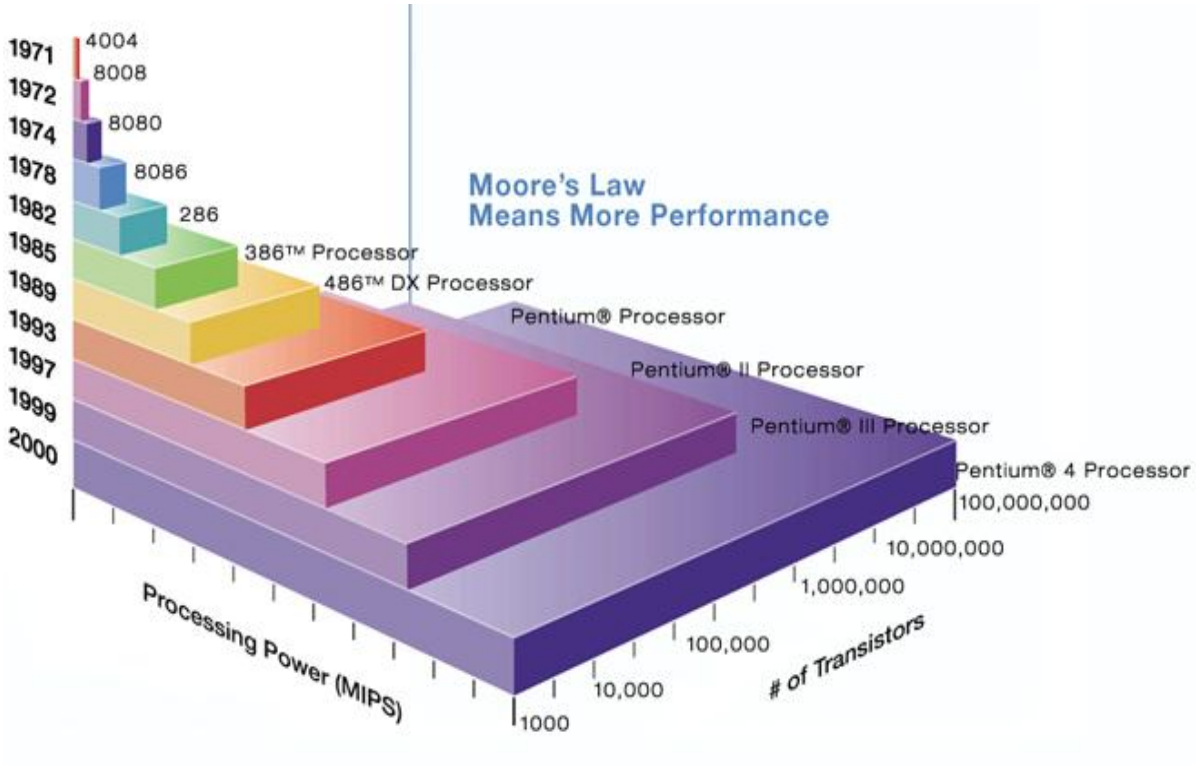


Figure 1.1 Graphical representation of Moore's law showing the increase in number of transistors being placed on computer chips [2, 4].

1.2.2 Top-down and Bottom-up Approaches

The various synthetic methods of growing nanomaterials such as nanowires can be grouped into the two broad categories of top-down and bottom-up [5]. The earliest methods used a top-down approach and include techniques such as optical and electron beam lithography, which use electron or ion beams to mill or pattern a substrate. Everything that isn't needed is etched away resulting in the desired nanomaterial.

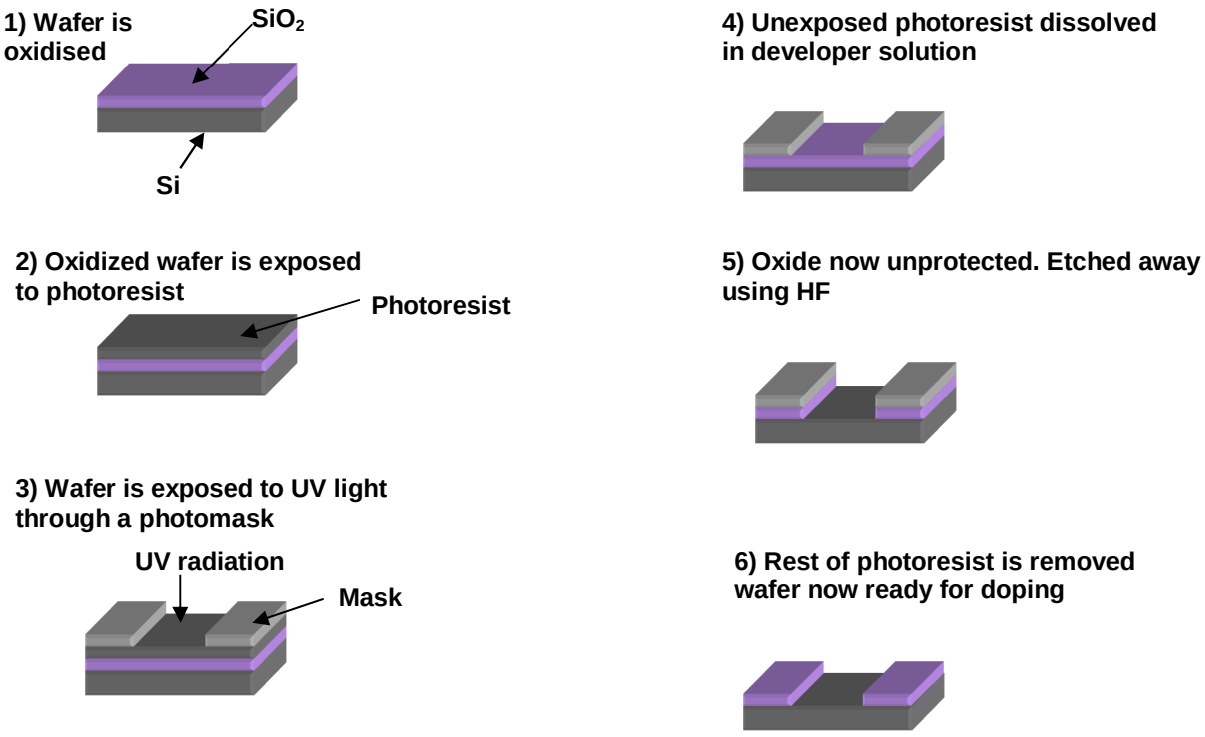


Figure 1.2 Top-down fabrication of a transistor

Transistor devices such as MOSFETS are examples of materials produced using this method, as illustrated in figure 1.3 below. However, while top-down lithographic methods remain synthetically useful processes, the continued miniaturisation of components and nanomaterials presents certain problems in the form of economic

and physical limitations. Taking the MOSFET as an example, the continued down-scaling of components will eventually result in the gate dielectric becoming so thin that quantum mechanical tunnelling of electrons will take place. The gate will stop acting like an insulator and will start leaking current, lowering efficiency and wasting energy. Currently, Si MOSFETS are scaled to the 32 nm node with gate lengths of 25-30 nm [6]. Another major issue with top-down methods is the imperfection of the surface structure and the defects that are generated during the process [7].

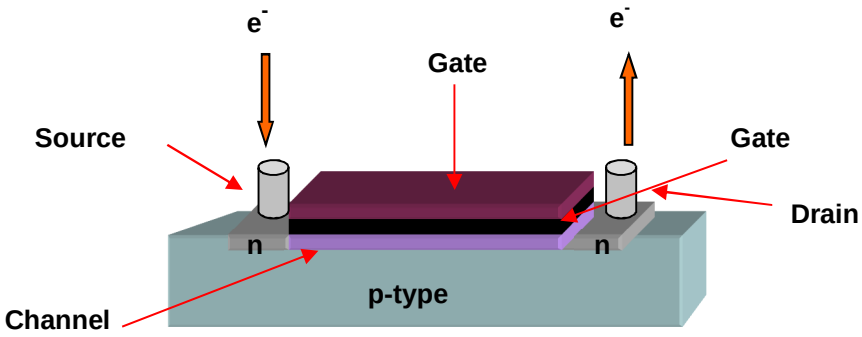


Figure 1.3 Schematic of a MOSFET structure

A lot of research has been carried out in an effort to solve this problem at the cost of much time and expense. A more viable and cost-effective approach is to investigate what are known as bottom-up techniques to synthesise smaller and smaller nanostructures. Bottom-up techniques represent the most useful synthetic methods for the growing of nanomaterials. While top-down methods use patterning and etching to mill away at a larger substrate until the desired nanomaterial is produced, bottom-up techniques start with nothing but reactants and grow materials atom by atom. These non-lithographic techniques for growing and organising materials on the

nanoscale are required if the limitations posed by top-down techniques are to be overcome. Various methods of synthesising and self-assembling building blocks into more complex device architectures have been developed and are discussed below.

1.2.3 One-dimensional Nanostructures and Quantum Confinement

One-dimensional semiconductor nanowires have stimulated much interest in the last decade due to their potential use as building blocks for assembling nanoscale devices and architectures [8, 9]. They also possess unique properties compared to their bulk counterparts, such as quantum confinement, allowing them to be utilised in functional optoelectronic and photovoltaic devices [10, 11]. Significantly, semiconductor nanowires have already shown promise in several fields such as construction [12], energy conversion [13], electronics [8, 11, 14, 15] and photonics [16] and will likely continue to lead the way for the development of future applications. The continued miniaturisation of electronic components in accordance with Moore's Law [2, 17] and the imminent approach of device scaling limitations have made research into semiconducting nanowires even more imperative.

Silicon has been the material of choice for the microelectronics industry for the last number of decades. Hence, research into materials that are compatible with current Si-based technology is a major theme in nanoelectronics. Like Si, Ge is a Group 14 semiconductor material and as such, it shares several properties in common with Si, such as a diamond cubic crystal structure. Germanium exhibits certain properties that are superior to those of Si, including a higher charge carrier mobility [18] and a larger Bohr exciton radius at higher dimensions. For this reason, interest in Ge nanowires has flourished in the last few years[19, 20] as research groups and industry

contemplate the necessary migration away from Si in order to improve functionality in electronic devices. The material has already recently demonstrated potential in various applications such as lithium-ion batteries[21-23], field effect transistors (FETs)[24, 25], memory applications[26-28], photovoltaics[29, 30] and nanoelectromechanical systems (NEMS)[31, 32]. Ge nanowires have also been used as a means of studying dopant location [33] as well as strain [34, 35], transport modulation [36] and band offset efficiency [37] in the form of core-shell nanowires. Finally, surface effects greatly affect the nanowire properties due to the high surface to volume ratio, thus research into the functionalization of germanium nanowire surfaces [38-42] has resulted in further development and a better understanding of the potential of these materials.

Current bottom-up epitaxial growth methods make use of the classic vapour-liquid-solid (VLS) mechanism to grow one-dimensional nanostructures where a liquid catalytic seed is employed for unidirectional, diameter-controlled nanowire growth [43-48]. In order to take advantage of the unique optical and electrical properties experienced on the nanoscale, strict control over the diameter and length of semiconductor nanowires is required. This control is difficult to achieve unless colloidal metal nanoparticles/seeds with tight diameter distributions are used. Understanding the important concepts and parameters that participate in a bottom-up nanowire growth mechanism, such as nucleation, supersaturation, preferential deposition and interfacial energies, opens up the possibilities of controlling the morphology of Ge nanowires to a high degree; an obvious prerequisite if they are going to be integrated into future electronic devices. Consequently, this article aims to review the progress of Ge nanowire research over the past 5-6 years, focusing on the various methods utilised to control wire morphology and growth. A brief review

of the recent synthetic methods employed to grow Ge nanowires will also be presented. Subsequently, various mechanisms of growth will be discussed with a particular emphasis on Au/Ge eutectic alloy system.

1.3 Nanowire Synthesis

Various synthetic methods have been employed to grow one-dimensional nanowires [49, 50], the majority of which are summarised in the flow chart shown in figure 1.4. These approaches include bottom-up techniques such as metal promoted vapour phase growth, metal assisted growth in liquids, non-metal gas phase growth and template synthesis. Top-down methods, which include electron beam and focused ion beam lithography, are also commonly employed in the production of well-ordered arrays of semiconductor nanowires. This section will review the synthetic methods commonly employed to grow Ge nanowires, with a focus on the bottom-up approaches. Specifically, the most widely used catalyst-based methods carried out in vapour, liquid and supercritical media will be discussed in addition to non-catalyst assisted methods. As top-down methods have not been widely utilised to generate Ge nanowires, they will not be discussed in this review. However, a detailed discussion on the top-down fabrication of semiconductor nanowires, particularly Si, has previously been reported by Hobbs *et al.* [5].

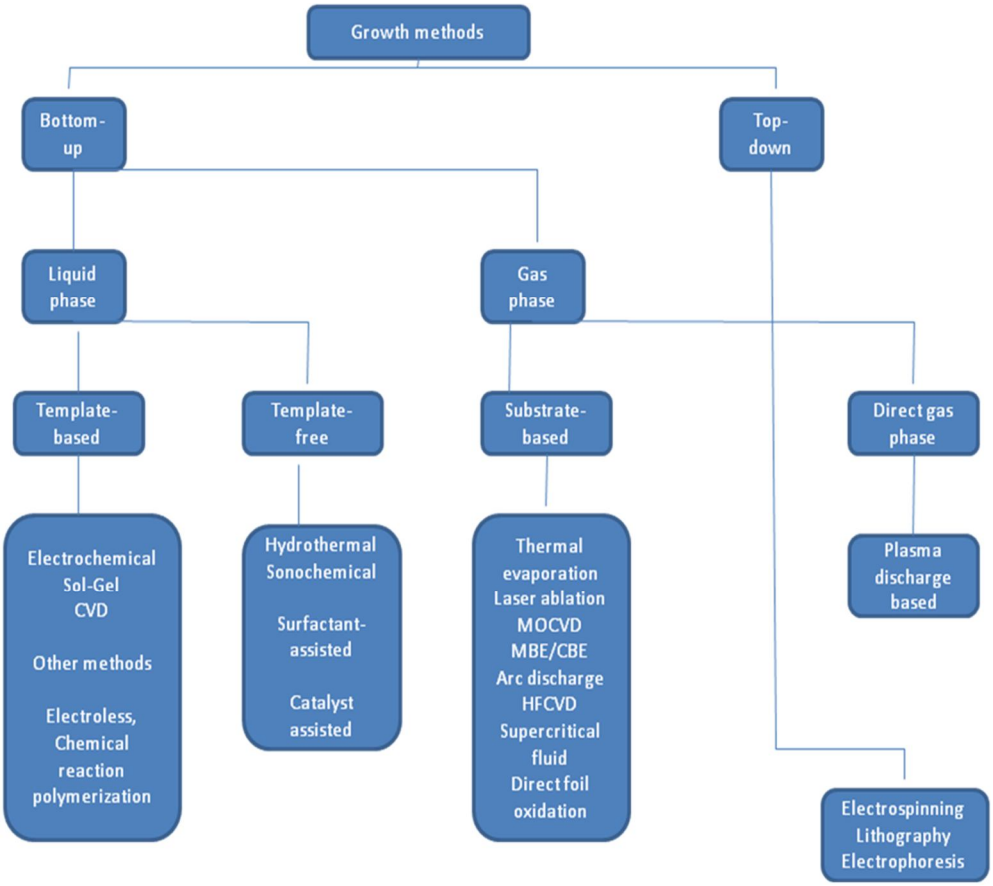


Figure 1.4 Schematic showing the various synthetic routes currently employed to grow Ge nanowires [51].

1.3.1 Seeded Growth in Vapour and Liquid Media

The most frequently used method for growing 1D semiconductor nanowires (including Ge) is the application of a metal catalyst particle in a liquid phase which promotes unidirectional growth via a three phase VLS mechanism [52] and can be performed within vapour, liquid or supercritical fluid (SCF) environments. Vapour and liquid-based growth of Ge nanowires consists of any method where the Ge precursor is in either vapour and liquid form and include techniques such as chemical vapour deposition (CVD) [53-58], metal-organic chemical vapour deposition (MOCVD) [59, 60], molecular beam epitaxy [61-63], template methods [64, 65] and various

evaporation methods such as electron beam evaporation [66, 67] and thermal evaporation [68, 69]. Alternatively, liquid/solution [21, 60, 70-75] and SCF [76-80] based methods involve the introduction of Ge precursors in liquid and supercritical media respectively. The key mechanism involved in most of these processes is analogous to the VLS mechanism first proposed by Wagner and Ellis [81] and is illustrated in figure 1.5 for the growth of Ge nanowires.

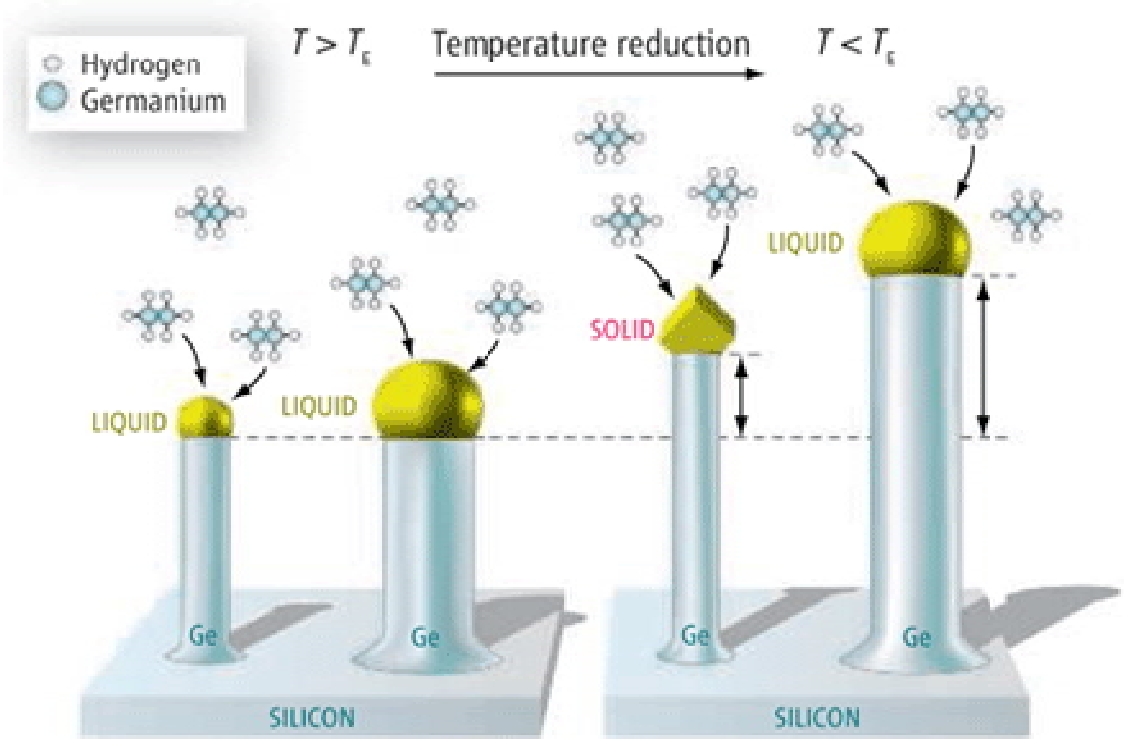


Figure 1.5 Representation of VLS and VSS mechanisms for growing GeNWs. Above the binary Au-Ge eutectic temperature (T_E, **left**), the nanowires have a liquid gold cap and grow via VLS growth. Below T_E (**right**), the cap of relatively thick nanowires is liquid, whereas the cap of relatively thin nanowires becomes a crystalline solid [82].

The VLS mechanism was based on the observations that metal impurities (seeds) were required for nanowire growth and that small amounts of the impurity were present at the tips of the wires. The diagram shown in figure 1.5 conveys the VLS and VSS (vapour-solid-solid) growth of Ge nanowires from Au seeds using a Ge_2H_6 precursor vapour. The VSS growth model will be discussed briefly in the next section. The VLS mechanism utilises liquid seeds (metal impurities) to promote nanowire growth via a supersaturation mediated process with a vapour precursor. Supersaturation, the difference in chemical potential ($\Delta\mu$) between Ge in the vapour phase and solid semiconductor phase, is the driving force behind VLS-nanowire growth; where 2D ledge nucleation at the triple phase boundary (TPB) and subsequent nanowire growth occurs when the kinetic barrier to nucleation is overcome [83]. Generally, participation of the VLS mechanism for nanowire growth can be identified in electron microscopy by the presence of a heavier seed at the tip of the nanowire, as these methods are characterized by the use of seeds to promote nanowire growth.

CVD is the most commonly employed bottom-up method used to synthesise Ge nanowires. The standard procedure is to introduce a gaseous Ge precursor, typically $GeCl_4$, GeH_4 or Ge_2H_6, into a system containing a Si substrate that has been coated with a gold film or Au nanoparticles [84-86]. A carrier gas such as H_2/Ar is employed to transport the precursor to the reaction site and to provide an oxygen free, reducing environment. Variations on the standard CVD method include using substrates other than Si, such as Ti [87], the use of alternative precursors, such as GeI_4 used to synthesise Ge-SiO_2 nanotubes [88] and the use of more complex organic based precursors to form core-shell Ge nanowires, where the monosrystalline nanowires is

encapsulated within another material [89-91]. Recently, the CVD method has been utilised in the growth of aligned endotaxial SiGe nanowires on a Si wafer [55] (see figure 1.6). Endotaxial refers to the growth of the nanowires within and along the substrate surface, resulting in pre-aligned nanowires instead of the usual entangled mesh which normally results from typical bottom-up growth. This endotaxial growth removes the need to align nanowires post-growth, an obvious prerequisite for their future integration as components in devices. One of the primary advantages of CVD is the low temperatures (typically at or below the eutectic temeperature of the binary alloy seed material) that can be employed when using metal catalytic seeds, *e.g.* Au, to synthesise Ge nanowires.

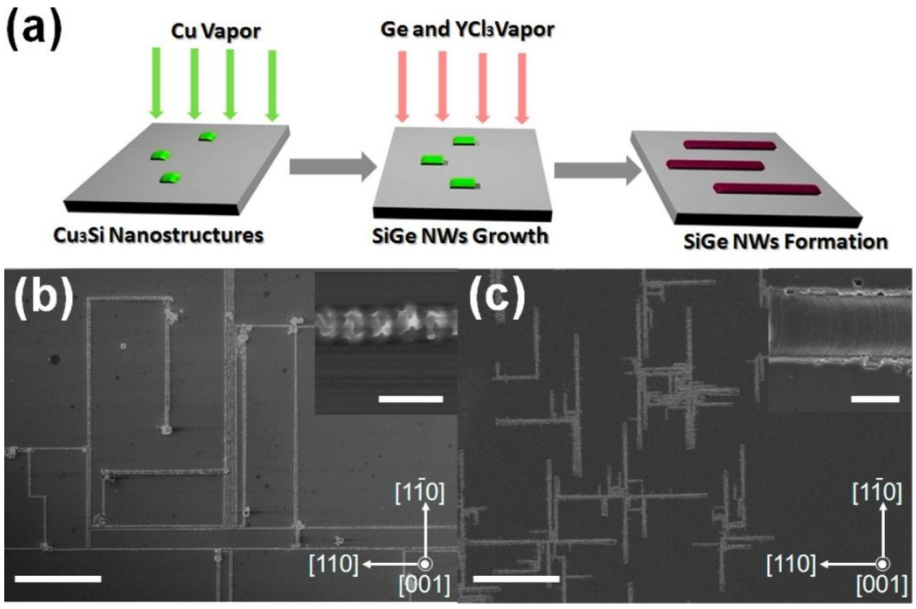


Figure 1.6 (a) Schematic illustration of the endotaxial SiGe nanowire formation process. SEM images of (b) the aligned SiGe nanowires synthesised at 720 °C on a Si wafer, where the inset shows the enlarged nanostructure, and (c) the same sample after silicate/oxide etching by HF, where the inset shows the enlarged SiGe nanowire surface. Scale bars for (b) and (c) are both 10 μm, 500 nm for the inset of (b), and 200 nm for the inset of (c) [55].

This low temperature approach is in contrast to methods such as thermal evaporation which employ very high temperatures (at least 200-300 ^{o}C) for growing Ge nanowires, a disadvantage for low-cost applications [68, 69]. By choosing suitable substrates, epitaxial approaches have been exploited to control the alignment and crystal orientation of Ge nanowires, where the nanowire growth direction matches the substrate. Molecular beam epitaxy (MBE) has been recently used to control the growth direction of Ge nanowires with great success [61, 62]. MBE is an excellent technique for the growth of nanowires as it offers ultra-high vacuum conditions (often as high as ~10^{-13} bar), precise control over morphology and composition and abrupt interfaces when compound semiconductor nanowires are synthesized. More importantly, it offers the ability to study the dynamics of nanowire growth and to control this growth at the atomic level more effectively than other techniques due to the very low growth rate (often 1 monolayer per second). This extremely low growth rate enables the investigation of the layer-by-layer growth of nanowires via the VLS mechanism, in order to gain a better understanding of the nanowire growth behaviour.

Kim *et al.* and Hawley *et al.* have achieved the epitaxial growth of Ge nanowires with CVD approaches. [57, 92] In particular, taper-free, vertically oriented Ge nanowires were realised by Kim *et al.* using a Ge buffer layer [56, 93], a two temperature process that was based on the method outlined by Greytak *et al.* [94] was used by to ensure the taper-free nature of the nanowires (see figure 1.7). Gunji *et al.* also made use of the two-temperature growth process to grow GeO_x nanowires through VLS oxidation [95]. The tapering of nanowires was also studied by Hawley *et al.* where they demonstrated control of the radial growth of Ge nanowires by

combining the well-established oxide-assisted-growth (OAG) mechanism [96, 97] with traditional CVD [92]. OAG essentially involves the evaporation and deposition of an oxide vapour to form crystalline nanowires wrapped in an amorphous oxide shell, which prevents radial growth and tapering, thus yielding nanowires with a constant diameter.

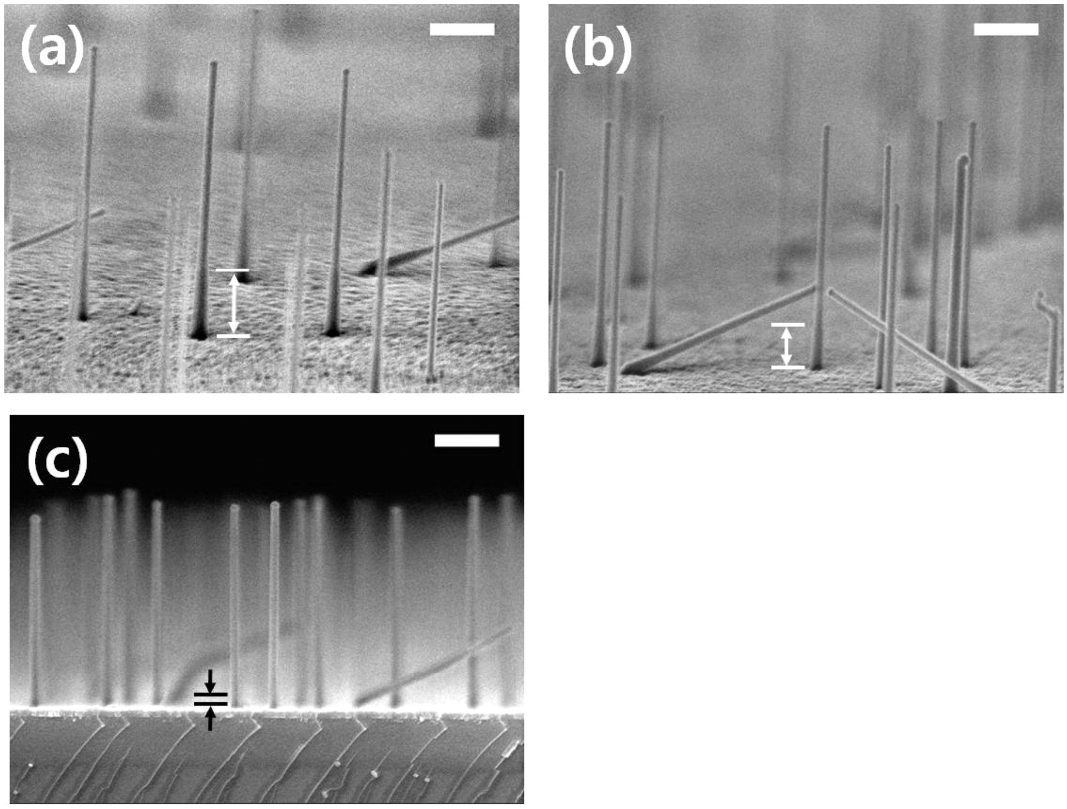


Figure 1.7 Side-view SEM images of Ge nanowires grown on a GeBSi substrate via a two-temperature process. The growth temperature during the base growth stage was 350 °C, while subsequent nanowire growth was performed at 300 °C for 20 min. The growth time during the base growth stage was: (a) 6 min, (b) 4 min and (c) 2 min. A 50 nm diameter Au colloidal solution was used. The regions marked by arrows in the SEM images are the part of nanowires grown during the base growth stage. Scale bar = 500 nm [56].

In contrast to the two-temperature method, the more facile single temperature methods have been used by Simanullang *et al.* to grow very thin (less than 5 nm) taper-free Ge nanowires [58, 98]. Vertically aligned epitaxial Ge nanowires have also

been achieved using bio-templated Au nanoparticles (NPs). The NPs were dispersed on S-layer protein templates, producing nanowires with a uniform <111> growth orientation [99]. As the (111) crystal plane has the lowest surface energy of all crystallographic orientations, Ge nanowires grow preferably along a <111> orientation on Si and Ge substrates. In contrast, nanowires with uniform <110> orientations were produced through vertical epitaxial growth on GaAs substrates from Au NPs [100]. Additionally, epitaxial growth of Ge nanowires has been achieved using methods such as electron beam evaporation [66]. As well as being able to grow aligned epitaxial nanowires with uniform crystallographic orientations, it is also highly desirable to fabricate position-controlled nanowires for device applications. Li *et al.* used top-down electron beam lithography to pattern Au catalyst particles on a SiO_2 substrate, after which they employed a CVD technique to grow Ge nanowires from a GeH_4 precursor [101].

In comparison to vapour-based methods, solution and SCF-based techniques offer promising alternatives for large-scale synthesis of Ge nanowires. Future methodologies for synthesising Ge nanowires will mostly likely comprise of solution-based techniques, as these afford large scale production of nanowires in a single reaction, as evidenced by of Yang *et al.*, who used a liquid injection technique (using several liquid precursors, including diphenylgermane) to scale-up their synthesis of Ge nanowires; producing 0.2 g of nanowires on a Si substrate [59], as shown in figure 1.8. The GeNW product was subsequently scaled up to form a 30 μm thick fabric, from 2.2 g of nanowire product, using a vacuum filtration process. Moreover, Ge nanowire fabrics have also been generated by Smith *et al.* who also investigated the plasticity and strength of the wires [102].

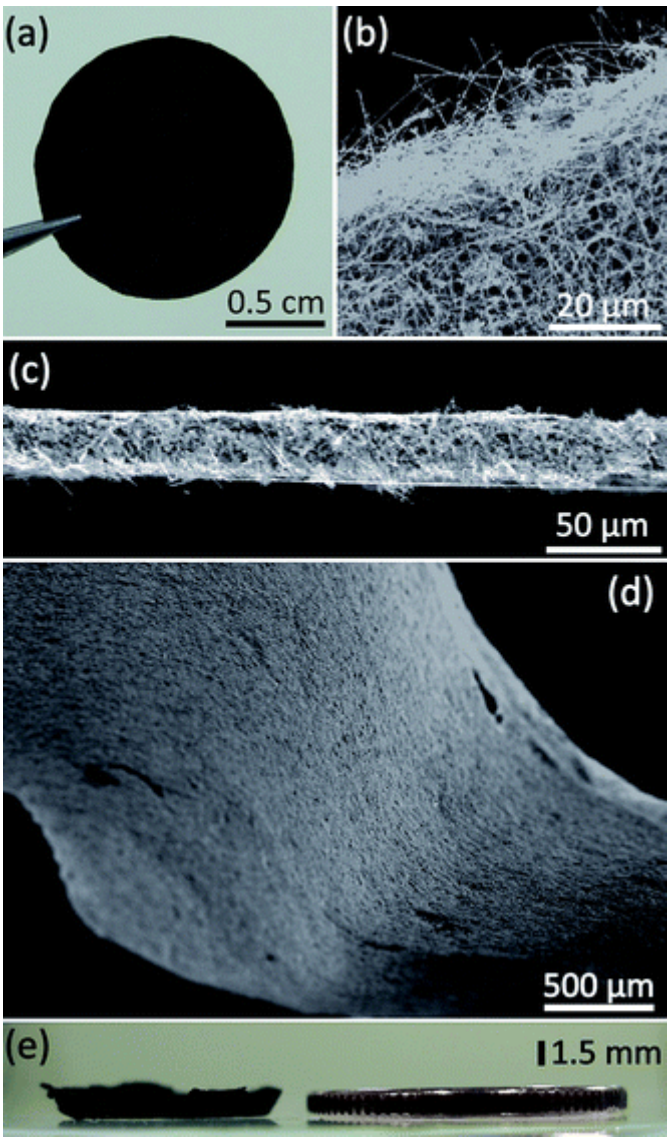


Figure 1.8 (a) Photograph of Ge nanowire fabric (diameter = 13 mm). SEM images of (b) the edge and (c) the cross-sectional area of a 30 µm thick fabric. (d) SEM image of the surface morphology of the Ge nanowire fabric. (e) Photograph of a 1.5 mm thick Ge nanowire fabric [59].

The ability to tune the reaction environments, *i.e.* pressure and temperature in a solution-based growth technique offers the possibility of scaling-up the product yield for commercial use, giving gram quantities of nanowires which can be molded into sheets, fabrics and inks. A SCF is a substance which has been elevated above its critical pressure and temperature. Many of the properties of SCFs vary with density and as such, conducting reactions in SCFs enables the manipulation of the reaction

environment through the control of temperature and pressure [103]. To this end, the supercritical-fluid-liquid-solid (SFLS) technique has been used to grow Ge nanowires. The SFLS process has also been combined with a templated method to guide the growth of Ge nanowires through anodic alumina membranes via Au catalysed growth [65]. These templates offer the capability of pre-aligning nanowires during the growth stage, thus eliminating the requirement for the post-alignment phase. $Ge_{1-x}Mn_x$ nanowires have also been synthesised using the SFLS technique, with the Mn atoms occupying substitutional sites in the Ge crystal lattice [104]. Incorporating Mn into Ge nanowires has been investigated as a means of studying dilute magnetic semiconductors (DMS) as possible building blocks for spintronic devices. Ferromagnetic materials such as Mn and Fe enable the combination of both semiconductor and ferromagnetic functionalities for these devices. The Mn-Ge binary system is of particular interest as many intermetallic compounds formed from these two elements are magnetic. Other examples include the doping of Ge nanowires with Mn by Grossi *et al.* via the co-evaporation of Ge and Mn powders [105] and the syntaxial growth of Ge/Mn-germanide nanowire heterostructures by Lensch-Falk *et al.* by CVD [106].

1.3.2 Alternative Catalysts for Metal Assisted Nanowire Growth

Au is considered the standard catalyst material for the growth of Ge nanowires because it is inert, easily deposited on a support and forms a low-temperature eutectic with Ge. Despite this, Au is problematic as it can be incorporated into the nanowire material during the alloying and growth stages. [107, 108] Au impurities can create deep level traps in Ge, even in low concentrations, decreasing carrier mobility and lifetimes.

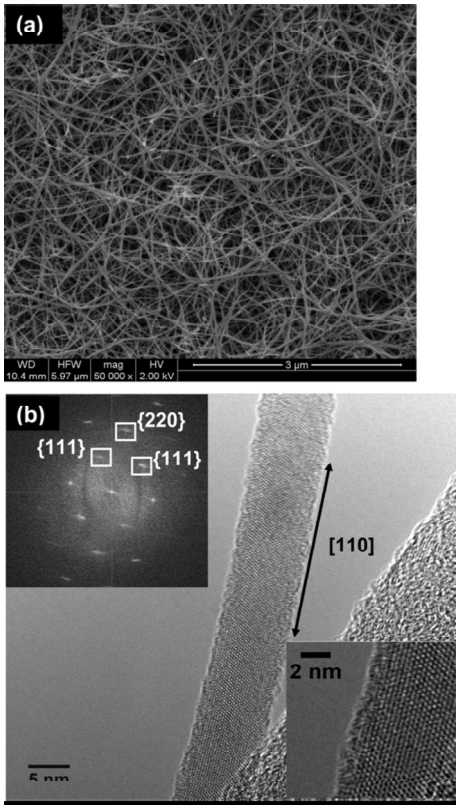


Figure 1.9 (a) SEM image illustrating the high density 1D Ge nanostructures grown from Ni nanoparticles. The HRTEM image shown in panel (b) represents a highly crystalline nanowire with a ⟨110⟩ growth direction (inset in panel (b) shows the high crystal quality of the nanowires synthesized) [79].

Consequently, the removal of Au seeds from the tips of VLS or VSS grown nanowires is a necessary prerequisite before device integration can occur. In addition to fuelling research into the removal of Au seeds from synthesised semiconductor nanowires [109, 110], these shortcomings of Au as a catalyst material for Ge nanowires have generated intense investigations into using other catalyst materials [111, 112]. Examples of recent work involving the growth of Ge nanowires from alternative metal seeds include the use of nickel [79] (figure 1.9), bismuth [113-115], indium [71, 116, 117], tin [118] manganese [106], copper [119], Ni-Cu bulk alloys [120], Au-Cu alloy particles [121] and silver [76, 122]. These catalysts can generally be categorised as: (1) high eutectic solid

state catalysts, which result in VSS-like growth, *e.g.* Ni, Cu and Ag, (2) catalysts with a low solubility in Ge which form liquid eutectics, *e.g.* In and Sn and (3) pure VSS catalysts, *e.g.* Au_xAg_{1-x} particles.

In fact, a wide range of alternatives have been identified by Lensch-Falk *et al.* who discuss the vapour-solid-solid (VSS) mechanism [123] as a possible substitute for the standard VLS methodology [112]. They highlight several important advantages of the VSS mechanism over the VLS approach, including reduced growth temperatures, more uniform diameter distributions, better control of nanowire orientation, increased purity and more abrupt interfaces for nanowire heterostructures. While Hoffman *et al.* have presented a detailed account of the nucleation of Si nanowires from solid seeds [124], similar studies on Ge nanowires have yet to be described. The VSS mechanism has also been used with SCF-assisted synthesis, in what has been termed the supercritical-fluid-solid-solid (SFSS) mechanism, as a means of growing Ge nanowires from Ni seeds [79, 125]. Both the VSS and VLS routes are effective methods for the growth of Ge nanowires and the ideal scenario would be to combine the advantages of both mechanisms to realize a much improved technique for fabricating Ge nanowires. Despite the fact that the VLS mechanism remains the most common route to nanowire synthesis, it is likely that the VSS mechanism will also become a widely accepted method, especially for the growth of heterostructures [126], due to the much lower solubility of the semiconductor material in Au. This will drastically reduce the "reservoir effect", thus yielding much sharper interfaces when the source material is changed. Additionally, the much lower temperatures employed for the VSS mechanism are advantageous for processing.

1.3.3 Seedless and Self-seeded Nanowire Growth

Germanium nanowires have also been synthesised without the use of catalytic seeds. Metal particles introduce contaminants into a nanowire system [107] which renders their integration into electronic applications problematic. Lotty *et al.* used a self-seeded growth method in supercritical toluene to synthesise Ge nanowires, using diphenylgermane as a Ge precursor[78], and proposed a model which accounts for nanoparticle coalescence at the beginning stages of nanowire growth and Ostwald ripening at the later stages. They also used in-situ TEM to show that nanowire diameter increased with temperature as a result of diffusion of Ge particles from the shell to the nanowire core (figure 1.10). A mechanism for nanowire growth was also proposed. This study extended the work carried out by Hobbs *et al.* [77] on the seedless growth of Ge nanowires from a variety of complex metal/organic precursors and consequently, represents a rather unique method for Ge nanowire fabrication when compared to the more widely reported metal-seeded growth methods. The authors showed that it may be possible in the future to control the diameters of Ge nanowires through the tailoring of precursor molecules. Other seedless methods have also been used to grow Ge nanowires, including a self-induced solid seeding method that makes use of copper foils [127]. Instead of metal nanoparticles acting as growth promoters, the in-situ formation of Cu_3Ge catalyses the growth of Ge nanowires.

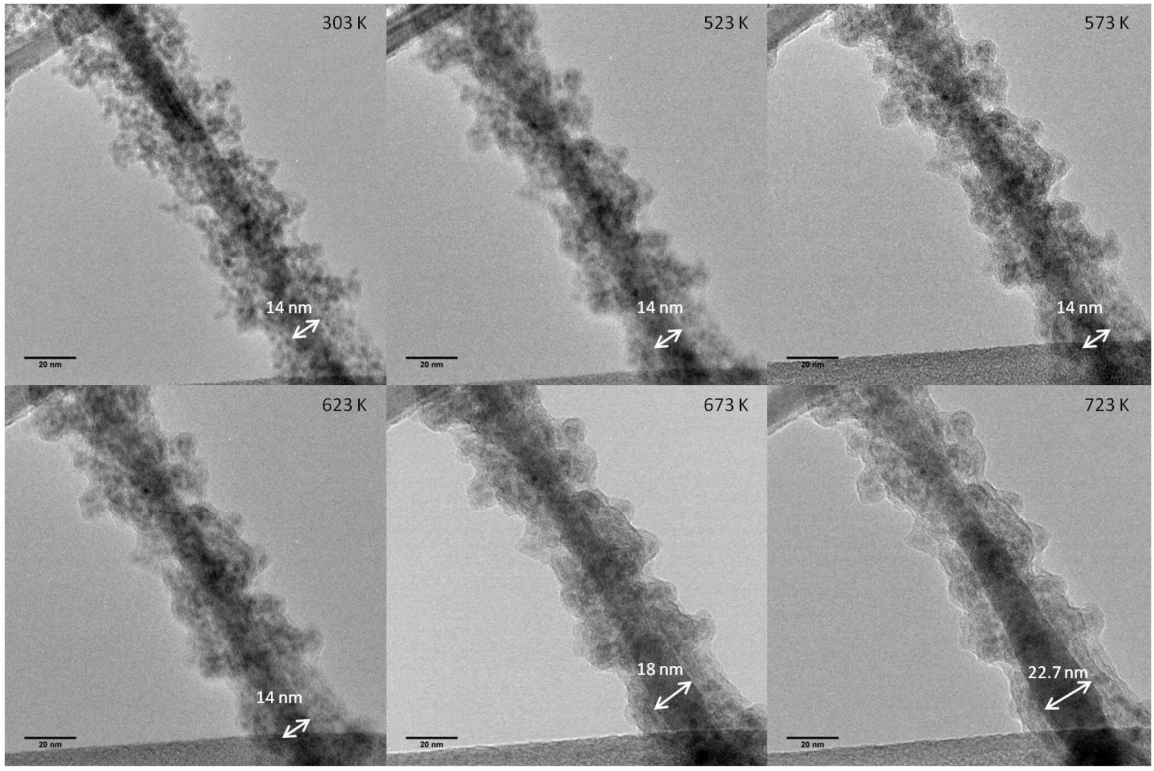


Figure 1.10 Ge nanowire grown using a self-seeded growth mechanism. In situ TEM heating stage experiments showing the Ge nanowire diameter increasing with temperature [78].

Kang *et al.* also reported the use of Cu_3Ge nanocrystals for growing Ge nanowires which eliminated the use for elemental metal seeds. Specifically, the Ge from the source material decomposed into the Cu of the Ni-Cu films which formed Cu_3Ge nanoscrystals. Ge then precipitated out of these nanocystals, forming GeNWs. However, the Ni-Cu bulk alloys from which the wires were synthesised produced two types of nanowires that were of non-uniform diameter and crystallinity. The first type were long, thin and typically monocrystalline, while the second category were thick and had extended defects throughout their structure. Unfortunately, both nanowire types were found in abundance from the same reaction, which could be problematic. Cu, a current collector in lithium ion batteries, is an attractive material for growing nanowires. Other copper-germanide derivatives have also been recently

used to form Ge nanowires [74]. Ge nanowires have also been grown using a seedless, low pressure CVD method on various substrates, including stainless steel and tungsten [128]. The Ge nanowires produced were subsequently used as templates for the growth of silicon oxycarbide (Si/O/C) nanotubes. The cultivation of Ge nanowires on various substrates has also been employed as a means of studying how surface pre-treatments effect growth and have included stainless steel, Fe, Mo, Ta, W, Si and SiO_2 [129]. A Ge buffer layer was used successfully to promote nanowire growth on the Si and SiO_2 substrates, a concept which has been reported elsewhere [56, 93]. A study of Ge nanowires as templates for the growth of other materials was also carried out by Tao *et al.*, in which they were employed as templates for the growth of ZnO nanowires [130], a promising material for photonics due to its wide bandgap of 3.37 eV. Hu *et al.* also used Ge nanowires as seeds to grow monocrystalline Ge layers on Si [131]. The exploitation of Ge nanowires for the subsequent growth of other materials will likely become a prevalent technique in the future, owing to the facile methods that are employed to grow them, in addition to the immense understanding of Ge which has been obtained over the last two decades. Additionally, seedless growth methods are likely to be utilised for the process of growing materials from Ge nanowires, as contamination in the Ge nanowire templates is minimised. Non-metal catalysed template methods have also been used to grow Ge nanowires from ionic liquids, as reported by Al-Salman *et al.* [132]. However, the nanowires produced were amorphous with a larger degree of surface roughness and as such, the validity of this technique is questionable.

Dailey *et al.* investigated a "seedless" growth method to synthesise Ge nanowires with a bimodal diameter distribution [133]. Here, wires grown from a Au/Si (111) layer

displayed narrower diameters than those grown from deposited seeds. Referring to the method as "seedless" is misleading however, as both types of nanowires grow via a modified VLS process, which suggests the presence of a seed particle. Finally, Ge nanowires have been synthesised using a non-catalytic CVD approach in which temperature was varied to give systematic diameter control [134].

1.3.4 Nanowire Synthesis Outlook

The primary challenge facing the bottom-up synthesis of nanowires is a requirement for their post alignment prior to assimilation into devices, as the majority nanowires are generated as entangled meshes [40, 77, 79]. Whilst several of the approaches outlined above combine growth and alignment into a single process [55, 61, 62], thus removing the requirement for post-alignment, these techniques are in the minority. The endotaxial method outlined by Li *et al.* represents a significant step forward in the alignment of Ge nanowires during the growth phase [55]. Pre-alignment of a Ge nanowire along (in-plane) and within a substrate is ideal for conventional IC design which relies on the active channel of the device lying co-planar to the Si wafer substrate. This requires a very high degree of controllability over nanowire placement and the endotaxial method may be what is required to achieve this. Additionally, methods that make use of randomly oriented nanowires films (without alignment) may be used to create transparent flexible electrodes. This has already been demonstrated for Ag nanowires [135] and is more than likely applicable to Ge nanowires also.

1.4 Kinetics and Thermodynamics of Ge Nanowire Growth

1.4.1 The Au/Ge System

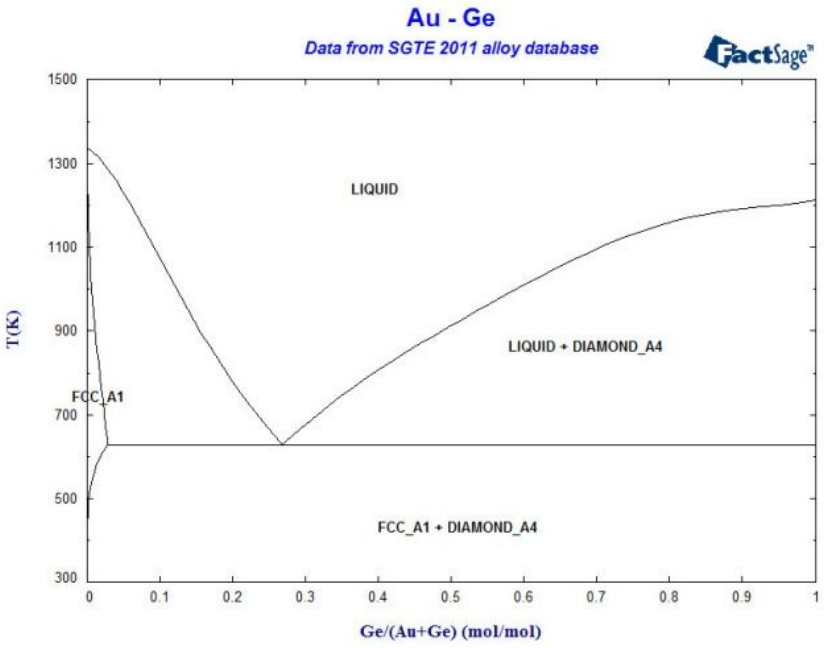


Figure 1.11 Au-Ge binary phase diagram. The diagram is dominated by a single eutectic point at 360 ^{o}C with 28 % Ge in Au.

Successful implementation of Ge-based technology will require an in-depth understanding of the solid-state and molten interactions in metal-germanium systems. The Au/Ge system in particular is important for the growth of Ge nanowires, as Au forms a deep low-temperature eutectic with Ge and has been employed successfully in semiconductor nanowire growth for many years. The behaviour of this system is predicted by the Au/Ge bulk phase diagram, as shown above in figure 1.11, which can be used to trace the progression of an Au/Ge binary alloy from a solid Au film to Ge nanowire growth, as the concentration of the Ge component in the two-phase system increases. However, care has to be taken as

deviations from the bulk phase diagrams occur in nanoscale systems, such as the Au/Ge alloy particles used to seed nanowire growth [136-139]. Specifically, the eutectic temperature and eutectic composition are reduced in nanoscale systems due to capillary effects, which are often represented by the Gibbs-Thomson equation [140]. Sutter *et al.* have investigated the nanoscale phase diagram of the Au/Ge system and used it to predict the temperature-dependent equilibrium composition of the alloy drops at the tips of Ge nanowires [138, 139]. Surprisingly, the work carried out by Kim *et al.* on the Au-Si system yielded results that were contrary to those obtained by Sutter *et al* [141]. Kim *et al.* found that the Au-Si phase diagram had no observable size dependence as there was no change in supersaturation with particle volume. The melting behaviour of a Au/Ge bi-layer was also investigated by Kryshtal *et al.* who observed that liquid-phase formation at the eutectic temperature only occured if the Au film thickness was above a critical value [142].

The difference between the bulk and nanoscale phase diagrams of the Au/Ge alloy system were also investigated by Chueh *et al.* The difference was highlighted by varying the Au concentration in the wires and then utilising an annealing/cooling step to induce phase separation of the Au and the Ge [143]. Ge will phase separate from Au upon cooling due to the differences in their surface energies [144] and depending on the amount of Au present, a variety of structures ranging from pyramid shaped nanoislands to uniform core-shell structures can be formed, as shown in figure 1.12. This formation of various nanostructures (which included islands, periodic nanodisks and core-shell structures) was explained by the phase diagram [139], with the authors controlling the atomic percentage of Au and thermal annealing above the eutectic temperature.

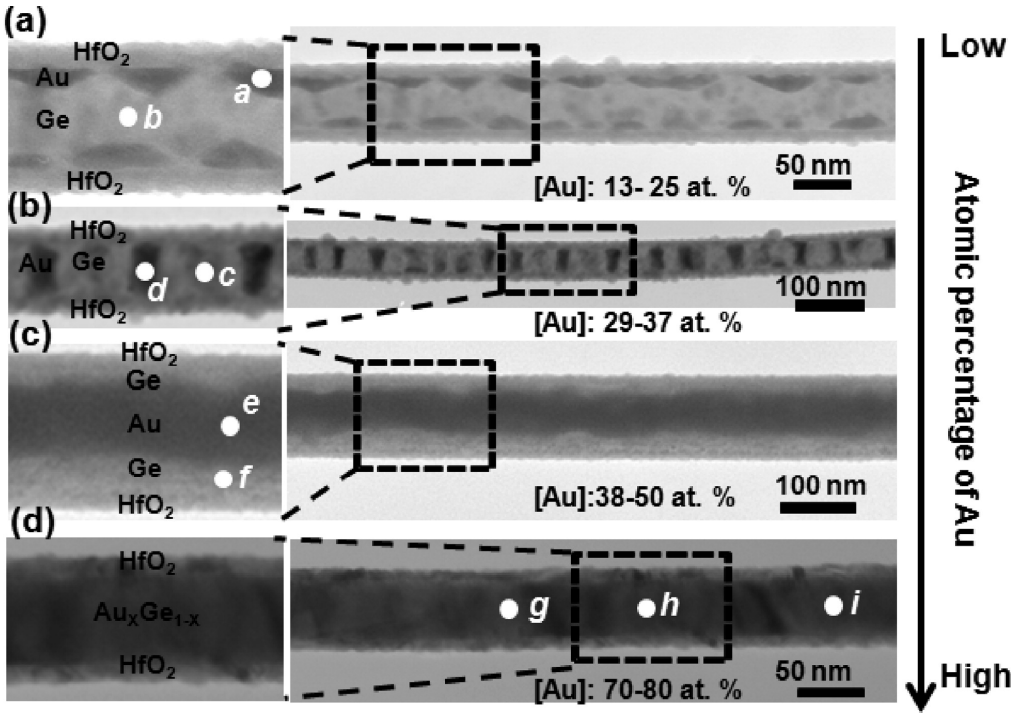


Figure 1.12 TEM images of the enabled Au/Ge nanostructures after thermal annealing at 450 °C for nanowires with: (a) 13−25, (b) 29−37, (c) 38−5, and (d) 70−80 atom % Au [143].

The Au/Ge system has been investigated for other applications such as alternatives to Pb containing solders [145-147] and as such, its structure has the been the focus of much examination [148-151]. Findings have contradicted the common understanding that Au/Ge does not form germanide compounds. For example, Tasci *et al.* identified the formation of a Au_5Ge_2 compound in which the Ge was coordinated by 6 Au atoms [149] while Takeda *et al.* inferred that the Ge atoms locate at the substitutional positions of the Au atoms via reverse monte carlo simulations [150]. Comparatively, neutron diffraction has also been used to study the structure of a $Au_{0.72}Ge_{0.28}$ eutectic system [152], while the electronic band structure of Au/Ge was investigated using angle-resolved photoemission and density functional theory calculations [153]. Additionally, Au nanocatalysts on the tips of Ge nanowires mostly adopt a face-centered-cubic structure, but a minority (about 10 %) crystallise in a hexagonal close-packed structure upon solidification [154].

Studies into the Au-Ge system as part of a ternary alloy have also been conducted. One possible advantage of using a ternary alloy system instead of a binary system is that it may allow the incorporation of dopants into the interior of a Ge nanowire through the alloy droplet [68] and potentially avoids the difficulties linked with the surface deposition of dopants. Ternary systems which have been investigated and modelled include the Au-Ge-Ni [155], Au-Ag-Ge [156], Au-Ge-Sb [157] and Au-Ge-Sn [158] systems.

1.4.2 Thermodynamic Considerations

A prerequisite for the integration of nanowires into devices is to be able to understand the kinetic and thermodynamic principles which dictate their controlled synthesis [159-162]. Thermodynamic aspects of Si nanowire growth have been reported elsewhere [141, 163-169], due to the importance of Si in current CMOS based devices. In this section, the thermodynamic and kinetic aspects of Ge nanowire growth will be detailed.

One method often utilised to study the dynamics of nanowire growth is in-situ transmission electron microscopy (TEM). In particular, video-rate lattice-resolved environmental TEM [170, 171] allows the introduction of a gaseous precursor into the microscopy cell, enabling the observation of nanowire growth in real time. As in-situ TEM allows the examination of nanoscale systems as they undergo physical transformation, *e.g.* upon heating, for example, insights into the liquid-solid interface behaviour between a metal tip and a semiconductor nanowire, phase nucleation and the mechanisms controlling nucleation and nanowire growth can be obtained [172-174].

For example, Holmberg *et al.* used in-situ TEM to carry out temperature-dependent studies on Ge nanowires encapsulated within amorphous carbon shells [140], as shown in figure 1.13. They found that as the temperature increased, the liquid-solid interface expanded into the wire while Ge re-crystallised in the spherical tip. This expansion was attributed to a capillary effect, as shown in equation 1, directly resulting from the presence of the carbon shell:

$$p_c = \Delta P^{sphere} - \Delta P^{cylinder} = \gamma\left[\left(\frac{2}{r^{sphere}}\right) - \left(\frac{1}{r^{cylinder}}\right)\right] \quad (1)$$

where p_c is the capillary pressure due to the difference in Laplace pressures ΔP in the spherical cap and the cylindrical neck of the nanowire, γ is the surface energy (units of energy per area) of the melt and r is the radius. The carbon shell also prevented any structural loss as the Ge nanowires were heated. Au and HfO_2 shells have been used more recently to prevent loss of structure to Ge nanowires upon heating [143], and may provide a means of more accurately studying in-situ behaviour in the future. The capillarity effect of nanoscale droplets is generally explained by using the Gibbs-Thompson formula [175], which explains how the very high surface to volume ratio of spherical seeds can account for nanoscale size effects, equation 2:

$$\Delta G_{G-T} = \frac{\alpha\gamma V_m}{r} \quad (2)$$

where ΔG_{G-T} is the change in Gibbs energy, r is the diameter of the seed, V_m is the volume of the seed, γ is the surface energy and α is the specific free energy. In chapter 4, the Gibbs-Thomson relationship will be expanded upon further in terms of the solute and equilibrium concentration of Ge in the nanowire seed. Sa *et al.* used

the capillarity effect to infer the size dependence composition of of VLS grown $Si_{1-x}Ge_x$ nanowires. They also suggested that the shift of droplet composition into the Au and Si rich regions of the Au-Ge-Si ternary alloy phase diagram was a result of these same capillary effects [176]. Capillarity and surface tension have also been used to account for the differences in droplet phase behaviour in VLS grown Ge nanowires [177], as the solid-vapour interfacial energy plays an important part in establishing the nanowire phase diagram.

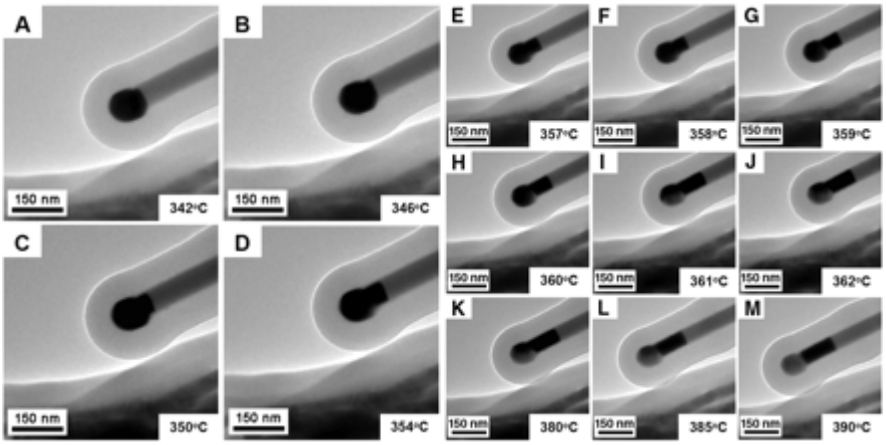


Figure 1.13 TEM images of a Au seed particle melted at 346 °C which migrates into the stem of the nanowire with increasing temperature. Ge recrystallised in the spherical end as the Au/Ge melt shifts into the neck of the nanowire [140].

Gamalski *et al*. used in-situ TEM to study the metastability of Au/Ge catalysts below the eutectic temperature and found that both solid and liquid metastable phases are possible [170, 171]. The phase of the catalyst is significance in determining how rapidly the chemical potential of the system can be increased to overcome the kinetic barrier for nucleation; thus determining the rate of interfacial ledge formation [124]. Gamalski *et al.* [171] suggested that the liquid metastable phase may be a result of high nucleation barrier to forming diamond-cubic Ge, while the Au/Ge liquid phase is thermodynamically and kinetically accessible according to equation 3[171]:

$$E_B \propto \frac{(\beta)^3}{(\Delta\mu)^2} \quad (3)$$

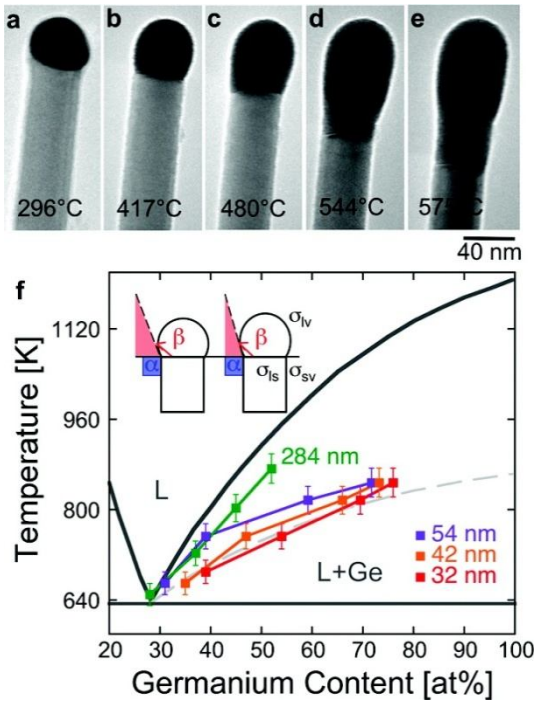


Figure 1.14 (a) to (e) Sequence of TEM images of a Ge nanowire close to the nanowire tip during *in-situ* annealing experiments at different temperatures; between room temperature and 575 °C. (a) Au−Ge alloy crystalline nanoparticle adjacent to the Ge nanowire before surface melting starts, (b) to (e) exchange of material across the Ge nanowire/liquid drop interface after melting of the alloy Au−Ge nanoparticle and (f) Au−Ge binary alloy phase diagram [138].

where $\Delta\mu$ is the chemical potential of Ge in the liquid, compared to the NW and β is a geometrically weighted difference of interfacial energies. Increasing the supersaturation (which is described in great detail in chapters 3 and 4) lowers this barrier to nucleation, thus increasing the rate at which Ge crystallizes at the liquid-solid interface giving a higher nanowire growth rate. This manipulation of nanowire growth rate is the focus of chapters 3 and 4. Gamalski *et al.* speculated that the solid metastable phases were a result of compositional changes during Ge nanowire

growth and that the VSS mechanism was a result of high Ge solubility in these phases [170]. Moreover, solid phase metastable Au/Ge seeds were observed in a separate report by Sutter *et al.*[137] (figure 1.14).and the concept of metastability has also been investigated for $Ge_{1-x}C_x$ alloy nanowires by Kim *et al.* [178].

One of the most significant contributions to the study of droplet/nanowire interface behaviour in Ge nanowires [86] was the establishment of a nanoscale phase diagram and its comparison to the bulk counterpart by Sutter *et al.* [137-139]. Estimation of equilibrium concentration along the Ge-liquidus was achieved using in-situ TEM and described how the droplet adjusted its composition upon heating or cooling to achieve an equilibrium Ge concentration according to the adjusted nanoscale phase diagram. Exchanging Ge atoms with the nanowire causes an expansion or contraction of the droplet size depending on whether it is heated or cooled. This exchange also causes a change in the faceting of the droplet/nanowire interface during the particle expansion/contraction. The Ge composition, which was used to establish the nanoscale phase diagram was determined using equation 4:

$$N_{Ge} = \frac{V(T) - N_{Au}v_{Au}}{v_{Ge}} \quad (4)$$

where N_{Au} is the (constant) number of Au atoms in the drop and v_{Au} and v_{Ge} denote the atomic volumes of the alloy components, determined from the densities of liquid Au and Ge. Equation (4) is used in chapter 4 to calculate the number of Ge atoms in the nanowire seeds and subsequently is used to determine the equilibrium Ge concentration. A size-dependent depression was observed for the nanoscale phase diagram when compared to the bulk, resulting in a very high equilibrium Ge content

at comparatively low temperatures. Dayeh *et al*. investigated the thermodynamics of Au diffusion along Ge nanowires using a Si layer to block this diffusion from the droplet of a Ge nanowire into the nanowire itself [179]. They estimated the lowest surface energy for a Au/Ge monolayer at the nanowire tip using a method outlined previously[180], and expressed in equation 5:

$$\Delta\mu = \mu_{Au-y}^{Surf} - \mu_{Au-y}^{Tip} = \frac{2\Omega_{Au}}{d}\left(\sigma_{Au-y(l)on\ y(s)}^{s} - 2\sigma_{Au-y(eutectic)}^{l}\right) + 4(\Delta H)x_y^2 x_{Au} \quad (5)$$

where Ω_{Au} is the atomic volume of Au, d is the nanowire diameter, $\sigma_{Au-y(l)on\ y(s)}^{s}$ is the surface energy density of a monolayer of liquid Au-y alloy on the solid y NW surface, $2\sigma_{Au-y(eutectic)}^{l}$ is the surface energy density of a monolayer of Au-y in the molten growth seed, ΔH is the enthalpy of mixing of Au and y, and x_y is the compositional fraction of y in Au.

Thermodynamic concepts have also been used to account for the seedless growth of Ge nanowires, using MBE on Si (001) substrates. A thermodynamic equation was proposed which explained that the driving force for Ge nanowire formation is the reduction of surface energy, rather than strain relaxation[181]:

$$E = V[\Delta\rho_{eff} + \frac{4}{btan\theta}\Delta\gamma + \frac{4\Gamma}{b^2 tan\theta}] \quad (6)$$

where V is the nanowire volume, Γ is the total energy associated with edges connecting adjacent facets and $\Delta\rho_{eff}$ is the sum of the elastic energy lowering. A

strong thermodynamic driving force was found to stabilise long faceted nanowires, according to the above equation.

1.4.3 Kinetic Considerations

The kinetics of Si nanowhisker (nanowhisker was the original term for nanowire) growth was first investigated by Givargizov in 1975 [175] and involved an investigation of the supersaturation as a function of the seed particle diameter as governed by the Gibbs Thompson effect (equation 7). Other kinetic parameters, such as the relationship between the nanowhisker growth rate and the supersaturation (equation 8) and the critical diameter, *i.e.* the lower limit of the thermodynamically attainable nanowire diameter in a nucleation mediated growth (equation 9). These expressions are given below:

$$\Delta\mu = \Delta\mu_0 - \frac{4\Omega\alpha}{d} \tag{7}$$

$$X \sim (\Delta\mu / kT)^n \tag{8}$$

$$\frac{\Delta\mu_0}{kT} = \frac{4\Omega\alpha}{kT}\frac{1}{d_c} \tag{9}$$

where $\Delta\mu$ is the chemical potential differences of Ge in the vapour phase compared to the nanowire, d_c is the critical diameter, k is the Boltzmann constant, T is the temperature, $\Delta\mu_0$ is the difference between the chemical potentials of Ge at a planar boundary, Ω is the atomic volume of the semiconductor species and α is the specific free energy of the whisker surface. These equations have formed the basis of many kinetic studies on semiconductor nanowires and have been expanded upon by Dayeh

et al. who investigated the kinetics associated with the nanoscale Au/Ge system in relation to the growth of Ge nanowires [182]. They found that the nanowire growth rate decreased for smaller diameters as described by the Gibbs-Thomson effect and presented an equation relating the supersaturation to the Ge concentration in the Au/Ge alloy droplet, equation 10:

$$\frac{\Delta\mu}{kT} = \frac{\Delta\mu_0}{kT} - \frac{1}{\kappa}\ln\left(\frac{C_{NW}}{C_\infty}\right) \quad (10)$$

where C_{NW} is the Ge concentration in the Au/Ge alloy nano-droplet and C_∞ is the equilibrium Ge concentration for bulk Au-Ge alloy. The term κ is added to equation S1 to take into account surface energy density changes, and consequently curvature changes with temperature. Increased equilibrium Ge concentration for smaller Au-Ge binary systems reduces the supersaturation, which in turn, yields a reduced growth rate. A decrease in nanowire diameter to a certain cutoff limit leads to a progressive reduction in the supersaturation and the termination of nanowire growth. As evident from equations (7), (8) and (9) increasing the supersaturation will increase the growth rate and decrease the critical. By increasing the GeH_4 partial pressure to a certain limit, Dayeh *et al.* [182] successfully manipulated the Au-Ge supersaturation concentration, leading towards a decreased critical diameter. Ge nanowire growth kinetics were also investigated within the Gibbs-Thomson framework by Renard *et al.* who also found that narrower wires had shorter lengths and established a critical diameter below which there was no growth [183].

In addition to Gamalski *et al.* work on the metastability of Au/Ge catalyst particles [170, 171], this group have also investigated nanowire nucleation kinetics at the triple

phase boundary (TPB), in a Au/Ge binary system for VLS-based nanowire growth [83], (see figure 1.15). A cyclic supersaturation model, whereby a new Ge bi-layer forms at the TPB upon overcoming an activation energy barrier for nucleation, was inferred as determined by:

$$\Delta G_B = \alpha^2/(4\Delta\mu) \quad (11)$$

The size of this barrier determines the rate of nucleation and thus the overall nanowire growth rate. In a cyclic process, the wetting angle of the catalyst increases as Ge precipitates at the rough TPB region, thus continuously increasing supersaturation during the cycle. Continued rising of the supersaturation results in a fall of the kinetic energy barrier for Ge bi-layer formation and step nucleation at the TPB. Step flow lowers the supersaturation and causes the dissolution of the Ge in the TPB region completing a growth cycle. Nanowire nucleation and growth has also been shown to depend on parameters such as substrate temperature, Ge deposition rate and surface diffusion length [184].

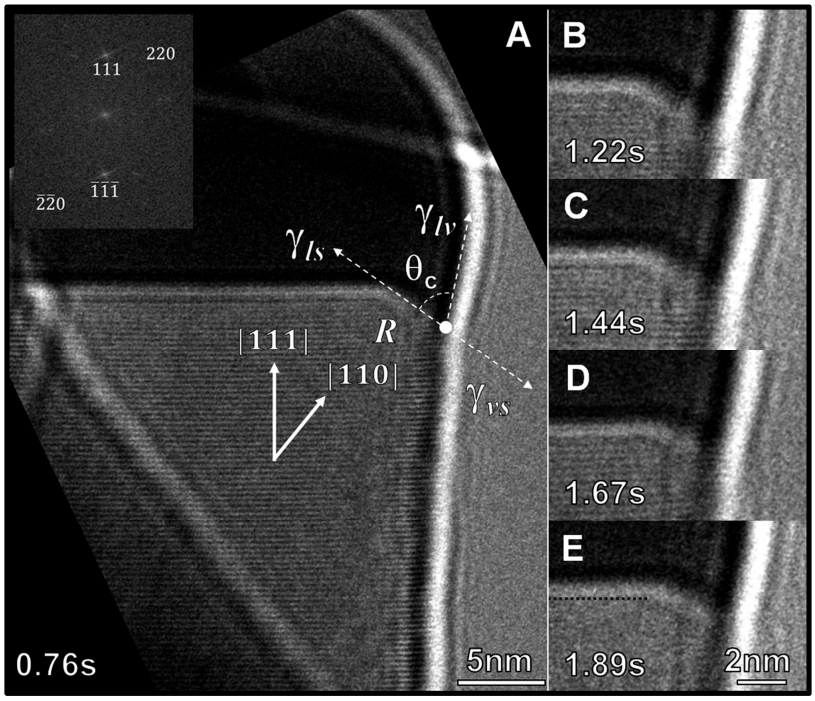


Figure 1.15 High-resolution phase-contrast TEM image sequence of the catalyst interface around the TPB of a growing Ge nanowire at ≈ 310 °C in Ge_2H_6. In (A) the atomically rough surface is denoted by *R*, the wetting angle by θ_c, and γ_{lv}, γ_{ls}, and γ_{vs} are the surface energy differences between the liquid−vapour, liquid−solid, and vapour−solid surfaces, respectively. The inset shows a selected area fast fourier transform of the Ge nanowire. In (E) the original (111) solid−liquid interface is traced with a dotted black line to highlight the advancement of the growth interface [83].

Kim *et al.* have studied the low-temperature catalytic growth of Ge nanowires and identified three pathways by which growth can proceed, depending on the temperature employed [185]. They rationalised that the pathways arise due to kinetic competition between the imposed timescale for Ge addition (τ_{Au}) and the inherent time scale for Ge nucleation in the Au and Au/Ge system (τ_{Ge}), where the latter timescale is described by equation 12:

$$\tau_{Ge} \approx \tau_0 \exp\left(\frac{\gamma^3}{(\Delta\mu)^2 kT}\right) \quad (12)$$

where γ is a geometrically weighted difference of interfacial energies and $\Delta\mu$ is the Ge supersaturation. The three pathways were identified as VSS, VLS and a combination of both mechanisms. When $\tau_{Au} \ll \tau_{Ge}$, this corresponded to standard VLS-type growth as the Au was completely dissolved before Ge nucleation (as the seed was a liquid alloy). However, with decreasing temperature, τ_{Ge} decreased rapidly and $\tau_{Ge} < \tau_{Au}$ meaning that solid Au was still present when Ge nucleated (the seed was not a liquid alloy), corresponding to a mixed regime of both VSS and VLS growth. Finally, when $\tau_{Ge} \ll \tau_{Au}$, Ge nucleated out of a seed particle that was mostly solid Au (with a thin AuGe liquid film on the surface), following a VSS growth pathway.

The differences in the growth kinetic between Ge and Si nanowires have been studied by Artoni *et al.* [165], who observed that the two material systems grow in different temperature and time regimes, even though Si and Ge share similar properties, crystal structures and phase diagrams. Ge nanowire growth was limited by the eutectic temperature only (a thermodynamic constraint), while Si nanowire growth was limited kinetically due to the low activation energy of surface diffusion of Si atoms. Additionally, the incubation times were much higher for Si nanowire growth. Also a considerable difference (approximately 60 %) in critical diameter was observed between Ge and Si nanowire growth due to the difference in surface energies, atomic volumes, and supersaturation. [186]

While the VLS mechanism has been studied in detail for Ge nanowire growth, the VSS mechanism remains relatively unexplored for most material systems, including Ge. A limited number of reports have been presented, highlighting diffusion limited

models for VSS nanowire growth [187, 188]. Despite the fact that these were based on III-V systems, the diffusion-limited approach (as opposed to supersaturation-limited) illustrated in these investigations should be applicable to Ge provided that certain assumptions are valid [187]. These assumptions include a hemispherical particle, a large interwire separation, negligible diffusion within the seed and steady-state adatom diffusion on the substrate and nanowire sides. While there have not been any reports detailing the VSS mechanism in Ge nanowires to date, it is likely that the VSS growth model will become more understood in the future, due to the increasing popularity of sub-eutectic nanowire growth techniques.

1.5 Morphology Control in Ge Nanowires

Investigations into understanding and controlling nanowire morphology, *e.g.* length, diameter, orientation, has largely been achieved using in-situ TEM approaches, due to ability to observe real-time morphological changes in the structure of nanowires [174, 185, 189]. As discussed above, morphological changes can be induced in Ge nanowire surfaces through annealing and adjusting the Au composition. This composition was varied by tuning the thickness of a Au film that was sputtered onto the surface of the nanowires, which determined the overall Au:Ge atomic ratio of the nanowires[143]. Changes in the morphology of Ge nanowires can also be achieved by varying the catalyst material used as the growth seed [64]. Schwarz *et al.* proposed a simple model to explain morphological changes in nanowires grown via the VLS mechanism and postulated that three elementary processes are responsible for a variety of growth behaviours [160]: facet dynamics, droplet statics and the introduction of new facets were responsible for changes in VLS grown nanowire morphologies and resulted in straight wires, kinked nanowires and nanowires which crawl along

the surface. Their model placed particular importance on the capillary force exerted by the liquid at the TPB; a concept which has been discussed more recently in terms of nanowire morphology by Gamalski *et al* [83].

Generally, nanowire morphology can be discussed in terms of kinks, defects, twins and overall crystallinity. Controllable crystallinity of Ge nanosctructures was achieved by Petkov *et al.* through the use of channelled alumina surfaces [65]. The same group also studied the defect formation in Ge more recently through the use of Ag and Au_xAg_{1-x} alloy seeds [76, 122] and observed that defects could be transferred into Ge nanowires from the seed particles via a supercritical-fluid-solid-solid (SFSS) process using both Ag and Au_xAg_{1-x} alloy seeds. The choice of seed was based on meeting several criteria including: low twin formation energy, the presence of a solid-phase seeding regime and similar structure and lattice constants between the particle and the nanowire. The transfer of crystallographic information from a seed particle to a nanowire opens up the possibility of engineering the structure of Ge nanowires and enabling the tuning of band structure via strain modulation. Kinking and defects in Ge nanowires were also investigated by Geaney *et al.* who used a high boiling point (HBS) method to vary the synthesis temperature to produce straight nanowires consisting of stacking faults (longitudinal and transverse), kinked nanowires and tortuous nanowires [190]. While kinked nanowires may have limited applications outside of three-dimensional electronics [191], the study of such architectures provides an understanding of how kinks are formed, thus enabling future generations of researchers to more accurately synthesise straight wires of uniform structural integrity.

1.5.1 Diameter and Length Control

The control of nanowire diameters and lengths is considered to be of paramount importance due to the dimensional dependency of nanoscale properties. Kim *et al.* have investigated the control of nanowire diameters via a two-temperature process [56]. They suggested that the use of low growth temperatures can prevent tapering of Ge nanowires, as diffusing adatoms are less likely to be assimilated into the nanowire sidewalls, ensurintg uniform nanowire diameters which can be seeded by Au particles of varying sizes. Seedless growth methods have been effectively used to grow Ge nanowires with tunable diameters in the past few years, by varying the partial pressures and temperatures employed [134]. Ge nanowire diameters have been controlled to produce ultra-thin nanowires in the absence of conventional metal seeds, with one report quoting diameters below 10 nm [77, 78]. Both reports used complex organometallic Ge precursors to grow the nanowires, which consist of an amorphous shell around the Ge core, that helps passivate the nanowire surfaces and maintains a uniform diameter. The same group also used solid phase seeding (via a SFSS approach) of Ge nanowires using size-selective Ni seeds which enabled wires to be synthesised with mean diameters of 9.3 and 14.2 nm respectively [79]. Controlling the size of the original metal seed was vital to achieving governable nanowire diameters. Solid phase catalytic seeds with high melting points, Ni, Cu, Fe *etc.*, offer controlled inter-particle diffusion and precise control over radial dimension of nanowires [79, 119]. However, during nanowire growth these seeds for germanides which increasing the volume of the seeds by up to 300 %, with an increase in the lower limit of attainable nanowire diameter. Biswas *et. al.* have looked into this seed expansion problem and have used Ag_xAu_{1-x} growth promoters, which does not go through any germination, to synthesise diameter controlled

nanowires in the sub-10 nm regime [76]. Diameter controlled seed particles were also utilised by Wen *et al.* to regulate the diameter of Ge nanowires grown from Au nanoparticles [75]. The diameters of the nanowires (40 and 80 nm) were found to exactly match the diameter of the nanoparticles.

The use of amorphous sheaths, as mentioned previously [140, 143], have been used successfully to control the diameters of Ge nanowires. The technique is analogous to controlling nanowire diameter via template pores such as anodic aluminium oxide (AAO) [192], as the sheath can be likened to a pore from which the nanowire grows. Materials used for sheaths include carbon [193], oxides [92] and multi-walled carbon nanotubes [90]. The use of a carbon sheath appears to be particularly effective because one-dimensional carbon materials can be grown using the VLS process with the same metal catalysts used for Ge [194, 195]. The carbon sheath is also immiscible with Ge and is formed simultaneously with the wire during VLS growth. The sheath was found to completely block vapour deposition on the nanowire sidewalls, preventing tapering and thus giving highly uniform diameters, as shown in figure 1.16 [193].

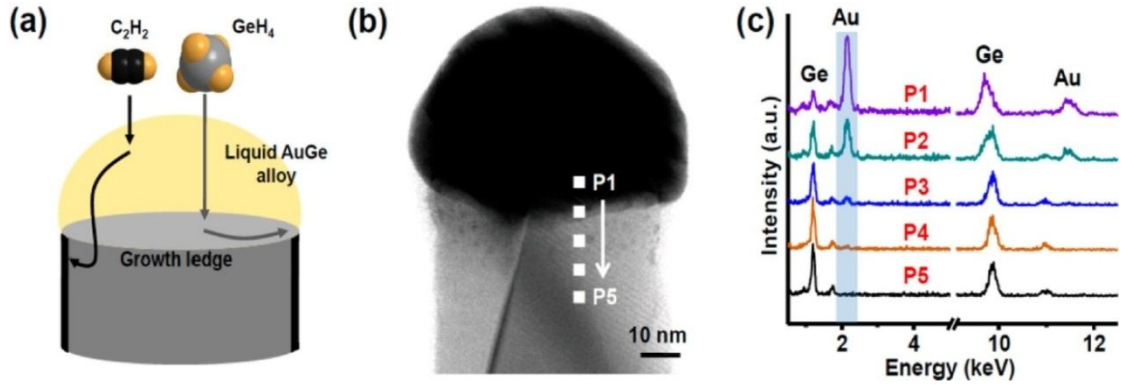


Figure 1.16 (a) Schematic for carbon sheath formation during the Ge nanowire growth process, (b) bright-field STEM image of a single Ge nanowire with a carbon sheath and (c) EDS analysis of the corresponding nanowire from the positions P1 to P5. This data shows that Au diffusion does not occur below the carbon sheath [193].

Length is also a factor which can be affected by the temperature of the growth process, as was shown by Pecora *et al.* when they investigated the epitaxial growth of Ge nanowires of various orientations [66]. They reported that the length of the wires increased as the temperature increased from 380 to 520 ^{o}C and that the lengths varied at a specific temperature depending on the growth orientation. Nanowire lengths can usually be altered by varying the growth time of the reaction and generally there is a linear dependence present [196]. In other words, the time frame over which the precursor is injected into the system in a typical CVD set-up determines the length of the resulting nanowires and is logical because when the injection stops, there is no longer any incorporation of the semiconductor material into the nanowire and therefore growth discontinues. Other methods of tuning the length of nanowires may involve manipulating the kinetics at the liquid-solid interface via the supersaturation of the metal seed particle [76, 197]. Dubrovskii *et al.* have demonstrated the narrowing of the length distribution of Ge nanowires and also presented a theoretical model to explain the behaviour [196]. An interesting conclusion from this report was that as the growth time was decreased from 70 to 15 minutes, the diameter dependence of the length changed. At higher growth times, the length increased with diameter which can be explained by the Gibbs Thomson effect. However, at lower growth times, nanowire lengths decreased with increasing diameter, which suggested the presence of a diffusion-induced growth regime.

1.5.2 Growth Orientation

The control of nanowire growth orientation is highly desirable, as the electronic and optical properties of the nanowire are often orientation dependent, and has been a topic of much investigation in recent years [198]. The orientation of nanowires has

been shown to be diameter dependent [199] and additionally, certain nanowire facets are more energetically favourable than others, thus an understanding of growth orientation and faceting is vital for growth engineering. One common method of controlling the orientation of Ge nanowires is through epitaxial growth from substrates such as GaAs (110) [100], Si(111) [200, 201] and Ge (111) [201].

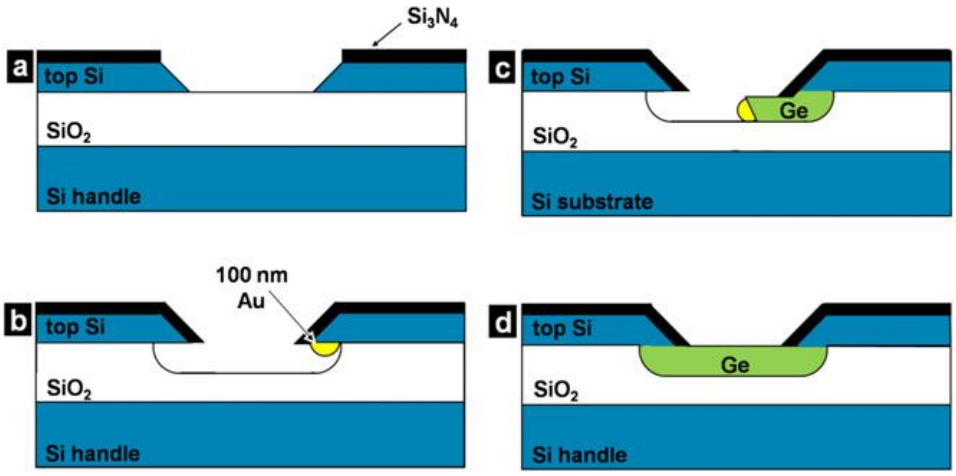


Figure 1.17 Process flow schematic: (a) SOI substrate etched with KOH, (b) selective deposition of Au nanoparticles on the exposed Si surfaces, (c) growth of guided Ge nanowires and (d) bridging Ge nanowires [202].

The underlying substrate orientation guides the crystallographic growth direction of the nanowires due to lattice matching. Ge nanowires have been observed to grow principally along the <110> direction from GaAs substrates whereas Si and Ge substrates commonly produce nanowires with a <111> growth direction. However, Ge(111) substrates have also been reported to yielding Ge nanowires with a predominately <110> orientation [201]. Ge nanowires with a <110> growth direction have also been synthesised by Quitoriano *et al.* [202] using SOITEC (001) oriented silicon-on-insulator substrates, as can be seen in figure 1.17. Nanowires could be reproducibly grown along the <110> direction and the authors compared this to unguided growth on a regular substrate in which the nanowires mostly adopted a

<111> orientation. As mentioned previously, solid phase seeding of Ge nanowires, via a VSS mechanism using Ni nanoparticles, could be used to control nanowire diameters [79]. A similar method was also used by Thombare *et al.*[203] to highlight that narrow diameter Ge nanowires (below 25 nm) adopted a predominantly <110> orientation and were free from kinks and defects, while larger diameter wires (above 25 nm) had a prevalent <111> orientation, with a high density of defects and kinks. This orientation dependence on diameter has previously been reported by Schmidt *et al*. [199] who also reported a transition diameter of around 25 nm. A prevailing <112> growth direction was observed for axially twinned Ge nanowires where {111} twin boundaries propagate along the length of the nanowires [76, 122]. Supersaturation controlled manipulation of the liquid-solid interface kinetics have previously been used previously to control orientations for GaAs nanowires [197], suggesting the method would also be applicable to Ge nanowire growth.

1.5.3 Heterostructures

Research into heterostructured nanowires has focused on forming compositionally abrupt interfaces between wire segments, which is vital for reproducible and predictable behaviour across nanowire junctions. Wen *et al.* [126] have investigated the use of Al-Au alloy catalyst particles to seed the growth of Si-Ge nanowires and form abrupt heterojunctions (see figure 1.18).

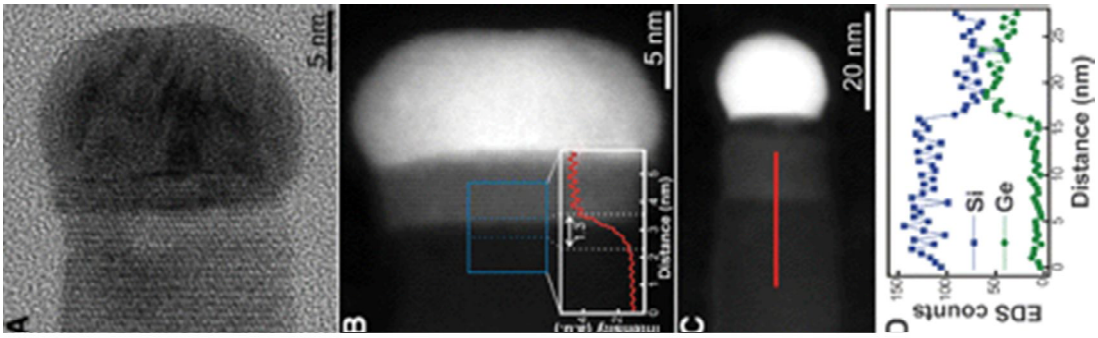


Figure 1.18 TEM and STEM analysis of a Si-Ge heterojunction nanowire . (A) High-resolution TEM image of a Si-Ge heterojunction nanowire. (B) High-angle annular dark-field scanning transmission electron microscopy (HAADF-STEM) image of a wire (diameter 17 nm). The inset shows the intensity profile across the interface, averaged over a 5-nm strip along the midpoint of the wire. The width of the interface is 1.3 nm. (C) HAADF-STEM image of a $Si/Si_{1-x}Ge_x$ nanowire (diameter 21 nm). (D) EDS line profile of Si andGe through the $Si/Si_{1-x}Ge_x$ junction, as indicated in (C), showing a sharp transition (less than 2 nm) from Si to SiGe. The composition of the $Si_{1-x}Ge_x$ alloy segment is estimated to be $Si_{0.7}Ge_{0.3}$. [126]

They confirm the ability to modulate the junction on the nanoscale via a VSS mechanism and obtain an interfacial abruptness of below 1 nm. The same group also reported the use of Ag-Au catalysts to control the heterojunction in Si-Ge nanowires [204] and the application of regular Au-Ge catalysts to form heterostructured nanowires of group 14 and III-V materials [205]. The abruptness of the heterojunction using the Ag-Au catalysts was approximately 1.3 nm and so offers similar benefits as the Al-Au alloy. Both the use of Ag-Au and Au-Al catalysts employ a VSS type growth mechanism (Ag-Au catalysts can also seed wires via a VLS mechanism, depending on which alloy composition is present) and have the advantage of very low solid solubility of Si and Ge in the seed metals. One of the primary disadvantages of the VSS mechanism is that it yields a lower nanowire growth rate compared to the VLS mechanism. An ideal scenario would be to take advantage of the standard VLS mechanism, to ensure a high growth rate, in combination with a VSS-type process to yield compositionally abrupt interfaces at the same time. Interestingly, Geaney *et al.*

have reported the VLS growth of Si-Ge nanowires with an interface abruptness of 1-2 atomic planes, confirmed by atomic-resolution electron energy loss spectroscopy (EELS) analysis [206].

In contrast to the highly abrupt interfaces reported above, Clark *et al.* [207] identified diffuse interfaces with noticeable broadening with increasing nanowire diameter. Interfacial broadening is normally due to the "reservoir" effect whereby a significant amount of the semiconductor material remains in the seed particle after the source of precursor has ceased, resulting in a compositional gradient at the junction between the two materials in question (in this case, Si and $Si_{1-x}Ge_x$). The broadening presents one of the fundamental challenges to the fabrication of abrupt heterojunctions. Dayeh *et al.* [208] report 100 % compositional modulation in Ge-Si nanowire heterostructures through Au catalysts via the VLS mechanism. Interfacial abruptness was not the focus of the report however, and this effect was not investigated in detail. Instead, the group studied defects in the stacking sequence and how they affected the TPB behaviour and nanowire morphology. Several reports have been published describing the interfacial abruptness from a theoretical/modelling point of view [209, 210], and this may be the most promising method of gaining greater insight into the formation of sharp interfaces.

Other interesting Ge nanowire heterostructures which have been investigated include Ge nanowire-$GeSiO_x$ nanotubes [211], radial core-shell heterostructures of Ge-SiO_x [91] and Ge-γAuGe nanowires [137]. In particular, the last report is of interest due to the presence of both stable and metastable phases in the same nanowire. The authors present a method to grow Ge nanowires with both stable and metastable phases via

the VLS mechanism. They heat the wires in-situ and observe how the liquid-solid interface expands into the nanowire due to the uptake of Ge into the seed. Interestingly, the interface does not recede upon cooling, but crystallises into metastable γAuGe with the top of the seed remaining in the liquid phase. The interface between the Ge and γAuGe appears to be about 1 nm in length which is comparable to reports already mentioned. [126, 204]

1.6 Conclusion and Outlook

The vast body of research that has accumulated over the past decade has made the semiconducting nanowire a strong candidate for future CMOS based devices [212]. The shift in the structure of the channel material in MOSFET devices from a planar configuration to architectures with reduced dimensionalities has necessitated the development of one-dimensional structures. As Ge shares many properties with Si, the material is sure to be at the forefront of any future developments. The wealth of synthetic methods available, the improved transport properties over Si and the ability to better control the morphology of Ge nanowires will ensure its placement as one of the leading materials for nanoscale development. Lieber *et al.* conclude that the three key ingredients to the nanowire system are the single-crystalline nature of the material, quantum confinement effects at narrow diameters and the ability to tailor the morphology of the nanowire itself [213]. The growth techniques employed along with an understanding of the growth kinetics and thermodynamics of the Au/Ge system are crucial to producing monocrystalline Ge and controlling the nanowire morphology, which in turn, is necessary to synthesise nanowires with highly uniform, narrow diameters so that these confinement effects can be taken advantage of. Consequently, this article has attempted to review these aspects which are most

critical to the advancement of Ge nanowire growth. The most common synthetic methods have been detailed as well as the most recent studies in dynamics and morphology control. As a result of the fundamental breakthroughs that have been achieved in these three main areas of Ge nanowire research over the last decade, the realisation of Ge nanowire based applications, such as lithium-ion batteries[21-23], field effect transistors (FETs)[24, 25], memory applications[26-28], photovoltaics[29, 30] and nanoelectromechanical systems (NEMS)[31, 32] draws ever closer.

Semiconducting nanowires can now be synthesised in large quantities using gas and solution based techniques, as evidenced by reports such as that by Wang *et al.* [59] which is promising for industry scale production. One key issue to address is the combination of top-down versus bottom up paradigms to produce Ge nanowires in large quantities and in controlled orientations and placements [5]. One of the most noteworthy publications that was mentioned in this article was the endotaxial growth of Ge via the VLS mechanism [55], which describes the growth of nanowires along a substrate, which results in aligned nanowires. Consequently, the combination of the scaling up methods developed by Wand *et al.* [59] and endotaxial growth along substrates may enable the simultaneous alignment of commercial scale quantities of Ge nanowires in the future. Li *et al* [55] report that the primary criteria to be satisfied include the dissolving of the catalyst into the substrate and the prevention of the catalyst from moving along the substrate. The use of substrates of sufficient size will also be necessary if large quantities are to be produced, but despite these limitations, this method holds substantial promise as a viable means to produce aligned Ge nanowires for commercial scale applications. Conversely, the ability to manufacture contacts and devices based on random nanowire networks [135] may

provide an interesting alternative to alignment, as this would eliminate the need to align the nanowires before integration.

Even as isolated architectures, Ge nanowires are ideal platforms for the investigation of material properties on the nanoscale. Accurate comparisons between bulk and nanoscale materials can be achieved through the investigation of nanowires, both via in-situ as they grow and ex-situ after growth has finished. Furthermore, additional aspects such as defect density, recombination processes and interface behaviour at heterojunctions need to be completely understood via isolated nanowire studies in order for these promising materials to be utilised to their full potential [50].

1.7 References

(1) Feynman, R. P., There's Plenty of Room at the Bottom. *Engineering and Science* 1960, pp 22.

(2) Moore, G. E. *Electronics* **1965,** 38, 114.

(3) *International Technology Roadmap for Semiconductors (ITRS), 2005 edition.*

(4) Vecchio, P. D., De-mystifying Software Performance Optimization. In http://software.intel.com/en-us/articles/: 2008.

(5) Hobbs, R. G.; Petkov, N.; Holmes, J. D. *Chem. Mater.* **2012,** 24, 1975.

(6) *International Technology Roadmap for Semiconductors (ITRS), 2009 edition.*

(7) Cao, G., Nanostructures and Nanomaterials: Synthesis, properties and applications. In Imperial College Press: 2004.

(8) Cui, Y.; Lieber, C. *Science* **2001,** 291, 851.

(9) Dubrovskii, V.; Cirlin, G.; Ustinov, V. *Semiconductors* **2009,** 43, 1539.

(10) Peng, K.; Xu, Y.; Wu, Y.; Yan, Y.; Lee, S.; Zhu, J. *Small* **2005,** 1, 1062.

(11) Duan, X.; Huang, Y.; Cui, Y.; Wang, J.; Lieber, C. *Nature* **2001,** 409, 66.

(12) J. Lee; S. Mahendra; Alvarez, P. J. J. *ACS Nano* **2010,** 4, 3580.

(13) A.I. Hochbaum; Yang, P. *Chem. Rev.* **2010,** 110, 527.

(14) Huang, Y.; Lieber, C. *Pure. Appl. Chem.* **2004,** 76, 2051.

(15) Barth, S.; Hernandez-Ramirez, F.; Holmes, J. D.; Romano-Rodriguez, A. *Prog. Mater. Sci.* **2010,** 55, 563.

(16) Yan, R.; Gargas, D.; Yang, P. *Nature Photon.* **2009,** 3, 569.

(17) Schaller, R. R. *Spectrum, IEEE* **1997,** 34, 52.

(18) Nguyen, P.; Ng, H.; Meyyappan, M. *Adv. Mater.* **2005,** 17, 549.

(19) Wu, X.; Kulkarni, J. S.; Collins, G.; Petkov, N.; Alme cija, D.; Boland, J. J.; Erts, D.; Holmes, J. D. *Chem. Mater.* **2008,** 20, 5954.

(20) Z Pei, L.; Y Cai, Z. *Recent Pat. Nanotechnol.* **2012,** 6, 44.

(21) Chockla, A. M.; Klavetter, K. C.; Mullins, C. B.; Korgel, B. A. *ACS Appl. Mater. Inter.* **2012,** 4, 4658.

(22) Seo, M. H.; Park, M.; Lee, K. T.; Kim, K.; Kim, J.; Cho, J. *Energy Environ. Sci.* **2011,** 4, 425.

(23) Chan, C. K.; Zhang, X. F.; Cui, Y. *Nano Lett.* **2008,** 8, 307.

(24) Le, S. T.; Jannaty, P.; Luo, X.; Zaslavsky, A.; Perea, D. E.; Dayeh, S. A.; Picraux, S. T. *Nano Lett.* **2012,** 12, 5850.

(25) Burchhart, T.; Lugstein, A.; Hyun, Y. J.; Hochleitner, G.; Bertagnolli, E. *Nano Lett.* **2009,** 9, 3739.

(26) Sun, X.; Yu, B.; Ng, G.; Meyyappan, M.; Ju, S.; Janes, D. B. *IEEE Trans. Electron Devices* **2008,** 55, 3131.

(27) Kim, S. B.; Zhang, Y.; McVittie, J. P.; Jagannathan, H.; Nishi, Y.; Wong, H. S. P. *IEEE Trans. Electron Devices* **2008,** 55, 2307.

(28) Jung, Y.; Nam, S. W.; Agarwal, R. *Nano Lett.* **2011,** 11, 1364.

(29) Garfunkel, E.; Mastrogiovanni, D.; Klein, L.; Wan, A.; Du Pasquier, A. *Abstr. Pap. Am. Chem. S.* **2008,** 236, 454.

(30) Pan, C.; Luo, Z.; Xu, C.; Luo, J.; Liang, R.; Zhu, G.; Wu, W.; Guo, W.; Yan, X.; Xu, J.; Wang, Z. L.; Zhu, J. *ACS Nano* **2011,** 5, 6629.

(31) Andzane, J.; Petkov, N.; Livshits, A. I.; Boland, J. J.; Holmes, J. D.; Erts, D. *Nano Lett.* **2009,** 9, 1824.

(32) Ziegler, K. J.; Lyons, D. M.; Holmes, J. D.; Erts, D.; Polyakov, B.; Olin, H.; Svensson, K.; Olsson, E. *Appl. Phys. Lett.* **2004,** 84, 4074.

(33) Xie, P.; Hu, Y.; Fang, Y.; Huang, J.; Lieber, C. M. *Proc. Natl. Acad. Sci. U S A.* **2009,** 106, 15254.

(34) Goldthorpe, I. A.; Marshall, A. F.; McIntyre, P. C. *Nano Lett.* **2008,** 8, 4081.

(35) Goldthorpe, I. A.; Marshall, A. F.; McIntyre, P. C. *Nano Lett.* **2009,** 9, 3715.

(36) Zhao, Y.; Smith, J. T.; Appenzeller, J.; Yang, C. *Nano Lett.* **2011,** 11, 1406.

(37) Amato, M.; Ossicini, S.; Rurali, R. *Nano Lett.* **2011,** 11, 594.

(38) Collins, G.; Holmes, J. D. *J. Mater. Chem.* **2011,** 21, 11052.

(39) Collins, G.; Fleming, P.; O'Dwyer, C.; Morris, M. A.; Holmes, J. D. *Chem. Mater.* **2011,** 23, 1883.

(40) Collins, G.; Koleśnik, M.; Krstić, V.; Holmes, J. D. *Chem. Mater.* **2010,** 22, 5235.

(41) Collins, G.; Fleming, P.; Barth, S.; O'Dwyer, C.; Boland, J. J.; Morris, M. A.; Holmes, J. D. *Chem. Mater.* **2010,** 22, 6370.

(42) Holmberg, V. C.; Rasch, M. R.; Korgel, B. A. *Langmuir* **2010,** 26, 14241.

(43) Morral, A. F. I.; Arbiol, J.; Prades, J. D.; Cirera, A.; Morante, J. R. *Adv. Mater.* **2007,** 19, 1347.

(44) Il Park, W.; Zheng, G. F.; Jiang, X. C.; Tian, B. Z.; Lieber, C. M. *Nano Lett.* **2008,** 8, 3004.

(45) Wei, D. P.; Chen, Q. *J. Phys. Chem. C* **2008,** 112, 15129.

(46) Wu, Y.; Yang, P. *J. Am. Chem. Soc.* **2001,** 123, 3165.

(47) Wang, D.; Dai, H. *Appl. Phys. A-Mater.* **2006,** 85, 217.

(48) Kamins, T.; Li, X.; Williams, R.; Liu, X. *Nano Lett.* **2004,** 4, 503.

(49) Wu, X. Y.; Kulkarni, J. S.; Collins, G.; Petkov, N.; Almecija, D.; Boland, J. J.; Erts, D.; Holmes, J. D. *Chem. Mater.* **2008,** 20, 5954.

(50) Sven Barth; Francisco Hernandez-Ramirez; Justin D. Holmes; Romano-Rodriguez, A. *Progress in Material Science* **2010,** 55, 563.

(51) Meyyappan, M.; Sunkara, M. K., *Inorganic Nanowires: Applications, Properties and Characterization.* CRC Press, Taylor and Francis Group: 2010.

(52) Choi, H. J. *Semiconductor Nanostructures for Optoelectronic Devices* **2012,** 1.

(53) Hammami, A.; Garnero, C. F.; Brewer, G.; McKeown, D. A.; Buechele, A.; Pegg, I. L.; Philip, J. *J. Phys. Chem. Solids* **2013,** 74, 40.

(54) Kamimura, H.; Araujo, L. S.; Berengue, O. M.; Amorim, C. A.; Chiquito, A. J.; Leite, E. R. *Physica E* **2011,** 44, 1776.

(55) Li, S.; Huang, X.; Liu, Q.; Cao, X.; Huo, F.; Zhang, H.; Gan, C. L. *Nano Lett.* **2012,** 12, 5565.

(56) Kim, J. H.; Moon, S. R.; Yoon, H. S.; Jung, J. H.; Kim, Y.; Chen, Z. G.; Zou, J.; Choi, D. Y.; Joyce, H. J.; Gao, Q.; Tan, H. H.; Jagadish, C. *Cryst. Growth. Des.* **2012,** 12, 135.

(57) Kim, J. H.; Moon, S. R.; Kim, Y.; Chen, Z. G.; Zou, J.; Choi, D. Y.; Joyce, H. J.; Gao, Q.; Tan, H. H.; Jagadish, C. *Nanotechnology* **2012,** 23, 115603.

(58) Simanullang, M.; Usami, K.; Kodera, T.; Uchida, K.; Oda, S. *Jpn. J. Appl. Phys.* **2011,** 50, 105002.

(59) Yang, H. J.; Tuan, H. Y. *J. Mater. Chem.* **2012,** 22, 2215.

(60) Pei, L. Z.; Zhao, H. S.; Tan, W.; Yu, H. Y.; Chen, Y. W.; Fan, C. G.; Zhang, Q.-F. *Mater. Charact.* **2009,** 60, 1400.

(61) Minh Tuan, D.; Petit, M.; Watanabe, A.; Michez, L.; Mendez, S. O.; Baghdad, R.; Vinh Le, T.; Coudreau, C. *J. Nanosci. Nanotechnol.* **2011,** 11, 9292.

(62) Marcus, I. C.; Berbezier, I.; Ronda, A.; Alonso, M. I.; Garriga, M.; Goñi, A. R.; Gomes, E.; Favre, L.; Delobbe, A.; Sudraud, P. *Cryst. Growth. Des.* **2011,** 11, 3190.

(63) Berbezier, I.; Ayoub, J.; Favre, L.; Ronda, A.; Morresi, L.; Pinto, N. *Surf. Sci.* **2011,** 605, 7.

(64) Li, X.; Meng, G.; Xu, Q.; Kong, M.; Zhu, X.; Chu, Z.; Li, A.-P. *Nano Lett.* **2011,** 11, 1704.

(65) Petkov, N.; Birjukovs, P.; Phelan, R.; Morris, M.; Erts, D.; Holmes, J. *Chem. Mater.* **2008,** 20, 1902.

(66) Pecora, E. F.; Irrera, A.; Artoni, P.; Boninelli, S.; Bongiorno, C.; Spinella, C.; Priolo, F. *Electrochem. Solid St.* **2010,** 13, K53.

(67) Kumar, R. R.; Yuvaraj, D.; Rao, K. N. *Mater. Lett.* **2010,** 64, 1766.

(68) Sutter, E.; Sutter, P. *Appl. Phys. A-Mater.* **2010,** 99, 217.

(69) Sutter, E.; Ozturk, B.; Sutter, P. *Nanotechnology* **2008,** 19, 435607.

(70) Mullane, E.; Geaney, H.; Ryan, K. M. *Chem. Commun.* **2012,** 48, 5446.

(71) Gu, J.; Collins, S. M.; Carim, A. I.; Hao, X.; Bartlett, B. M.; Maldonado, S. *Nano Lett.* **2012,** 12, 4617.

(72) Chockla, A. M.; Korgel, B. A. *J. Mater. Chem.* **2009,** 19, 996.

(73) Carim, A. I.; Collins, S. M.; Foley, J. M.; Maldonado, S. *J. Am. Chem. Soc.* **2011,** 133, 13292.

(74) Pei, L. Z.; Zhao, H. S.; Tan, W.; Yu, H. Y.; Chen, Y. W.; Wang, J. F.; Fan, C. G.; Chen, J.; Zhang, Q.-F. *Mater. Res. Bull.* **2010,** 45, 153.

(75) Wen, B.; Huang, Y.; Boland, J. J. *J. Mater. Chem.* **2008,** 18, 2011.

(76) Biswas, S.; Singha, A.; Morris, M. A.; Holmes, J. D. *Nano Lett.* **2012,** 12, 5654.

(77) Hobbs, R. G.; Barth, S.; Petkov, N.; Zirngast, M.; Marschner, C.; Morris, M. A.; Holmes, J. D. *J. Am. Chem. Soc* **2010**, 132, 13742.

(78) Lotty, O.; Hobbs, R.; O'Regan, C.; Hlina, J.; Marschner, C.; O'Dwyer, C.; Petkov, N.; Holmes, J. D. *Chem. Mater.* **2012,** 25, 215.

(79) Barth, S.; Kolesnik, M. M.; Donegan, K.; Krstic, V.; Holmes, J. D. *Chem. Mater.* **2011,** 23, 3335.

(80) Smith, D. A.; Holmberg, V. C.; Rasch, M. R.; Korgel, B. A. *J. Phys. Chem. C* **2010,** 114, 20983.

(81) Wagner, R. S.; Ellis, W. C. *Appl. Phys. Lett.* **1964,** 4, 89.

(82) Schmidt, V.; Gösele, U. *Science* **2007,** 316, 698.

(83) Gamalski, A.; Ducati, C.; Hofmann, S. *J. Phys. Chem. C* **2011,** 115, 4413.

(84) Zahedifar, M.; Hosseinmardi, F.; Eshraghi, L.; Ganjipour, B. *Radiat. Phys. Chem.* **2011,** 80, 324.

(85) Le, S. T.; Jannaty, P.; Zaslavsky, A.; Dayeh, S. A.; Picraux, S. T. *Appl. Phys. Lett.* **2010,** 96, 262102.

(86) Kolíbal, M.; Vystavel, T.; Novák, L.; Mach, J.; Sikola, T. *Appl. Phys. Lett.* **2011,** 99, 143113.

(87) Bryce, B. A.; Levendorf, M. P.; Park, J.; Tiwari, S. *Electrochem. Solid St.* **2010,** 13, K77.

(88) Huang, J.; Chim, W. K.; Wang, S.; Chiam, S. Y.; Wong, L. M. *Nano Lett.* **2009,** 9, 583.

(89) Drinek, V.; Subrt, J.; Klementova, M.; Fajgar, R. *J. Anal. Appl. Pyrol.* **2010,** 89, 255.

(90) Pandurangan, A.; Morin, C.; Qian, D.; Andrews, R.; Crocker, M. *Carbon* **2009,** 47, 1708.

(91) Arnold, D. C.; Hobbs, R. G.; Zirngast, M.; Marschner, C.; Hill, J. J.; Ziegler, K. J.; Morris, M. A.; Holmes, J. D. *J. Mater. Chem.* **2009,** 19, 954.

(92) Hawley, C. J.; McGuckin, T.; Spanier, J. E. *Cryst. Growth. Des.* **2013,** 13, 491.

(93) Jung, J. H.; Yoon, H. S.; Kim, Y. L.; Song, M. S.; Kim, Y.; Chen, Z. G.; Zou, J.; Choi, D. Y.; Kang, J. H.; Joyce, H. J.; Gao, Q.; Hoe Tan, H.; Jagadish, C. *Nanotechnology* **2010,** 21, 295602.

(94) Greytak, A. B.; Lauhon, L. J.; Gudiksen, M. S.; Lieber, C. M. *Appl. Phys. Lett.* **2004,** 84, 4176.

(95) Gunji, M.; Thombare, S. V.; Hu, S.; McIntyre, P. C. *Nanotechnology* **2012,** 23, 385603.

(96) Zhang, R. Q.; Lifshitz, Y.; Lee, S. T. *Adv. Mater.* **2003,** 15, 635.

(97) Wang, N.; Tang, Y. H.; Zhang, Y. F.; Lee, C. S.; Lee, S. T. *Phys. Rev. B* **1998,** 58, 16024.

(98) Simanullang, M.; Usami, K.; Kodera, T.; Uchida, K.; Oda, S. *J. Nanosci. Nanotechnol.* **2011,** 11, 8163.

(99) Sierra-Sastre, Y.; Choi, S.; Picraux, S.; Batt, C. A. *J. Am. Chem. Soc.* **2008,** 130, 10488.

(100) Song, M. S.; Jung, J. H.; Kim, Y.; Wang, Y.; Zou, J.; Joyce, H.; Gao, Q.; Tan, H.; Jagadish, C. *Nanotechnology* **2008,** 19, 125602.

(101) Li, C.; Usami, K.; Yamahata, G.; Tsuchiya, Y.; Mizuta, H.; Oda, S. *Appl. Phys. Express* **2009,** 2, 015004.

(102) Smith, D. A.; Holmberg, V. C.; Korgel, B. A. *ACS Nano* **2010,** 4, 2356.

(103) Holmes, J. D.; Lyons, D. M.; Ziegler, K. J. *Chem. Eur. J.* **2003,** 9, 2144.

(104) van der Meulen, M. I.; Petkov, N.; Morris, M. A.; Kazakova, O.; Han, X.; Wang, K. L.; Jacob, A. P.; Holmes, J. D. *Nano Lett.* **2008,** 9, 50.

(105) Grossi, V.; Bussolotti, F.; Passacantando, A.; Santucci, S.; Ottaviano, L. *Superlattice. Microst.* **2008,** 44, 489.

(106) Lensch-Falk, J. L.; Hemesath, E. R.; Lauhon, L. J. *Nano Lett.* **2008,** 8, 2669.

(107) Allen, J. E.; Hemesath, E. R.; Perea, D. E.; Lensch-Falk, J. L.; Li, Z.; Yin, F.; Gass, M. H.; Wang, P.; Bleloch, A. L.; Palmer, R. E. *Nature Nanotech.* **2008,** 3, 168.

(108) Hemesath, E. R.; Schreiber, D. K.; Gulsoy, E. B.; Kisielowski, C. F.; Petford-Long, A. K.; Voorhees, P. W.; Lauhon, L. J. *Nano Lett.* **2011,** 12, 167.

(109) Woodruff, J. H.; Ratchford, J. B.; Goldthorpe, I. A.; McIntyre, P. C.; Chidsey, C. E. D. *Nano Lett.* **2007,** 7, 1637.

(110) Hou, W.-C.; Chen, L.-Y.; Tang, W.-C.; Hong, F. C. N. *Cryst. Growth. Des.* **2011,** 11, 990.

(111) Ross, F. M.; Wen, C. Y.; Kodambaka, S.; Wacaser, B. A.; Reuter, M. C.; Stach, E. A. *Philos. Mag.* **2010,** 90, 2807.

(112) Lensch-Falk, J. L.; Hemesath, E. R.; Perea, D. E.; Lauhon, L. J. *J. Mater. Chem.* **2009,** 19, 849.

(113) Xiang, Y.; Cao, L.; Arbiol, J.; Brongersma, M. L.; Fontcuberta i Morral, A. *Appl. Phys. Lett.* **2009,** 94, 163101.

(114) Lee, M.-K.; Kim, T. G.; Ju, B.-K.; Sung, Y.-M. *Cryst. Growth. Des.* **2009,** 9, 938.

(115) Yan, C.; Lee, P. S. *J. Phys. Chem. C* **2009,** 113, 2208.

(116) Xiang, Y.; Cao, L.; Conesa-Boj, S.; Estrade, S.; Arbiol, J.; Peiro, F.; Heiss, M.; Zardo, I.; Morante, J. R.; Brongersma, M. L.; Fontcuberta I Morral, A. *Nanotechnology* **2009,** 20, 245608.

(117) Geaney, H.; Kennedy, T.; Dickinson, C.; Mullane, E.; Singh, A.; Laffir, F.; Ryan, K. M. *Chem. Mater.* **2012,** 24, 2204.

(118) Mullane, E.; Kennedy, T.; Geaney, H.; Dickinson, C.; Ryan, K. M. *Chem. Mater.* **2013,** 25, 1816.

(119) Kang, K.; Kim, D. A.; Lee, H. S.; Kim, C. J.; Yang, J. E.; Jo, M. H. *Adv. Mater.* **2008,** 20, 4684.

(120) Kang, K.; Gu, G. H.; Kim, D. A.; Park, C. G.; Jo, M. H. *Chem. Mater.* **2008,** 20, 6577.

(121) Connell, J. G.; Al Balushi, Z. Y.; Sohn, K.; Huang, J.; Lauhon, L. J. *J. Phys. Chem. Lett.* **2010,** 1, 3360.

(122) Barth, S.; Boland, J. J.; Holmes, J. D. *Nano Lett.* **2011,** 11, 1550.

(123) Mohammad, S. N. *J. Chem. Phys.* **2009,** 131, 224702.

(124) Hofmann, S.; Sharma, R.; Wirth, C. T.; Cervantes-Sodi, F.; Ducati, C.; Kasama, T.; Dunin-Borkowski, R. E.; Drucker, J.; Bennett, P.; Robertson, J. *Nature Mater.* **2008,** 7, 372.

(125) Lu, X.; Harris, J. T.; Villareal, J. E.; Chockla, A. M.; Korgel, B. A. *Chem. Mater.* **2013,** 25, 2172.

(126) Wen, C. Y.; Reuter, M.; Bruley, J.; Tersoff, J.; Kodambaka, S.; Stach, E.; Ross, F. *Science* **2009,** 326, 1247.

(127) Geaney, H.; Dickinson, C.; Barrett, C. A.; Ryan, K. M. *Chem. Mater.* **2011,** 23, 4838.

(128) Krabac, L.; Klementova, M.; Subrt, J.; Fajgar, R.; Kupcik, J.; Bastl, Z.; Stuchlikova, T. H.; Drinek, V. *J. Anal. Appl. Pyrol.* **2012,** 97, 94.

(129) Drinek, V.; Fajgar, R.; Klementova, M.; Subrt, J. *J. Electrochem. Soc.* **2010,** 157, K218.

(130) Tao, Y.; Zhang, G.; Xia, Y.; Wang, H.; Gong, F.; Wu, H.; Tao, G. *Mater. Chem. Phys.* **2010,** 121, 230.

(131) Shu Hu; Paul W. Leu; Ann F. Marshall; McIntyre, P. C. *Nature Nanotech.* **2009,** 4, 649.

(132) Al-Salman, R.; Mallet, J.; Molinari, M.; Fricoteaux, P.; Martineau, F.; Troyon, M.; El Abedin, S. Z.; Endres, F. *Phys. Chem. Chem. Phys.* **2008,** 10, 6233.

(133) Dailey, E.; Drucker, J. *J. Appl. Phys.* **2009,** 105, 064317.

(134) Kim, B. S.; Koo, T. W.; Lee, J. H.; Kim, D. S.; Jung, Y. C.; Hwang, S. W.; Choi, B. L.; Lee, E. K.; Kim, J. M.; Whang, D. *Nano Lett.* **2009,** 9, 864.

(135) De, S.; Higgins, T. M.; Lyons, P. E.; Doherty, E. M.; Nirmalraj, P. N.; Blau, W. J.; Boland, J. J.; Coleman, J. N. *ACS Nano* **2009,** 3, 1767.

(136) Adhikari, H.; Marshall, A.; Goldthorpe, I.; Chidsey, C.; McIntyre, P. *ACS Nano* **2007,** 1, 415.

(137) Sutter, E.; Sutter, P. *Nanotechnology* **2011,** 22, 295605.

(138) Sutter, E. A.; Sutter, P. W. *ACS Nano* **2010,** 4, 4943.

(139) Sutter, E.; Sutter, P. *Nano Lett.* **2008,** 8, 411.

(140) Homberg, V. C.; Panthani, M. G.; Korgel, B. A. *Science* **2009,** 326, 405.

(141) Kim, B. J.; Tersoff, J.; Kodambaka, S.; Reuter, M. C.; Stach, E. A.; Ross, F. M. *Science* **2008,** 322, 1070.

(142) Kryshtal, A. P.; Sukhov, R. V.; Minenkov, A. A. *J. Alloy. Compd.* **2012,** 512, 311.

(143) Chueh, Y. L.; Boswell, C. N.; Yuan, C. W.; Shin, S. J.; Takei, K.; Ho, J. C.; Ko, H.; Fan, Z.; Haller, E.; Chrzan, D. *Nano Lett.* **2010,** 10, 393.

(144) Jung, S. J.; Lutz, T.; Boese, M.; Holmes, J. D.; Boland, J. J. *Nano Lett.* **2011,** 11 1294.

(145) Chidambaram, V.; Yeung, H. B.; Shan, G. *J. Electron. Mater.* **2012,** 41, 2107.

(146) Chidambaram, V.; Hald, J.; Hattel, J. *J. Alloy. Compd.* **2010,** 490, 170.

(147) Leinenbach, C.; Valenza, F.; Giuranno, D.; Elsener, H. R.; Jin, S.; Novakovic, R. *J. Electron. Mater.* **2011,** 40, 1533.

(148) Pasturel, A.; Jakse, N. *Phys. Rev. B* **2011,** 84, 134201

(149) Tasci, E. S.; Sluiter, M. H. F.; Pasturel, A.; Jakse, N. *Phys. Rev. B* **2010,** 81, 172202

(150) Takeda, S.; Fujii, H.; Kawakita, Y.; Tahara, S.; Nakashima, S.; Kohara, S.; Itou, M. *J. Alloy. Compd.* **2008,** 452, 149.

(151) Hajjar, S.; Garreau, G.; Josien, L.; Bubendorff, J. L.; Berling, D.; Mehdaoui, A.; Pirri, C.; Maroutian, T.; Renard, C.; Bouchier, D.; Petit, M.; Spiesser, A.; Dau, M. T.; Michez, L.; Le Thanh, V.; Mentes, T. O.; Nino, M. A.; Locatelli, A. *Phys. Rev. B* **2011,** 84, 125325.

(152) Chirawatkul, P.; Zeidler, A.; Salmon, P. S.; Takeda, S. i.; Kawakita, Y.; Usuki, T.; Fischer, H. E. *Phys. Rev. B* **2011,** 83, 014203.

(153) Hoepfner, P.; Schaefer, J.; Fleszar, A.; Meyer, S.; Blumenstein, C.; Schramm, T.; Hessmann, M.; Cui, X.; Patthey, L.; Hanke, W.; Claessen, R. *Phys. Rev. B* **2011,** 83, 235435.

(154) Marshall, A. F.; Goldthorpe, I. A.; Adhikari, H.; Koto, M.; Wang, Y.-C.; Fu, L.; Olsson, E.; McIntyre, P. C. *Nano Lett.* **2010,** 10, 3302.

(155) Jin, S.; Duarte, L. I.; Huang, G.; Leinenbach, C. *Monatsh. Chem.* **2012,** 143, 1263.

(156) Wang, J.; Liu, Y. J.; Tang, C. V.; Liu, L. B.; Zhou, H. Y.; Jin, Z. P. *Thermochim. Acta.* **2011,** 512, 240.

(157) Wang, J.; Leinenbach, C.; Roth, M. *J. Alloy. Compd.* **2009,** 485, 577.

(158) Wang, J.; Leinenbach, C.; Roth, M. *J. Alloy. Compd.* **2009,** 481, 830.

(159) Wacaser, B. A.; Dick, K. A.; Johansson, J.; Borgström, M. T.; Deppert, K.; Samuelson, L. *Adv. Mater.* **2009,** 21, 153.

(160) Schwarz, K.; Tersoff, J. *Nano Lett.* **2010,** 11, 316.

(161) Dubrovskii, V. G.; Cirlin, G. E.; Sibirev, N. V.; Jabeen, F.; Harmand, J. C.; Werner, P. *Nano Lett.* **2011,** 11, 1247.

(162) Eisenhawer, B.; Sivakov, V.; Christiansen, S.; Falk, F. *Nano Lett.* **2013,** 13, 873.

(163) Shakthivel, D.; Raghavan, S. *J. Appl. Phys.* **2012,** 112, 024317.

(164) Lü, Y.; Cui, H.; Yang, G.; Wang, C. X. *Nano Lett.* **2012,** 12, 4032.

(165) Artoni, P.; Pecora, E. F.; Irrera, A.; Priolo, F. *Nanoscale Res. Lett.* **2011,** 6, 1.

(166) Schwarz, K.; Tersoff, J. *Phys. Rev. Lett.* **2009,** 102, 206101.

(167) Schmidt, V.; Wittemann, J. V.; Senz, S.; Gösele, U. *Adv. Mater.* **2009,** 21, 2681.

(168) Wen, C. Y.; Tersoff, J.; Reuter, M.; Stach, E.; Ross, F. *Phys. Rev. Lett.* **2010,** 105, 195502.

(169) Wang, N.; Cai, Y.; Zhang, R. *Mater. Sci. Eng., R* **2008,** 60, 1.

(170) Gamalski, A.; Tersoff, J.; Sharma, R.; Ducati, C.; Hofmann, S. *Phys. Rev. Lett.* **2012,** 108, 255702.

(171) Gamalski, A. D.; Tersoff, J.; Sharma, R.; Ducati, C.; Hofmann, S. *Nano Lett.* **2010,** 10, 2972.

(172) Woehl, T. J.; Evans, J. E.; Arslan, I.; Ristenpart, W. D.; Browning, N. D. *ACS Nano* **2012,** 6, 8599.

(173) Nikolova, L.; LaGrange, T.; Reed, B.; Stern, M.; Browning, N.; Campbell, G.; Kieffer, J.-C.; Siwick, B.; Rosei, F. *Appl. Phys. Lett.* **2010,** 97, 203102.

(174) Ross, F. M. *Rep. Prog. Phys.* **2010,** 73, 114501.

(175) Givargizov, E. I. *J. Cryst. Growth* **1975,** 31, 20.

(176) Sa, I.; Lee, B.-M.; Kim, C.-J.; Jo, M.-H.; Lee, B.-J. *Calphad* **2008,** 32, 669.

(177) Edwin J. Schwalbach; Voorhees, P. W. *Nano Lett.* **2008,** 8, 3739.

(178) Kim, B.-S.; Lee, J.-H.; Son, K.; Hwang, S. W.; Choi, B. L.; Lee, E. K.; Kim, J. M.; Whang, D. *ACS Appl. Mater. Inter.* **2012,** 4, 805.

(179) Dayeh, S. A.; Mack, N. H.; Huang, J. Y.; Picraux, S. *Appl. Phys. Lett.* **2011,** 99, 023102.

(180) den Hertog, M. I.; Rouviere, J.-L.; Dhalluin, F.; Desré, P. J.; Gentile, P.; Ferret, P.; Oehler, F.; Baron, T. *Nano Lett.* **2008,** 8, 1544.

(181) Zhang, J. J.; Katsaros, G.; Montalenti, F.; Scopece, D.; Rezaev, R. O.; Mickel, C.; Rellinghaus, B.; Miglio, L.; De Franceschi, S.; Rastelli, A.; Schmidt, O. G. *Phys. Rev. Lett.* **2012,** 108, 085502

(182) Dayeh, S. A.; Picraux, S. *Nano Lett.* **2010,** 10, 4032.

(183) Renard, C.; Boukhicha, R.; Gardes, C.; Fossard, F.; Yam, V.; Vincent, L.; Bouchier, D.; Hajjar, S.; Bubendorff, J. L.; Garreau, G.; Pirri, C. *Thin Solid Films* **2012,** 520, 3314.

(184) Porret, C.; Devillers, T.; Jain, A.; Dujardin, R.; Barski, A. *J. Cryst. Growth* **2011,** 323, 334.

(185) Kim, B. J.; Wen, C. Y.; Tersoff, J.; Reuter, M. C.; Stach, E. A.; Ross, F. M. *Nano Lett.* **2012,** 12, 5867.

(186) Zhang, X.; Lew, K.-K.; Nimmatoori, P.; Redwing, J. M.; Dickey, E. C. *Nano Lett.* **2007,** 7, 3241.

(187) Johansson, J.; Svensson, C. P. T.; Mårtensson, T.; Samuelson, L.; Seifert, W. *J. Phys. Chem. B* **2005,** 109, 13567.

(188) Persson, A. I.; Larsson, M. W.; Stenström, S.; Ohlsson, B. J.; Samuelson, L.; Wallenberg, L. R. *Nature Mater.* **2004,** 3, 677.

(189) Kuo-Chang Lu, W.-W. W., Hao Ouyang, Yung-Chen Lin, Yu Huang, Chun-Wen Wang,; Zheng-Wei Wu, C.-W. H., Lih J. Chen and K. N. Tu. *Nano Lett.* **2011,** 11, 2753.

(190) Geaney, H.; Dickinson, C.; Weng, W.; Kiely, C. J.; Barrett, C. A.; Gunning, R. D.; Ryan, K. M. *Cryst. Growth. Des.* **2011,** 11, 3266.

(191) Tian, B.; Cohen-Karni, T.; Qing, Q.; Duan, X.; Xie, P.; Lieber, C. M. *Science* **2010,** 329, 830.

(192) Yang, Z.; Veinot, J. G. C. *J. Mater. Chem.* **2011,** 21, 16505.

(193) Kim, B.-S.; Kim, M. J.; Lee, J. C.; Hwang, S. W.; Choi, B. L.; Lee, E. K.; Whang, D. *Nano Lett.* **2012,** 12, 4007.

(194) Takagi, D.; Kobayashi, Y.; Hibino, H.; Suzuki, S.; Homma, Y. *Nano Lett.* **2008,** 8, 832.

(195) Yoshihara, N.; Ago, H.; Tsuji, M. *Jpn. J. Appl. Phys.* **2008,** 47, 1944.

(196) Dubrovskii, V.; Xu, T.; Lambert, Y.; Nys, J. P.; Grandidier, B.; Stiévenard, D.; Chen, W.; Pareige, P. *Phys. Rev. Lett.* **2012,** 108, 105501.

(197) Han, N.; Wang, F.; Hou, J. J.; Yip, S. P.; Lin, H.; Fang, M.; Xiu, F.; Shi, X.; Hung, T. F.; Ho, J. C. *Cryst. Growth. Des.* **2012,** 12 6243.

(198) Fortuna, S. A.; Li, X. *Semicond. Sci. Technol.* **2010,** 25, 024005.

(199) Schmidt, V.; Senz, S.; Gosele, U. *Nano Lett.* **2005,** 5, 931.

(200) Park, S. J.; Chung, S. H.; Kim, B. J.; Qi, M.; Xu, X.; Stach, E. A.; Yang, C. *J. Mater. Res.* **2011,** 26, 2744.

(201) Kramer, A.; Albrecht, M.; Boeck, T.; Remmele, T.; Schramm, P.; Fornari, R. *Superlattice. Microst.* **2009,** 46, 277.

(202) Quitoriano, N. J.; Kamins, T. I. *Nanotechnology* **2011,** 22, 065201.

(203) Thombare, S. V.; Marshall, A. F.; McIntyre, P. C. *J. Appl. Phys.* **2012,** 112, 054325

(204) Chou, Y.-C.; Wen, C.-Y.; Reuter, M. C.; Su, D.; Stach, E. A.; Ross, F. M. *ACS Nano* **2012,** 6, 6407.

(205) Hillerich, K.; Dick, K. A.; Wen, C.-Y.; Reuter, M. C.; Kodambaka, S.; Ross, F. M. *Nano Lett.* **2013,** 13, 903.

(206) Geaney, H.; Mullane, E.; Ramasse, Q. M.; Ryan, K. M. *Nano Lett.* **2013,** 13, 1675.

(207) Clark, T. E.; Nimmatoori, P.; Lew, K.-K.; Pan, L.; Redwing, J. M.; Dickey, E. C. *Nano Lett.* **2008,** 8, 1246.

(208) Dayeh, S. A.; Wang, J.; Li, N.; Huang, J. Y.; Gin, A. V.; Picraux, S. T. *Nano Lett.* **2011,** 11, 4200.

(209) Vastola, G.; Shenoy, V. B.; Zhang, Y. W. *J. Appl. Phys.* **2012,** 112, 064311.

(210) Dayeh, S. A.; Gin, A. V.; Picraux, S. T. *Appl. Phys. Lett.* **2011,** 98, 163112.

(211) Huang, J. Q.; Chiam, S. Y.; Chim, W. K.; Wong, L. M.; Wang, S. J. *Nanotechnology* **2009,** 20, 425604.

(212) Yang, P.; Yan, R.; Fardy, M. *Nano Lett.* **2010,** 10, 1529.

(213) Lu, W.; Lieber, C. M. *J. Phys. D: Appl. Phys.* **2006,** 39, R387.

Experimental Methods

2

2.1 Synthesis of Germanium Nanowires from Bilayer Films

2.1.1 Si Substrates and Preparation of Diphenylgermane Solution

Si(100) substrates were coated with a 5 nm Au film using a Cressington HR 208 sputter coater with a quartz crystal thickness monitor. The target was placed inside the instrument and the pressure pumped down to 0.01 mbar. The density of Ge was then entered into the thickness monitor and the current set to 60 mA. Ar gas was then bled into the chamber. With the shutter closed, 1-2 nm of Ge was removed from the target to remove the surface oxide. The shutter was opened and the Ge deposited with the thickness being monitored in real time. Three samples consisting of a layer of Ge with thicknesses of 1, 2 and 5 nm were prepared by depositing such a layer on one half of the substrate, forming a Au/Ge bilayer. Diphenylgermane (DPG) was used as the precursor for Ge nanowire growth. Solutions of DPG in anhydrous toluene were prepared in an N_2 glove box with a typical concentration of 1.07×10^{-4} M.

2.1.2 Germanium Nanowire Synthesis

Continuous-flow reactions were carried out in a toluene medium using a liquid injection chemical vapor deposition (LICVD) technique. The as-prepared Au/Ge sputtered Si substrates were loaded into a stainless steel micro reactor cell connected by metal tubing. The reaction cell and connections were dried for 24 h at 180 ºC under vacuum. A solution of diphenyl germane (DPG) was loaded into a Hamilton GASTIGHT(R) sample-lock syringe (1000 series) inside a nitrogen filled glovebox under stringent precautions against water. Prior to DPG injection, the coated Si substrate was annealed for 30 min at 430 ºC (well above the nominal Au/Ge eutectic temperature) under a flowing H_2/Ar (flow rate of 0.5 ml min^{-1}) atmosphere inside a

tube furnace. The precursor solution was then injected into the metal reaction cell using a high precision syringe pump at a rate of 0.025 ml min^{-1}. H_2/Ar flow was maintained during the entire growth period. Typical growth times were 25 min, though the times were varied to study the effect on nanowire length. The cell was allowed to cool down to room temperature and disassembled to access the growth substrate. Nanowires were washed with dry toluene and dried under N_2 flow for further characterisation.

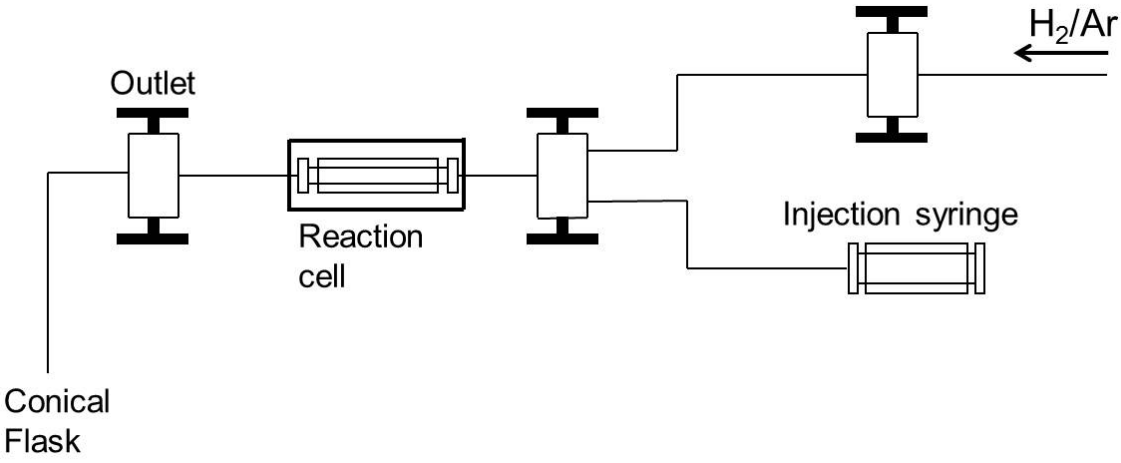


Figure 2.1. Schematic of the liquid-injection chemical vapour deposition set-up used to synthesise germanium nanowires.

2.1.3 Electron Microscopy Characterisation of Germanium Nanowires

Structural characterisation was carried out using scanning electron microscopy (SEM), transmission electron microscopy (TEM), energy dispersive X-ray (EDX) analysis and selective area electron diffraction (SAED). SEM was carried out on a FEI Quanta FEG 650 operating at 5-10 kV. Bright-field TEM, in-situ temperature dependent studies and SAED were carried out on a JEOL JEM 2100 transmission electron microscope operating at 200 kV, while EDX was carried out using an Oxford Instruments INCA energy system fitted to the TEM. For TEM characterisation, nanowires were dispersed in isopropanol and dropped onto lacey carbon 400 mesh copper grids. Bilayer and nanowire cross-sections were prepared on a FEI Helios Nanolab^{TM} dual-beam SEM/FIB suite using a standard lift-out technique similar to that described elsewhere [1].

Nanowire length and diameters were obtained using phase-contrast TEM. The sonication method represents a source of error for obtaining nanowire lengths as the lengths measured using the TEM might not be representative of the original lengths after growth. This is due to the fact that sonication may cause the loss of structural integrity of the nanowires as they break away from the substrate and are dispersed in solution. To minimise this effect, the sonication time was no more than 5 seconds.

In-situ TEM was carried out using a Gatan Model 628 single-tilt heating holder. Au and Au/Ge bi-layer films were sputtered onto PELCO ® 18nm silicon dioxide support films (Ted Pella) on a 3 mm grid consisting of 60 x 60 μm apertures on a 0.5 x 0.5 mm window. The sputtering process was identical to that described above. The grid was placed inside the holder between two washers and was kept in place using a beryllium hexaring. Images were taken at room temperature after which the

temperature was raised to 300 ^{o}C using a Gatan Model 901 SmartSet hot stage controller. The temperature was then ramped from 300 ^{o}C up to 800 ^{o}C with an image being taken every 10 ^{o}C. Each temperature was maintained for approximately 3 minutes. Dark-field imaging was used to compare the alloying process of the Au and Au/Ge bi-layer films as this mode eliminates mass-thickness contrast. Dark-field imaging was obtained as follows: first, a diffraction pattern was formed from the image in question by inserting the selected area diffraction aperture. The diffracted electrons in the selected-area electron diffraction pattern (SADP) were chosen by inserting an objective aperture into the back focal plane of the objective lens. The aperture was then used to select one of the diffracted beams.

2.2 Synthesis of Germanium Nanowires from Evaporated Films

2.1.1 Evaporation of Au, Ag and Ge films

Au, Au/Ag and Au/Ag/Ge films (Au = 10 nm, Ag = 3 nm and Ge = 4 or 6 nm) were evaporated onto Si/SiO_2 substrates (the SiO_2 layer was 200 nm) using a Temescal FC2000 e-beam evaporation system. The substrates were first treated with a 30 s in-situ Ar ion etch to improve adhesion. The metals were then evaporated at a rate of 1 Å s^{-1}.

2.2.2 Preparation of Au and $Au_{0.75}Ag_{0.25}$ particles

Au and $Au_{0.75}Ag_{0.25}$ nanoparticles used as growth promoters were prepared using a method outlined previously by Liu *et al* [2]. Briefly, 0.3 mmol of $HAuCl_4.3H_2O$ (for Au nanoparticles) and 0.225 mmol of $HAuCl_4.3H_2O$ with 0.075 mmol of silver acetate (for $Au_{0.75}Ag_{0.25}$ nanoparticles) were mixed with 2 ml oleylamine, 1 ml oleic acid and 10 ml phenyl ether under an Ar atmosphere and heated to 150 °C with

constant stirring. The solutions were kept at that temperature for 4 hr and then cooled to room temperature. Nanoparticles were precipitated and cleaned with ethanol and dispersed in toluene for further use as catalysts for nanowire growth.

For the particle seeded growth, Au and $Au_{0.75}Ag_{0.25}$ particles were drop-cast onto SiO_2/Si substrates coated with 6 nm of evaporated Ge. Ge thin film coated substrates were pre-treated by dipping in a 1 % HF solution for 30 s to remove the native GeO_2 layer. The particle solutions were then drop-casted onto the substrate and dried under nitrogen. Nanoparticle coated substrates were placed inside a stainless steel micro reactor cell attached with high precision needle valves. The synthesis was carried out as described above for bi-layer films. UV-Vis absorbance spectroscopy of the Au and $Au_{0.75}Ag_{0.25}$ particles was carried out using an Agilent Technologies Varian Cary 50 UV-Vis spectrophotometer.

2.2.3 Electron Microscopy Characterisation of Germanium Nanowires

Electron microscopy characterisation was carried out as described above. In-situ TEM was carried out using a Gatan Model 628 single-tilt heating holder. Nanowires were dispersed in isopropanol and dropped onto lacey carbon 400 mesh copper grids. Nanowires of various diameters synthesised from both Au and Au_xAg_{1-x} alloy nanoparticles were selected for heating experiments. The grids were placed in the holder and room temperature images of the nanowire seeds were taken using bright-field TEM mode. Bright-field TEM mode is obtained in the same fashion described above for dark-field mode, but with the objective aperture centered over the spot representing the direct electron beam. The temperature was then raised to the growth temperature of 465 ^{o}C (without ramping) using a Gatan Model 901 SmartSet hot

stage controller. Images were taken of the selected nanowires at this temperature before being allowed to cool down.

2.3 Pt Interconnect Deposition

All Pt interconnect depositions were performed on a FEI Helios NanoLab^{TM} Dual-Beam instrument using an acceleration voltage of 5 kV. Deposition dwell time was set at 5.0 μs with a multi-pass serpentine scan type and the distance from the GIS to the sample was 200 μm for all depositions. The pixel distance spacing was 11.54 nm for the $Pt(PF_3)_4$ precursor and 23.07 nm for the $(CH_3)_3Pt(C_pCH_3)$ precursor. The sample substrate (with prefabricated Au/Ni contact pads) was placed in the chamber along with a Faraday cup (FEI) in order to measure the exact beam current from the electron source. Nominal beam currents were set at 1.4 nA, while the actual mean current measured using the Faraday cup was 1.28 ± 0.09 nA. The instrument was then evacuated overnight giving a chamber pressure of about 6.0×10^{-7} mbar. Upon opening the gas injection system (GIS), the pressure in the chamber increased an order of magnitude higher than the base pressure, suggesting a sufficient quantity of precursor was injected into the system. After closing the GIS, the pressure returned to its original value within 10 min. Electron beam induced deposition (EBID) was applied by a tetrakis (trifluorophosphine) platinum ($Pt[PF_3]_4$) GIS (CAS number: 19529-53-4, vapour pressure 240 mm (55 ^oC), boiling point 80 ^oC, MW 547.01, supplied by STREM Chemicals Inc.) and a standard $(CH_3)_3Pt(C_PCH_3)$ GIS to selectively deposit Pt metal onto Au/Ni contact pads for 2- and 4-point electrical measurements. Interconnects with nominal dimensions of 30 μm × 200 nm and thicknesses of approximately 20 nm, were deposited.

2.3.1 Rapid Thermal Annealing

Annealing of the interconnects was achieved by rapid thermal annealing (RTA) at 400 ^{o}C for 1 min in N_2 and in forming gas (5% H_2 in N_2), respectively. The ramp time from room temperature to 400 ^{o}C was achieved in 2 min giving a rate of approximately 3.3 ^{o}C s^{-1}.

2.3.2 Electrical Characterisation

The electrical measurements were performed using a Cascade Microtech probe station with a B1500 (Agilent Technologies) semiconductor device analyser. Pt interconnects from both precursors were deposited across 4 Au/Ni contact pads. Initial measurements consisted of using a 4-point probe method to identify the contact resistance. This was performed by contacting two probes to the two outer pads and forcing a current between them. The voltage drop between the inner two electrodes was the measured. After a negligible contact resistance was obtained, 2-point measurements were carried out for the rest of the study. Figure 2.2 below highlights the difference between the two methods. In both cases, a voltage sweep between -1 V and +1 V was employed.

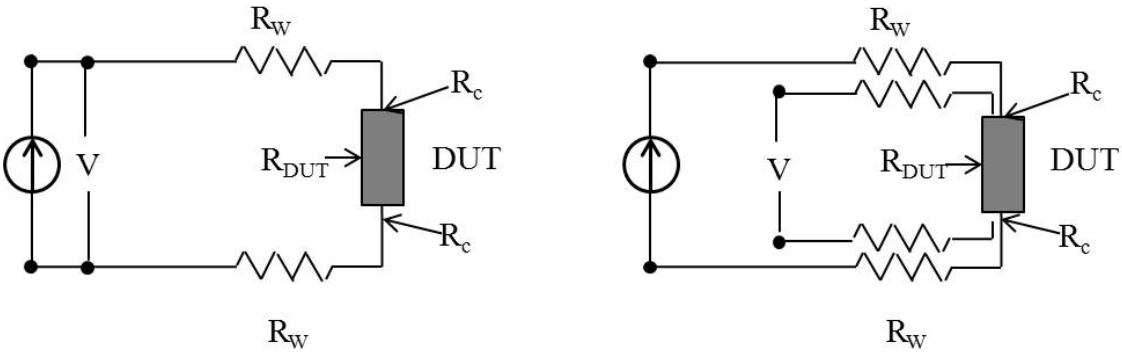


Figure 2.2 2-point (left) and 4-point (right) probe resistance measurements [3].

2.4 References

(1) Giannuzzi, L. A.; Stevie, F. A. *Micron* **1999,** 30, 197.

(2) Liu, S.; Chen, G.; Prasad, P. N.; Swihart, M. T. *Chem. Mater.* **2011,** 23, 4098.

(3) Schroder, D. K., *Semiconductor material and device characterization.* 3rd ed.; John Wiley & Sons: 2006.

Engineering the Growth of Germanium Nanowires by Tuning the Supersaturation of Au/Ge Binary Alloy Catalysts

3

[This chapter has been published as a peer-reviewed article in the journal Chemistry of Materials. Consequently, certain sections of the chapter such as the abstract and introduction may contain repeating paragraphs and concepts]

O'Regan, C.; Biswas, S.; O'Kelly, C.; Jung, S. J.; Boland, J. J.; Petkov, N.; Holmes, J. D. (2013). ***Chem. Mater****. 25:3096-3104*

3.1 Abstract

The synthesis of Ge nanowires with very high-aspect ratios (greater than 1000) and uniform crystal growth directions is highly desirable, not only for investigating the fundamental properties of nanoscale materials, but also for fabricating integrated functional nanodevices. In this chapter, we present a unique approach for manipulating the supersaturation, and thus the growth kinetics, of Ge nanowires using Au/Ge bilayer films. Ge nanowires were synthesised on substrates consisting of two parts: a Au film on one half of a Si substrate and a Au/Ge bilayer film on the other half of the substrate. Upon annealing the substrate, Au and Au/Ge binary alloy catalysts were formed on the Au-side and Au/Ge-side of the substrates respectively, under identical conditions. The lengths of Ge nanowires produced were found to be significantly higher on the Au/Ge bilayer side of the substrate compared to the Au-coated side, as a result of a reduced incubation time for nucleation on the bi-layer side. The mean length and growth rate on the bilayer side (with a 1 nm Ge film) was found to be 5.5 ± 2.3 μm and 3.7×10^{-3} μm s^{-1} respectively, and 2.7 ± 0.8 μm and 1.8×10^{-3} μm s^{-1} for the Au film. Additionally, the lengths and growth rates of the nanowires further increased as the thickness of the Ge layer in the Au/Ge bilayer was increased. In-situ TEM experiments were performed to probe the kinetics of Ge nanowire growth from the Au/Ge bilayer substrates. Diffraction contrast during in-situ heating of the bilayer films clarified the fact that thinner Ge films, *i.e.* lower Ge concentration, take longer to alloy with Au than thicker films. Phase separation was also more significant for thicker Ge films upon cooling. The use of binary alloy catalyst particles, instead of the more commonly used elementary metal catalyst, enabled the supersaturation of Ge during nanowire growth to be readily tailored, offering a unique approach to producing very long high aspect ratio nanowires.

3.2 Introduction

One-dimensional (1D) semiconductor nanowires have stimulated much interest in the last number of decades due to their potential use as building blocks for assembling nanoscale devices and architectures. [1-3] While Si has been the material of choice for many years for nanoscale electronic devices [1], there has recently been a renewed interest in Ge [4-7] for applications such as nano-electromechanical systems (NEMS) [8, 9], lithium-ion batteries [10-12], field effect transistors (FETs) [13] and photovoltaics [14]. Like Si, Ge is a Group 14 semiconductor material and exhibits certain properties that are superior to those of Si, including a higher charge carrier mobility [15] and a larger Bohr exciton radius, leading to more pronounced quantum confinement effects at higher dimensions. [16] Notably, the many parallels between Si and Ge should allow the seamless integration of Ge into current Si based devices.

The vapour-liquid-solid (VLS) method is the most recognized approach for synthesising Ge nanowires, allowing control over morphology and aspect ratio. The synthesis of high aspect ratio Ge nanowires with diameters between 10-20 nm and lengths in the micrometer and even millimeter regime, is of practical importance for the development of multiple device structures using individual nanowires. Long Ge nanowires, with high aspect ratios, can potentially be achieved by manipulating the rate determining step of VLS growth. Previous reports have highlighted that the incorporation of growth species (via the vapor phase) at the liquid-vapour interface [17-19] and the crystallisation of nanowires at the liquid-solid interface [20] can both act as potential rate determining steps in the VLS mechanism. Whilst both the incorporation and crystallization steps play a role in determining the overall rate of nanowire growth, the incorporation process can be neglected in our VLS

experiments as we assume the precursor pressure remains constant throughout the growth process; due to minimal temperature variations and carrying out reactions at atmospheric pressure. Therefore, assuming the crystallisation of the Ge nanowires to be rate limiting, the enhanced rate of nanowire growth can be achieved by increasing the supersaturation of Ge in a binary system, such as Au-Ge. Supersaturation acts as the driving force for layer-by-layer crystallisation at the triple phase boundary (TPB) during the nanowire growth process [21]. Han *et al.*[22] previously tuned the supersaturation of Au-Ga binary alloy particles in order to manipulate the growth of GaAs nanowires. They found that by increasing the Ga concentration in the seeds, by varying the thickness of the Au film deposited on SiO_2/Si substrates, they could increase the growth rate of the resulting nanowires and maintain unidirectional growth. Standard Au films have already been used to promote the growth of Ge nanowires by several groups [23, 24]. Whilst Ge buffer films have been used to grow taper-free and highly crystalline Ge nanowires via a two-temperature process [25, 26] and have also been used to catalyze the growth of Au and Si_3Cu nanowires [27, 28], they have not been employed to manipulate the growth kinetics of Ge nanowire growth via a VLS process. Here, we report the successful manipulation of the supersaturation in the liquid seeded bottom-up growth of Ge nanowires by tailoring the eutectic composition in Au-Ge bilayer films to influence the induction time for nanowire growth; providing a facile method for growing high aspect ratio Ge nanowires for future nanoscale devices.

.

3.3 Results and Discussion

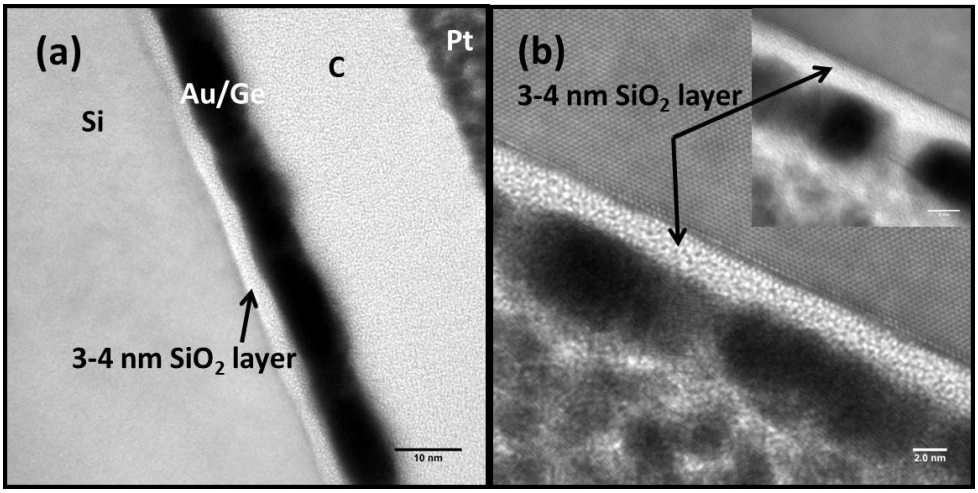


Figure 3.1 Phase-contrast TEM micrographs of a Au/Ge (5 nm/1nm) bi-layer cross-section. While the Ge is layer is hard to distinguish due to its thickness, EDX analysis was used to confirm its presence. (a) Au/Ge bi-layer film before annealing. A 3-4 nm SiO_2 layer is clearly visible beneath the Au. (b) Au/Ge bilayer film after annealing at 430 ^oC for 30 mins. Note that the 3-4 nm SiO_2 layer is still intact, which prevents intermixing of Si and Au.

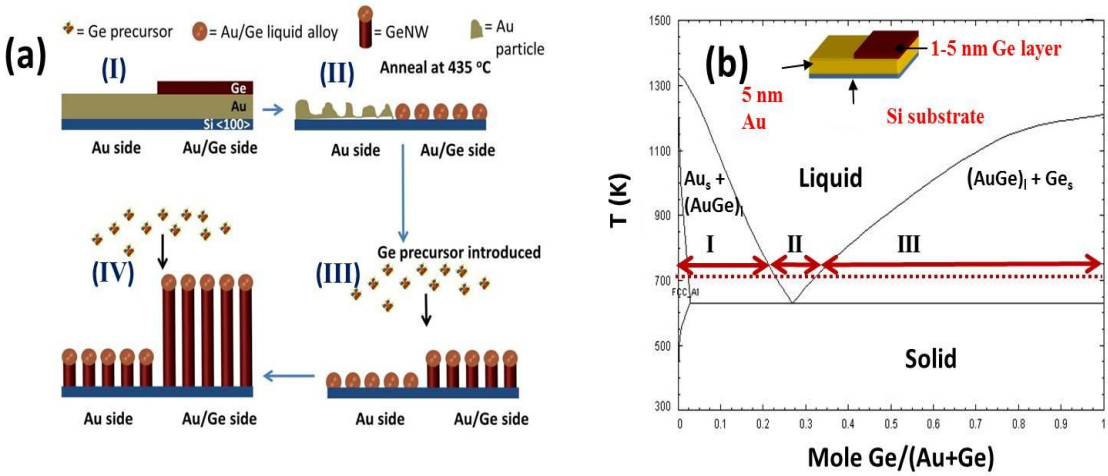


Figure 3.2 (a) Schematic illustrating the difference between Ge nanowire growth on the Au and Au/Ge bilayer side of a Si substrate. Nanowires grown on the bilayer side nucleate faster and thus have greater lengths than those on the Au side, for a given growth time. (b) Phase diagram of the Au/Ge alloy system tracing and comparing the evolution of Ge nanowires grown on the Au side and Au/Ge bilayer side of the substrate. Inset shows the 2-part substrate used which consists of a Au film on one side and a Au/Ge bilayer on the other side.

A cross-sectional TEM image of a pre-annealed Au/Ge (5 nm/1 nm) bilayer film deposited on a Si(100) substrate is shown in figure 3.1. The presence of a 3-4 nm SiO_2 layer beneath the Au film prevents direct interaction of Au with the underlying Si substrate and the formation of a Au/Si alloy upon annealing, as previously reported by Ferallis *et al.* [29]. Significantly, this SiO_2 layer remains intact after annealing at 430 ^oC for 30 min, as shown in figure 3.1 (b) confirming the absence of intermixing between the Au films and the Si substrate. Figure 3.2 (a) presents a schematic of the nanowire growth process using a 2-part Si substrate consisting of a Au (5 nm) and Au/Ge (5 nm/*x* nm) bilayer film, with varying Ge thickness (*x* = 1, 2, 5 nm) (shown in the inset in figure 3.2 (b))

3.3.1 The Use of Bi-layer films to Influence Ge Nanowire Growth

The bulk phase diagram for the Au/Ge binary system (figure 3.2 (b)) [30] traces the progression of an Au/Ge binary alloy system from a solid Au film to Ge nanowire growth, as the concentration of the Ge component in the two-phase system increases. The phase diagram, in conjunction with the schematic shown in figure 3.2 (a), can be used to explain the participation of the Ge film to yield high aspect ratio nanowires. Typically, VLS growth requires the presence of both a semiconductor material and a metal catalyst to form a binary alloy before nanowire growth can proceed. A typical VLS process involves a Au catalyst heated above the eutectic point of the metal-semiconductor binary system, for example, 360 ^oC with a 28 % uptake of Ge in Au [30]. Without any Ge uptake, the system remains at the beginning of regime I on the red line of the phase diagram, as shown in figure 3.2 (b), *i.e.* to the far left of the Au rich region (with 0 % Ge content). As the system is heated to the synthesis temperature, Au on the bilayer part of the Si substrate is exposed to Ge, forming a

eutectic liquid melt catalyst with a certain uptake of Ge (regime II, figure 3.2 (b) and part II, figure 3.2 (a)) whilst the pure Au part of the substrate remains unexposed to Ge. With an increased supply of Ge from the precursor, the alloy particle on the bi-layer side becomes supersaturated causing solid Ge to crystallise out of the droplet forming a nanowire (regime III, figure 3.2 (b)). The incubation time associated with Ge nucleation is directly related to the Ge supersaturation ($\Delta\mu$), *i.e.* the difference in the chemical potential between Ge in the Au/Ge alloy and Ge in the crystalline nanowire. Hence, a reduced incubation time for nanowire nucleation can be achieved by increasing the solute concentration in a two phase liquid alloy and thus the supersaturation of the Ge in the binary catalyst system [31].

Exposure of the Au/Au-Ge substrate to the Ge precursor (DPG), results in a higher Ge supersaturation in the Au/Ge bilayer film (regime III, figure 3.2 (b)), and faster nucleation of Ge nanowires, as seen in part III of figure 3.2 (a). The Au side of the substrate however only reaches regime II in the phase diagram with the introduction of DPG into the reaction chamber. Sustained flow of the Ge precursor through the system results in further growth of the nanowires on the Au/Ge substrate side, as the system is already in the Ge-rich part of the phase diagram (part IV of the schematic in figure 3.2 (a)). At the same time interval, the Au side reaches regime III of the phase diagram in figure 3.2(b) and nucleation of solid Ge occurs. Consequently, Ge nanowires grow first on the Au/Ge bilayer side due to a lower induction time, resulting from faster supersaturation and nucleation of the catalytic seeds. Hence, the bilayer system produces longer wires when compared with standard Au seed mediated growth methods over a typical growth period of 25 min (figures 3.3 (a) and (b)). Millisecond timescales for a single nucleation event have previously been

predicted through a time resolved simulation study of a VLS-nanowire growth process [32]. However, monitoring the time scales of single nucleation event in a 2D layer-by-layer growth process on both the Au and Au/Ge bilayer sides of a substrate was beyond our experimental capability. Hence, a 25 min time interval was chosen to compare multiple nucleation events in both the Au and Au/Ge bi-layer films, which collectively contribute to the nanowire growth process [31,33].

3.3.2 SEM and TEM Characterisation

Figures 3.3 (a) and (b) show top-down SEM images of Ge nanowires grown from a Au film and a Au/Ge bilayer film (5 nm/2 nm) respectively, using the LICVD methodology at 430 ^{o}C with a 25 min growth time. SEM analysis supports the argument outlined above for a faster supersaturation and hence a higher growth rate of nanowires with the Au/Ge film (where the Ge film is 2 nm), by revealing significantly longer wires on the Au/Ge side (7.7 ± 3.0 μm) of the substrate when compared to the Au side (2.7 ± 0.8 μm) for a typical growth time of 25 min (figure 3.3 (e)), corresponding to growth rates of 4.9×10^{-3} and 1.8×10^{-3} μm s^{-1} for growth on the Au/Ge and Au side respectively. The calculated nanowire growth rates include a contribution from the incubation time in the nucleation mediated process.

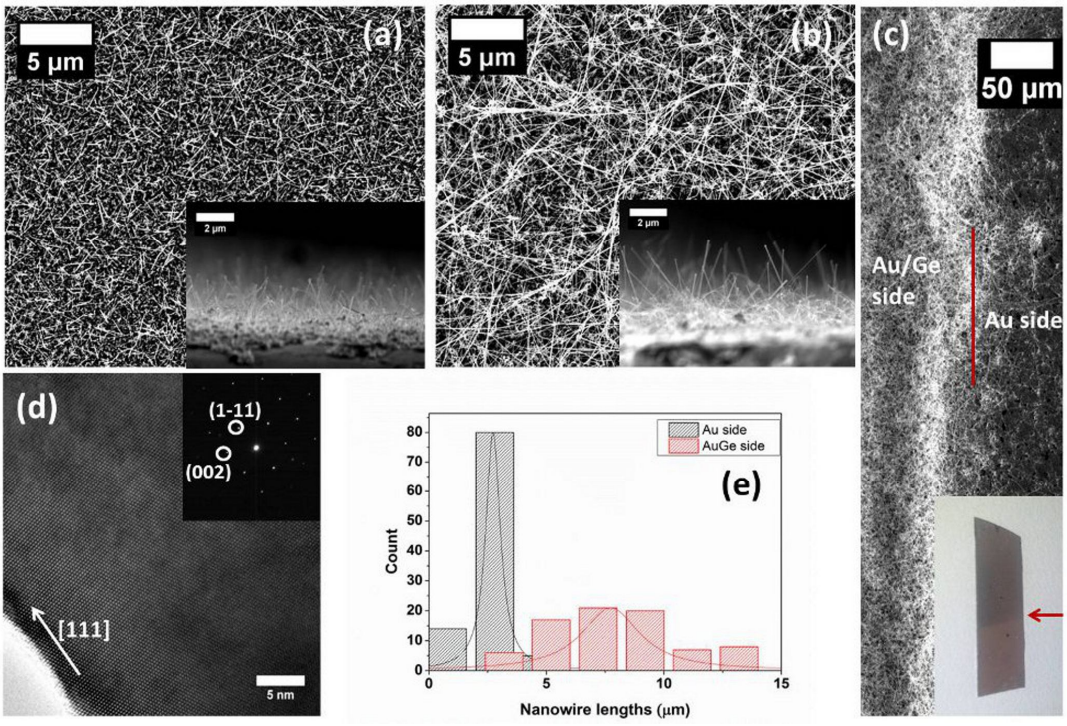


Figure 3.3 SEM and TEM images of Ge nanowires grown from a two-sided substrate. (a)-(b) Top-down SEM images showing Ge nanowires grown from the Au side and Au/Ge (5nm / 2 nm) side respectively; growth time was 25 min. Insets show cross-sectional SEM images of Ge nanowires on the Au side and Au/Ge side respectively. (c) Top-down SEM image showing the interface between the Au and Au/Ge side. Inset is a photograph taken of the substrate after removal from the CVD apparatus. The sharp interface implying different growth scenarios with the Au and Au/Ge film. (d) Lattice resolution TEM image of a Ge nanowires grown on the Au/Ge bilayer side. Inset is the SAED pattern viewed along the [110] zone axis which confirms the <111> growth direction. (e) Histogram confirming the significant difference in nanowire lengths between the Au and Au/Ge side. Lorentzian curves are fitted to both plots to guide the eye, which show a much broader size distribution of the GeNWs grown on the bi-layer side

The significantly longer nanowire lengths can also be seen in the insets of both figures 3.3 (a) and (b), which show SEM images of nanowires tilted 90 degrees to the beam, grown on the Au and Au/Ge bilayer side of the Si substrate respectively. SEM characterisation confirmed a high abundance of nanowires on the substrate. A sharp interface can be seen between the Au and Au/Ge sides of a substrate shown in figure 3.3 (c), highlighting the presence of different growth regimes on the two sides

and that as the interface is crossed, the growth regime rapidly changes. The inset in figure 3.3 (c) shows a photograph of the substrate after removal from the reaction cell. The interface (marked by the red arrow) between the different growth regimes on the Au and Au/Ge sections of the substrate can clearly be seen in the photograph. Figure 3.3 (d) shows a high resolution TEM micrograph of a Ge nanowire grown on the Au/Ge bilayer side of a Si substrate, highlighting the crystallinity of the nanowire. The inset in figure 3.3 (d) is an SAED pattern imaged along the [110] zone axis of the nanowire, confirming its cubic crystal structure (PDF 04-0545) and [111] growth direction. Nanowires grown from the Au/Ge and Au-only layers were found to have predominantly a [110] or [111] growth directions, with the [110] direction prevalent for nanowires with diameters below approximately 25-30 nm, as previously reported by Schmidt *et al.*[34] for Si nanowires. These growth orientations do not agree with the recently published data of Dayeh *et al.* who reported [111] growth directions for nanowires below 25 nm[17]. Only a minority of our Ge nanowires below 25 nm had a [111] orientation.

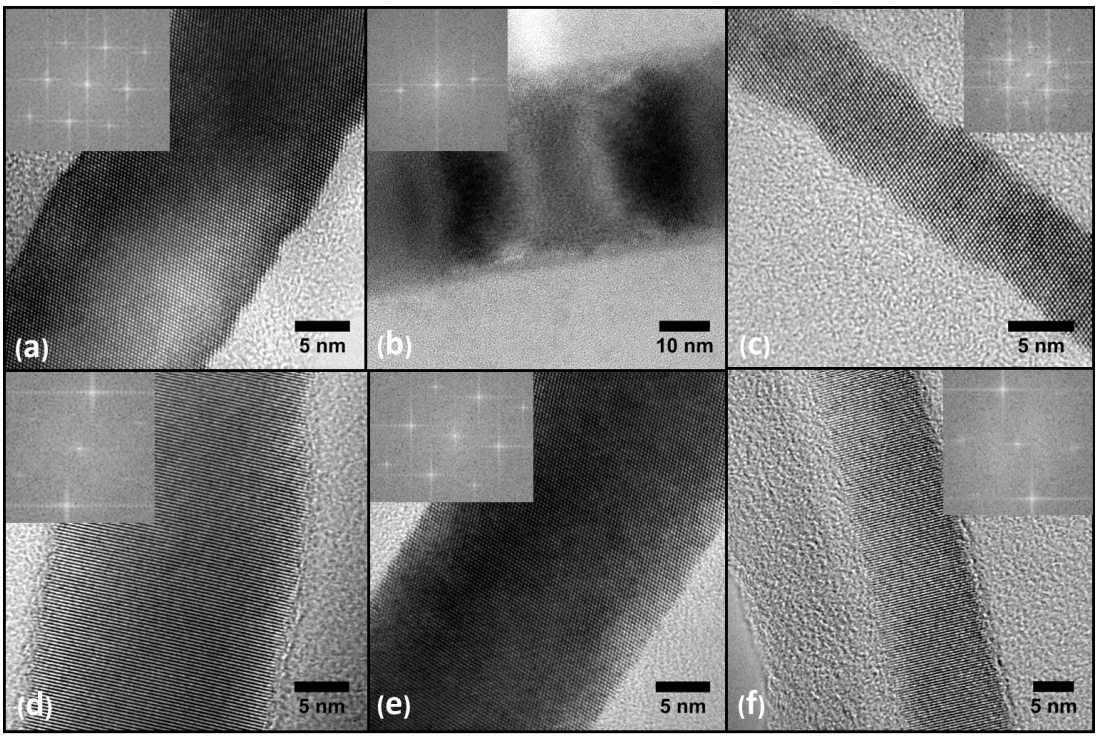


Figure 3.4 TEM micrographs of nanowires grown from the Au/Ge bi-layer side ((a), (b) and (c)) and nanowires grown from the Au film side ((d), (e) and (f)). Insets are fast fourier transforms (FFTs) taken from the lattice resolved image and confirm the common growth orientation of (111).

Figure 3.4 presents additional high resolution TEM images of Ge nanowires grown from the two-part substrate in order to highlight the uniform morphology of the nanowires. Recently, Han *et al.* [22] demonstrated that tuning the catalytic composition of binary alloys affected the crystallographic growth direction of the GaAs nanowires produced. Hence, the diameters and growth directions of over 60 nanowires were compiled for both the Au and Au/Ge growth regimes. Distributions of Ge nanowire growth directions from the Au and Au/Ge sides of Si substrates are presented in figure 3.5 and reveal predominantly [110] and [111] orientations on both sides. On the Au side, approximately 69 % of the nanowires adopted a [111] orientation while 24 % have a [110] direction. A minority of the nanowires examined adopt a [211] orientation (6 %). A larger percentage of the Ge nanowires

examined on the Au/Ge side had a [111] orientation, with 83 % of them adopting this growth direction, while only 15 % adopted the [110] orientation. Again, a minority of wires had a [211] growth direction (~ 2 %). Hence, the addition of a Ge buffer layer did not notably influence the overall nanowire growth direction. Au/Ge bilayer films can therefore be utilised to generate high-quality Ge nanowires without sacrificing orientation uniformity. Additionally, the diameter of the Ge nanowires grown from the Au/Ge side were similar to those synthesised on the Au side, with mean diameters of 49.1 ± 14.6 nm and 42.1 ± 11.2 nm for the Au side and Au/Ge bilayer side respectively. Whilst an in-depth investigation into the nanowire orientation dependence on length was not undertaken in this study, figure 3.5 infers that the majority of the long nanowires adopt a [111] orientation, assuming a supersaturation limited growth process and the Gibbs-Thomson effect.

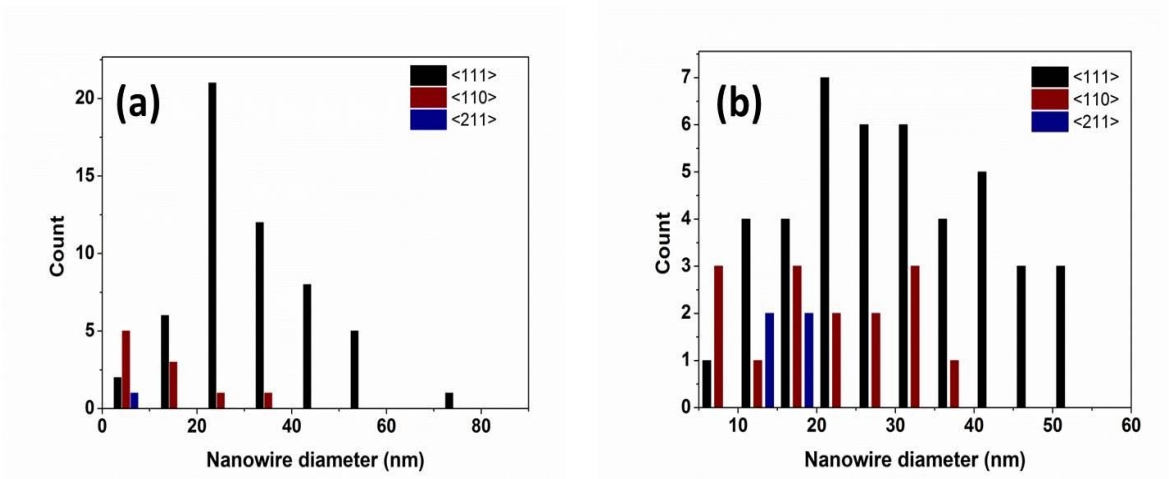


Figure 3.5 Diameter-dependent growth orientation distributions. (a) Distribution of nanowire diameters obtained by TEM on the Au/Ge bi-layer side. Diameters for (111), (110) and (211) are given. (b) Distribution of nanowire diameters obtained by TEM on the Au film side. Diameters for (111), (110) and (211) are given. No significant difference in diameters or growth orientations was observed between the Au film and the Au/Ge bi-layer.

3.3.3 Kinetic Studies of Ge Nanowires

Figure 3.6 (a) shows a histogram of the length distributions of Ge nanowires grown from Au/Ge bilayer films with increasing Ge film thickness. In all cases, a 2-part substrate as described in figure 3.2 was used, allowing a direct comparison between nanowire growth on the Au and Au/Ge sides of the substrate under identical reaction conditions. The histogram shows the lengths of Ge nanowires grown from a standard Au film (5 nm) and from Au/Ge bilayer films with Ge thicknesses of 1, 2 and 5 nm. Each plot consists of a Lorentzian fit in addition to the raw data, which was obtained by direct measurement of nanowire lengths using TEM. As is evident from the graph, as the thickness of the Ge layer increased, so did the mean length of the nanowires, accompanied by a broadening of the length distribution. The mean lengths in each case were found to 2.7 ± 0.8 μm, 5.5 ± 2.3 μm, 7.7 ± 3.0 μm and 9.02 ± 3.5 μm for the pure Au film and Au/Ge bilayer films with a Ge thickness of 1, 2 and 5 nm respectively. A distinct broadening in the length distribution of the nanowires with increasing Ge thickness is apparent from the Lorentzian fits shown in figure 3.6 (a). The FWHM increased from 0.8 to 3.5 μm for Ge nanowires grown from a Au-only film to a 5 nm Au/5 nm Ge bilayer film and can be explained by the difference in the supersaturation and nucleation kinetics for the eutectic binary alloy seeds compared to Au.

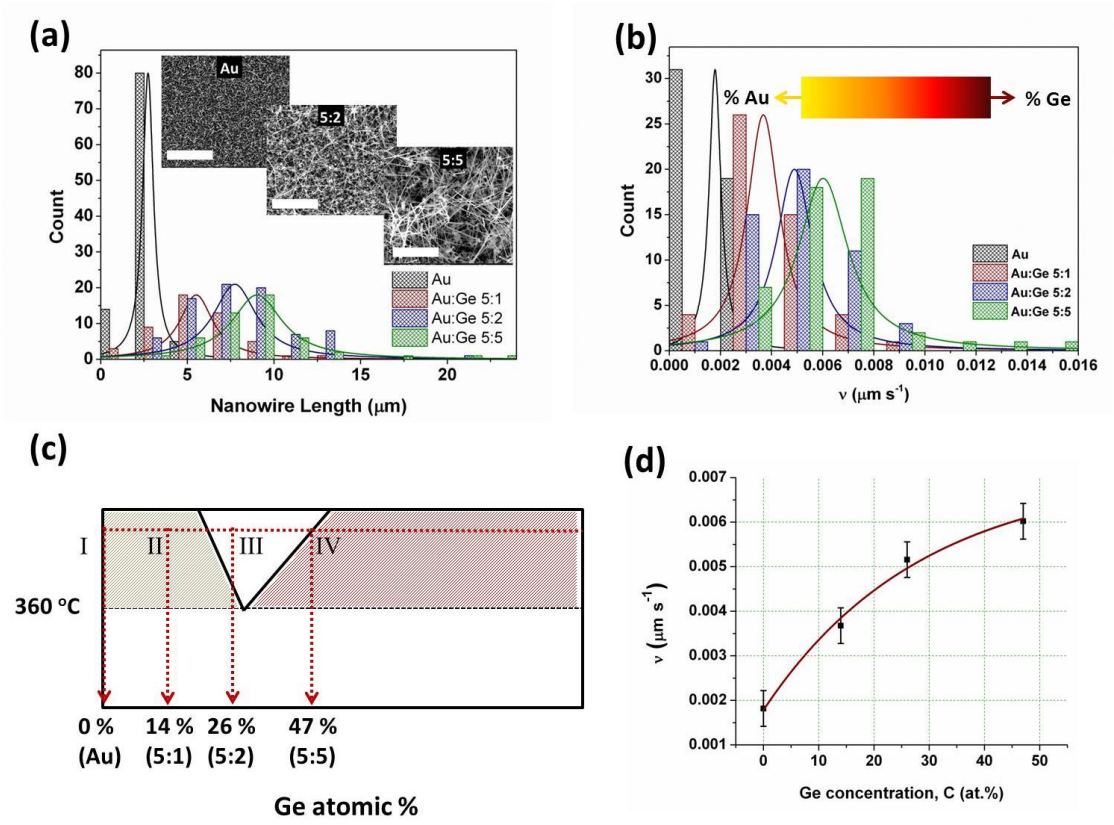


Figure 3.6 (a) Histogram showing the relative length distributions of Ge nanowires grown from a Au film and Au/Ge bilayers with varying Ge thicknesses. Growth time in all cases in 25 mins. Insets show SEM images of Ge nanowires grown from a Au film as well as Au/Ge bilayers, with Ge layer thickness of 2 and 5 nm. Scale bar is 5 μm (b) Histogram showing the relative growth rate distributions of Ge nanowires grown from a Au film and Au/Ge bilayers with varying Ge thicknesses. Lorentzian curves are fitted to all plots in (a) and (b), and show a broadening of the size distribution in the length and growth rate of GeNWs as the thickness of the Ge film increases. (c) Enhancement of the low-temperature regime of the Au/Ge phase diagram shown in figure 1(b) which traces the behavior of the binary alloy formed from bilayers with increasing Ge solute concentration, *i.e.* increasing Ge film thickness. (d) Mean nanowire growth rate as a function of the Ge solute concentration in the binary alloy.

A Au/Ge bilayer creates a binary alloy upon annealing, prior to any precursor injection. However, the binary alloy particles do not contain an equal Ge concentration, as the distribution of the Ge layer within the Au is not uniform. The percentage of Ge is not the same in each binary alloy particle catalyst, resulting in different levels of supersaturation. Consequently, when the Ge precursor is injected,

nucleation of Ge at the TPB will not occur simultaneously for all binary alloy particles, resulting in a broad distribution of lengths. This broadening increases with thicker Ge films, yielding Au/Ge binary alloy particles with a higher and more varied Ge content. With the pure Au film, there is no formation of binary alloy particles after annealing. The Au islands which form upon nucleation are exposed to the Ge precursor in roughly equal proportions, resulting in near equal supersaturation and simultaneous nucleation of Ge nanowires, yielding a narrower length distribution. SEM micrographs (shown in the inset in figure 3.6 (a)) of Ge nanowires grown from a Au layer, a Au (5 nm)/Ge (2 nm) bilayer and a Au (5 nm)/Ge (5 nm) bilayer show longer nanowires with increasing Ge film thickness, *i.e.* increasing Ge content in the eutectic catalyst. As mentioned previously, the formation of a Au/Si alloy as a result of the intermixing between the Au and Si substrate upon annealing is unlikely due to the presence of a 3-4 nm SiO_2 layer. To further alleviate concerns about intermixing, we carried out growth experiments on Si/SiO_2 wafers (200 nm SiO_2 layer). Figure 3.7 (a) shows a TEM micrograph of a cross-section of one of these substrates with a deposited Au/Ge bi-layer. The 200 nm SiO_2 layer is clearly visible. Figure 3.7 (b) reveals a nanowire length distribution very similar to that shown in figure 3.6 (a) for a 2 nm Ge film, suggesting that Au/Si intermixing was not an issue in our experiments.

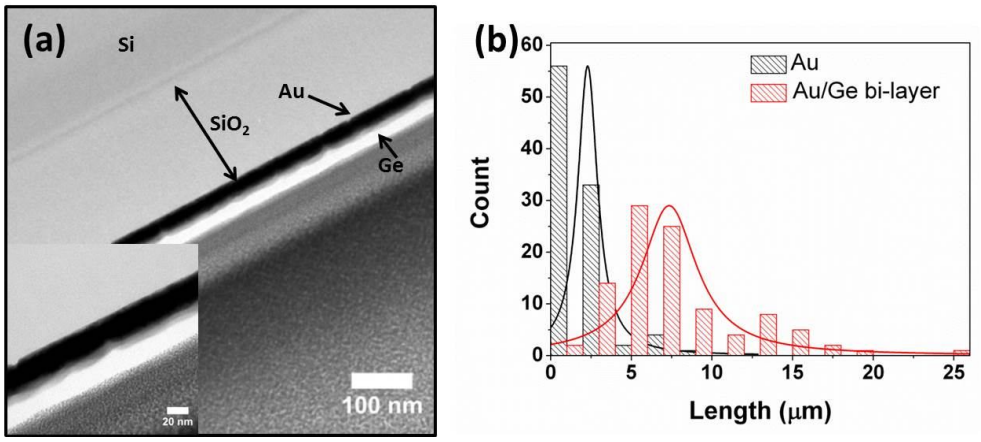


Figure 3.7 (a) TEM micrograph showing a cross-section the Si/SiO_2 substrate that was used to grow GeNWs, as a compliment to the growth already carried out using Si wafers. The 200 nm SiO_2 layer is clearly visible. Inset is higher magnification of the same cross-section, highlighting the Au/Ge bi-layer. (b) Length distribution of GeNWs grown on the Au and Au/Ge bi-layer deposited on the Si/SiO_2 substrate. The distribution clearly shows longer nanowires on the bi-layer side

Figure 3.6 (b) shows a second histogram of nanowire growth rates from the same bilayers as shown in figure 3.6 (a). As expected, the overall nanowire growth rate increases with the thickness of the Ge layer, due to the raised Ge concentration in the binary alloy particle catalysts, inferring a faster nucleation of Ge at the TPB. The overall nanowire growth rate can be separated into constituent parts: (i) the rate of incubation, *i.e.* the time required for the initial nucleation to take place upon precursor injection and (ii) the rate after incubation. The incubation time consists of a dead time (T_1), *i.e.* the time for the precursor to travel from the source chamber to reaction chamber and the time for a nucleation event to occur (T_2). As a millisecond timescale is expected for a single nucleation event, shortening of the dead time in the Au/Ge bi-layer contributes towards a faster overall incubation rate ($T_1 + T_2$). During this dead time, the Au side remains inert in terms of germination and nucleation. However, on the Au/Ge side, the nucleation process can initiate due to the presence

of the Ge film, effectively minimising the dead time. In other words, single nucleation events take longer on the Au side because of the added dead time.

The faster nucleation of Ge with increasing Ge film thickness is explained with a magnified representation of the eutectic region of the bulk phase diagram (figure 3.6 (c)). Annealing of the Au and Au/Ge films prior to nanowire growth is the key to obtaining favourable growth kinetics with a Ge buffer layer. The annealing process creates binary alloy catalysts which participate in nanowire growth, thus yielding a higher Ge concentration when compared to standard Au seeds. Increasing the Ge concentration corresponds to progression along the horizontal dashed red line in figure 3.6 (c), representing nanowire growth at a temperature of 430 ^{o}C. Position I on the partial bulk Au/Ge phase diagram (figure 3.6 (c)) represents 0 % Ge in Au and is analogous to using a pure Au film. Assuming the absence of a Ge precursor, the Au film does not form a Au/Ge alloy upon annealing at our growth temperature prior to nanowire growth. Introducing a Ge film moves the Au/Ge system along the dashed red line to regime II which, assuming complete intermixing, is analogous to a 5 nm Au/1 nm Ge bilayer film, or approximately 14 at.% Ge in the Au/Ge binary alloy. Here, the system will form a Au/Ge liquid mixture with solid Au upon heating, but the entire film will not form a liquid alloy and the solid Au will require an incubation time for alloying and supersaturation to occur. A further increase in the Ge concentration in the Au/Ge system to a composition of 26 at.% (regime III) places the system within the liquid region of the phase diagram and forms a Au/Ge binary eutectic alloy. This is analogous to the participation of a 5 nm Au/2 nm Ge bilayer film. Finally, increasing the thickness of the Ge film in the Au/Ge bilayer to 5 nm (47 at.% Ge in the Au/Ge alloy) moves the Au/Ge binary system further along

the dashed red line to point IV, into the Ge-rich region of the phase diagram, resulting in extremely fast nucleation. Although the bulk binary phase diagram has been used to explain the nanowire growth scenario, a shift in the liquidus and solidus curve in the bulk phase diagram should be taken into account due to nanoscale size effects[17, 35-37]. Finally, figure 3.8 summarises the dependence of nanowire length and growth rate on Ge buffer layer thickness.

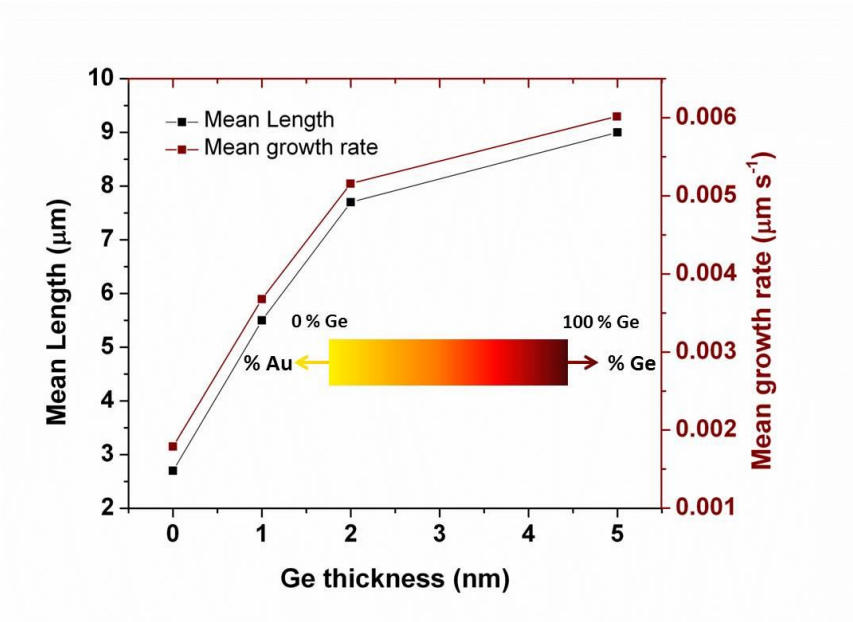


Figure 3.8 Summary of length and growth rate behaviour of nanowires grown from bi-layers of increasing Ge thickness.

The nanowire growth after incubation, *i.e.* independent of T_1 and T_2, is also influenced by the introduction of a Ge layer to the Au-coated substrate, as evidenced from the nanowire length distribution plots shown in figure 3.9 for Ge nanowire growth from Au and Au/Ge substrates for different reaction times. A more pronounced increase in the mean length of the nanowires in the Au/Ge side for different reaction periods indicates a change in the growth rate during and after nanowire incubation.

Supersaturation acts as a thermodynamic driving force which transfers Ge atoms from a seed particle to a nanowire. Givargizov presented a quadratic relationship between the growth rate of Si nanowires and the supersaturation according to equation 1 [20]:

$$v = b\left(\frac{\Delta\mu}{kT}\right)^2 \quad (1)$$

where v is the nanowire growth rate, b is the kinetic coefficient of crystallisation, $\Delta\mu$ is the supersaturation, k is the Boltzmann constant and T is the temperature. According to equation 1, the growth rate can be enhanced by increasing the supersaturation. Moreover, the supersaturation increases with Ge concentration according to equation 2 [17]:

$$\Delta\mu = kT\ln\left(\frac{C}{C_{eq}}\right) \quad (2)$$

where C is the solute concentration in the liquid binary alloy and C_{eq} is the equilibrium solute concentration determined from the bulk phase diagram. Thermodynamically, increasing the Ge concentration in the seed is associated with increasing the chemical potential of the growth species in solution, thus increasing the driving force responsible for nanowire growth. In this study, the Ge solute concentration (C) has been increased by adding a Ge layer onto a Au film and annealing the substrate to form a binary Au/Ge alloy prior to the introduction of the Ge precursor. Increasing the thickness of the Ge layer further increases C (assuming

rapid intermixing) and hence raises the supersaturation to a greater extent. The exponential dependence of the nanowire growth rate on the Ge concentration in the binary alloy catalyst (figure 3.6 (d)) can be inferred from equations (1) and (2), which further confirms the dependence of nanowire growth rate on the supersaturation. Considering 2D ledge nucleation at the TPB for Ge nanowire growth, the kinetic barrier for nucleation, as derived from classical nucleation theory, is given in equation 3 [31]:

$$\Delta G_B = \alpha^2 / 4\Delta\mu \tag{3}$$

where α is a geometrically weighted coefficient for forming a new surface and ΔG_B is the kinetic barrier for Ge ledge nucleation at the TPB. The size of ΔG_B determines the rate of Ge nucleation at the TPB and thus the overall growth rate of the Ge nanowires. ΔG_B can be related to the rate of nucleation according to equation 4 below:

$$P(t) = K \exp\left(-\frac{\Delta G_B}{k_b T}\right) \tag{4}$$

where K can be represented by $ZC\omega$, in which Z is the Zeldovich factor, C is the monomer concentration and ω is the molecular attachment frequency [31]. As the supersaturation increases, the rate of nucleation increases according to $exp\left(-\frac{b}{\Delta\mu}\right)$. An increased rate of nucleation also means a lower induction time.

Nucleation of Ge from a binary seed occurs within two different growth regimes over two time-scales [38]. The first of these is τ_{Ge} which represents the time for Ge nucleation to occur at the triple phase boundary (TPB) and the second is $\tau_{Au,}$ representing the time needed to add enough Ge to dissolve all the Au and melt the particle. In a standard VLS method with a Au film, usually $\tau_{Au} << \tau_{Ge}$ which tells us that the Au seed melts to form a AuGe alloy much faster than the nucleation of Ge to form a nanowire. This is logical as moving from left to right across the phase diagram (figure 1(b)), the Au/Ge binary system reaches the liquid alloy region before progressing on towards the nucleation region on the Ge rich side. However, upon increasing the Ge concentration in the binary alloy particles, by using an Au/Ge bilayer film instead of a Au film, the time for the particle melting (τ_{Au}) can be further reduced by shortening the time required for overall nucleation. Specifically, if the time required for the system to progress across the alloying (liquid) region of the phase diagram is shortened, then it can reach the nucleation stage quicker. This argument can be supported mathematically, leading to a direct dependence of the Ge solute concentration on induction time, as $\tau_{Ge} \propto (\ aC)$, where τ_{Ge} is the induction time for nucleation (reciprocal of the nucleation rate *P(t)*), *C* is the Ge solute concentration and *a* is a constant for a set of certain experimental parameters. The normal growth rate accounts for multiple nucleation events and lateral crystal growth over the duration of growth. The enhanced supersaturation on the Au/Ge bi-layer part increases the nucleation rate for each step and hence when all these nucleation events are added together, we get an overall faster nanowire growth rate on the Au/Ge side. Length distribution curves for the growth at different time scales (15 min, 25 min and 40 min) are presented in figure 3.9 and show different growth rates (actual growth rate excluding the incubation time) for Au and Au/Ge sides of the

substrate. Enhanced solute (Ge) concentration in the liquid alloys of the Au/Ge side when compared with the Au part at a certain time for each nucleating cycle during nanowire growth contributes towards higher supersaturation and nanowire growth rate. The nucleating cycle competes with the liquid alloy drop rejecting the excess Ge to reach an equilibrium state.

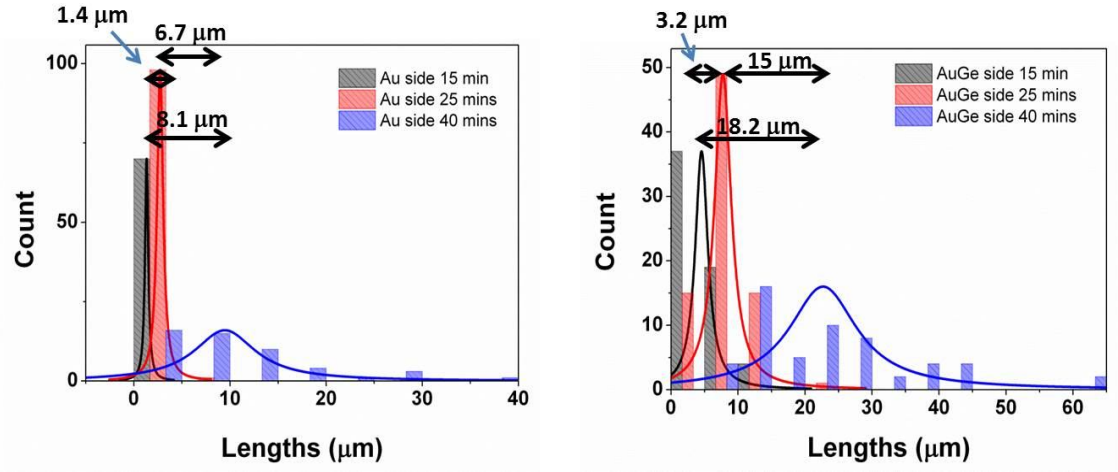


Figure 3.9 Length distributions of GeNWs at different growth times of 15, 25 and 40 mins. The length is shown to increase with growth time. (a) Length distribution for the Au side. (b) Length distribution for the Au/Ge side. The difference between mean lengths for different growth times is larger for the Au/Ge side, suggesting a higher growth rate.

3.3.4 In-situ TEM Studies of Bi-layer Films

The Ge nucleation kinetics for bilayer films of varying Ge layer thickness was further investigated using *in-situ* annealing experiments inside a TEM. Au and Au/Ge bilayer films were deposited on SiO_2 support films with thicknesses identical to those used to synthesise Ge nanowires. As in-situ TEM allows the examination of nanoscale systems as they undergo physical transformation (upon heating, for example), insights into the liquid-solid interface behaviour, phase nucleation and the mechanisms controlling nucleation and growth [39-41] can be obtained. Figure 3.10 shows a series of dark-field TEM images taken during in-situ heating of the Au-only and Au/Ge bilayer films. Dark-field imaging was used to eliminate contrast due to mass/thickness allowing comparison between alloying of the bilayer films.

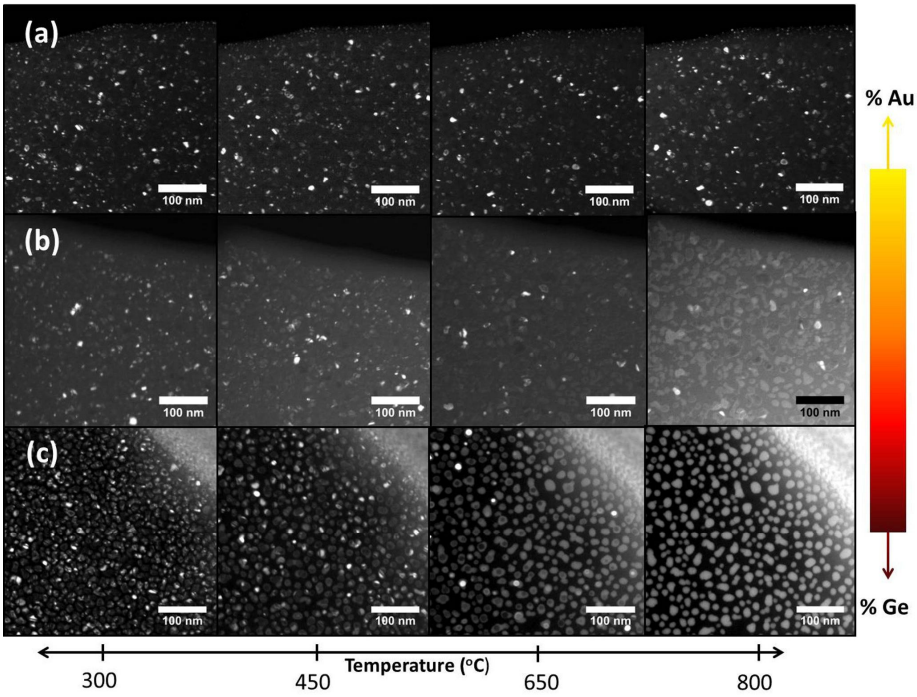


Figure 3.10 Three series of plan view dark field images showing the annealing of Au/Ge bilayer films deposited on SiO_2 membrane grids by in-situ TEM. Images show films at 300, 400, 650 and 800 ^{o}C. Heating of (a) a 5 nm Au film, (b) a 5 nm Au/1 nm Ge bilayer and (c) a 5 nm Au/5 nm Ge bilayer.

Figure 3.10 (a) represents a series of images taken during the in-situ heating of a 5 nm Au film. The bright spots represent the diffraction contrast from solid crystalline Au with specific orientations that meet the Bragg condition. A significant contrast can be observed across the entire temperature range, as the Au does not form an alloy and remains crystalline even at high temperatures. Conversely, figures 3.10 (b) and (c) show a reduction in diffraction contrast as the temperature increases for the 5 nm Au/1 nm Ge and 5 nm Au/5 nm Ge bilayers films respectively. This change in diffraction is particularly significant in figure 4(c) where the contrast completely disappears at high temperatures leaving uniform grey particles, inferring the complete formation of a liquid alloy; each sample was heated for 45 min in total with each temperature investigated maintained for 5 min. This in-situ data clarifies the fact that thinner Ge films, *i.e.* lower Ge concentration, take longer to alloy with Au than thicker films. Hence, longer nanowires are seen for thicker Ge films.

Higher magnification images were taken of the particles at high temperatures and at room temperature to compare the morphology of the particles before and after annealing of the films for different Ge film thicknesses. Moreover, the solidification of the particles and phase separation of the semiconductor material from the metallic material were compared. These studies offer an insight into the nucleation kinetics of Ge for varying Ge film thicknesses.

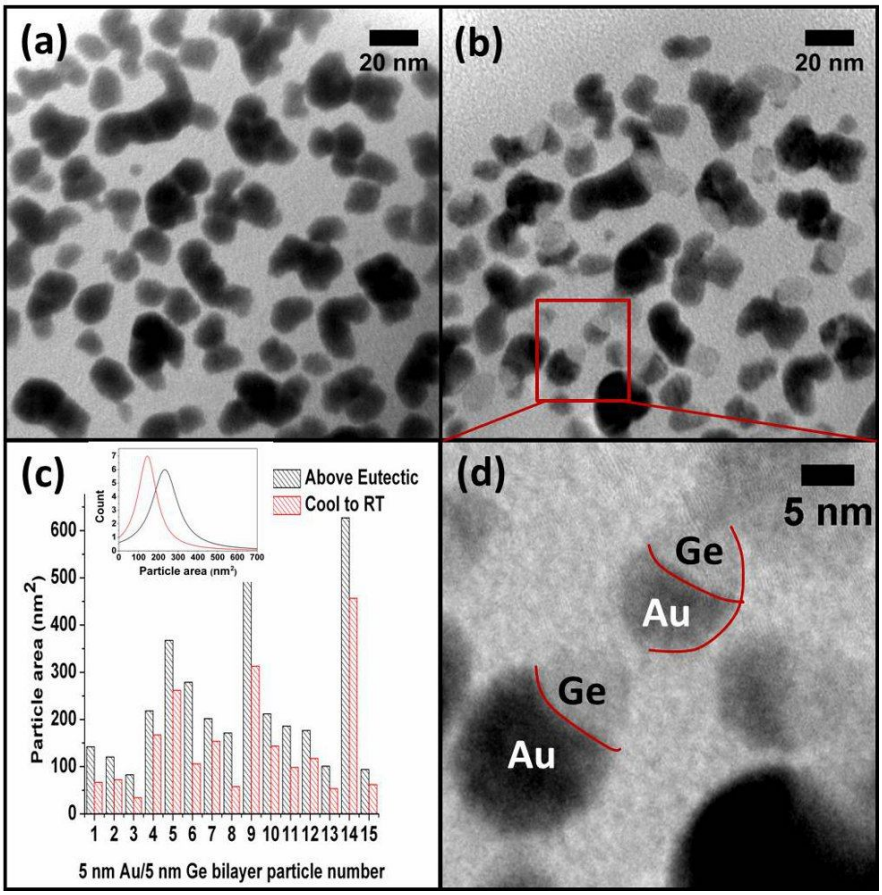


Figure 3.11 TEM analysis of Au/Ge alloy particles during in-situ temperature studies of the 5 nm Au/5nm Ge bilayer film. (a) TEM image of Au/Ge alloy particles above the eutectic temperature. (b) TEM micrograph of the Au/Ge particles shown in part (a) after cooling down to room temperature. (c) Bar chart showing the size differences between 15 particles measures above the eutectic temperature and after cooling to room temperature. Inset shows the Lorentzian curves of histograms plotted from the sizes of the same 15 particles at high temperature and after cooling to room temperature. (d) TEM image of the area inside the red box in (b), highlighting the separation of Ge from Au after cooling to room temperature. Red lines outline the interface between the Au and Ge.

Figure 3.11 (a) shows a TEM image of a 5 nm Au/5nm Ge bilayer film above the eutectic temperature during in-situ heating. Alloy particles in their liquid state are formed at this temperature as confirmed by the uniform contrast of the islands. After the sample was cooled down to room temperature, precipitation of Ge occurred as the particles solidify, as shown in figure 3.11 (b). In comparison to figure 3.11 (a), the Au and Ge segments are more easily identified, which is indicative of

solidification and segregation of the semiconductor phase from the metallic phase. As a consequence of this solidification, there is a shrinking of particle volumes, which is confirmed by the bar chart shown in figure 3.11 (c). This bar chart represents the projected areas taken of the dark Au portion of each particle; the Ge portion is excluded as Ge has been expelled from the Au due to phase separation. The areas of 15 particles were taken before and after cooling to room temperature during in-situ TEM studies and plotted. As is evident from figure 3.11 (c), the mean particle size decreased upon cooling, a result which can more easily be seen in the distribution shown in the inset (Lorentzian curves). Figure 3.11 (d) shows a TEM image of the area within the red box in figure 3.11 (b) and attempts to highlight the separate Au and Ge phases. The red lines mark the edges of the particles and what we believe to be the interface between the two phases. It should be noted that it is not definite which phase is Au and which is Ge. A more suitable technique would have been HAADF-STEM imaging as the high-angle scattered electrons are very sensitive to differences in atomic number. Hence, it is a more accurate method for identifying separate elements. However, we are reasonably confident that the labels of the phases in figure 3.11 (c) are correct. Figures 3.12 and 3.13 present a similar analysis for the 5 nm Au/1 nm Ge bilayer film and Au film respectively. Comparing part (c) in figures 3.11, 3.12 and 3.13, the difference in particle sizes above the eutectic temperature and after cooling to room temperature becomes less significant as the thickness of the Ge film is reduced. The difference in particle sizes for the pure Au film (figure 3.13) is negligible because Ge is obviously absent and so the particles remain solid at high temperature and during cooling (as is evident from the diffraction contrast throughout figure 3.10 (a)).

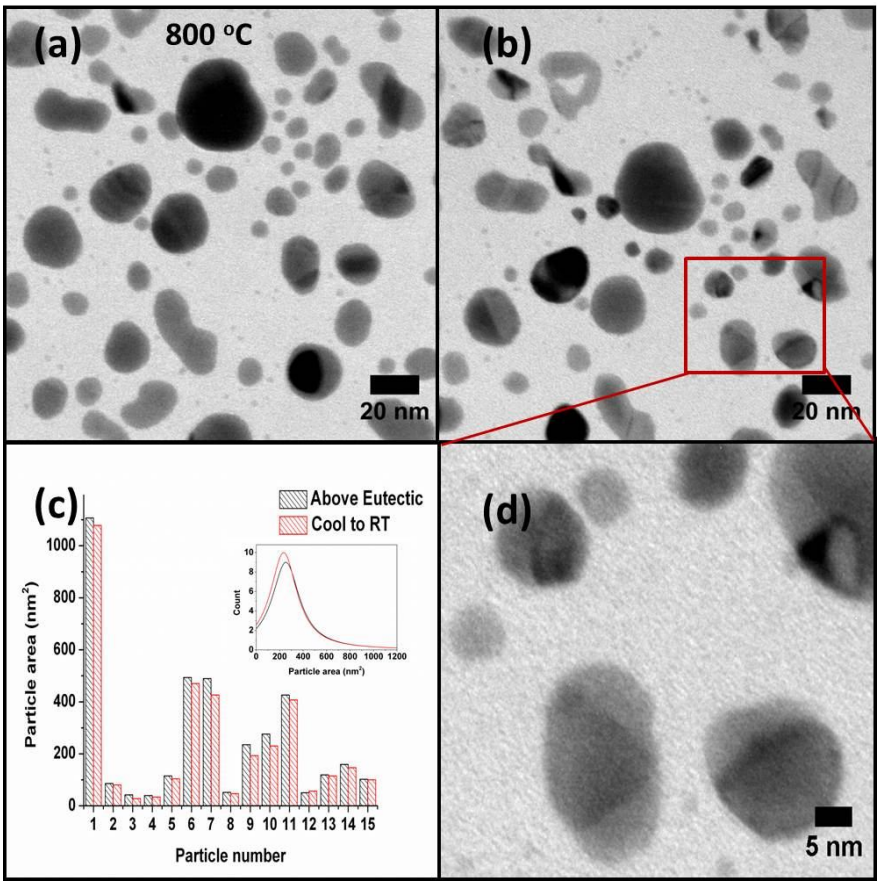


Figure 3.12 TEM analysis of Au/Ge alloy particles during in-situ temperature studies of the 5 nm Au/1nm Ge bi-layer film. (a) Low resolution TEM micrograph of Au/Ge alloy particles above the eutectic temperature. (b) Low resolution TEM micrograph of the Au/Ge particles shown in part (a) after cooling down to room temperature. (c) Bar chart showing the size differences between 15 particles measures at 800 ˚C and after cooling to room temperature. Inset shows the Lorentzian curves of histograms plotted from the sizes of the same 15 particles at high temperature and after cooling to room temperature. (d) High resolution TEM micrograph of the area inside the red box in (b), highlighting the separation of Ge from Au after cooling to room temperature.

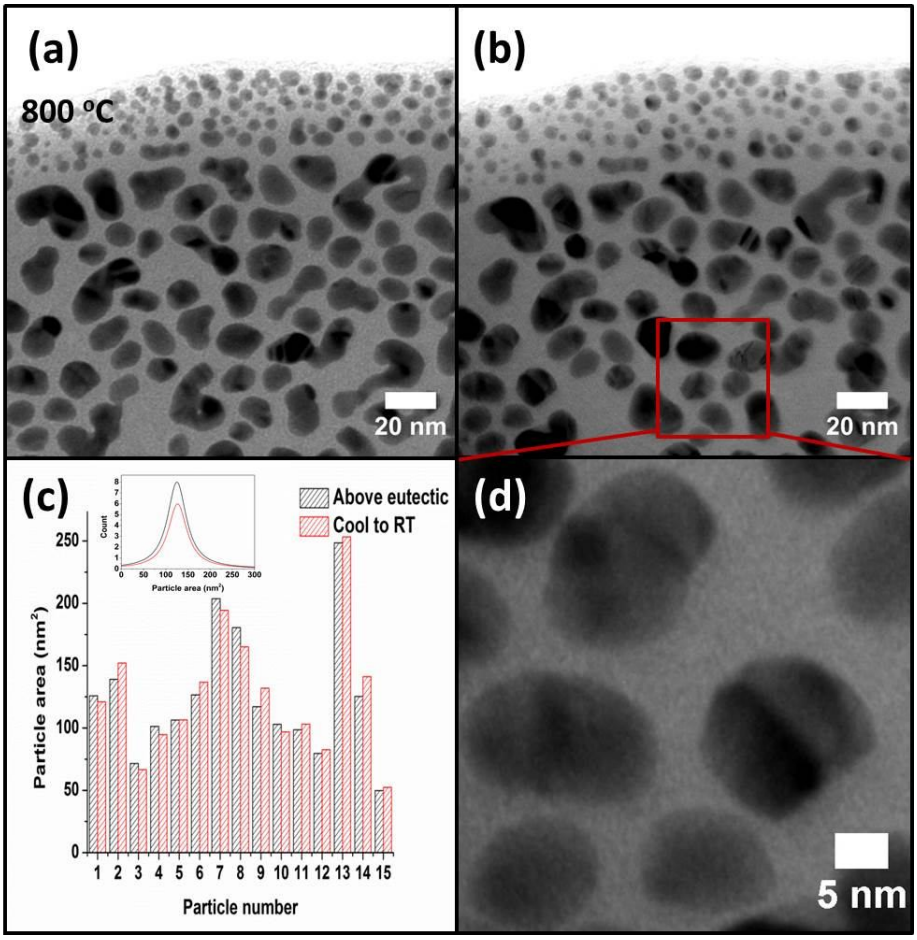


Figure 3.13 TEM analysis of Au alloy particles during in-situ temperature studies of the 5 nm Au film. (a) Low resolution TEM micrograph of the sintered Au islands above the eutectic temperature. (b) Low resolution TEM micrograph of the Au islands shown in part (a) after cooling down to room temperature. (c) Bar chart showing the size differences between 15 particles measures at 800 ˚C and after cooling to room temperature. Inset shows the Lorentzian curves of histograms plotted from the sizes of the same 15 particles at high temperature and after cooling to room temperature. (d) High resolution TEM micrograph of the area inside the red box in (b).

The mismatch in sizes between the particles at 800 ºC and room temperature gradually becomes more significant with thicker Ge layers, as summarised in figure 3.14. This observation is reasonable due to the higher content of the Ge component in the eutectic binary alloy particles for the bilayer film with thicker Ge layers. Also the interface between the Au and Ge after cooling to room temperature is less

discernible in the TEM micrographs for the Au (5nm)/Ge (1nm) films due to weaker contrast between the two phases (figures 3.12 and 3.13). In-situ TEM annealing experiments with Au and Au/Ge films produced significant insights into the formation of eutectic binary alloy seeds and contribution of higher Ge supersaturation in the nucleation process.

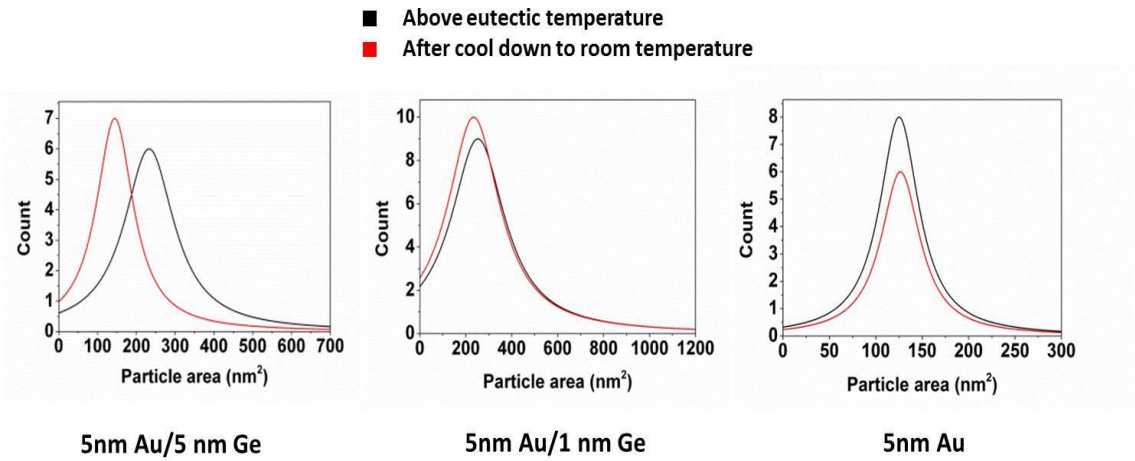


Figure 3.14 Summary of the particle size distributions from part (c) of figure 3.11, figure 3.12 and figure 3.13. As the thickness of the Ge layer decreases from 5 nm to 1 nm to 0 nm (Au film), the difference in particle sizes above the eutectic temperature and at room temperature becomes less significant.

3.4 Conclusion

To conclude, a novel method of tailoring the supersaturation of the Au/Ge binary alloy system has been utilised to grow long, crystalline Ge nanowires. Au/Ge bilayer films were successfully demonstrated to increase the Ge solute concentration in the alloy seed and hence the supersaturation before the injection of a Ge precursor for nanowire growth. Nanowires were collected on a two-part substrate consisting of a Au/Ge bilayer and a Au-only film which allowed the comparison of growth dynamics under identical conditions. Lengths and growth rates were found to be greater on the Au/Ge side while growth directions and diameter were consistent on both sides. In-situ TEM was used to clarify the growth characteristics via diffraction contrast, thus enabling the comparison of the alloying procedure for the different bilayers. This unique method marks the first time a metal-semiconductor binary alloy has been used to manipulate the Ge nucleation kinetics at the triple phase boundary during nanowire growth. This approach of manipulating supersaturation with a change in the solute concentration in the alloy seed could be combined with the other critical growth kinetics influencing parameters, *i.e.* pressure, temperature, dopant concentration, precursor decomposition chemistry, equilibrium concentration *etc*. to realise an ideal scenario for much improved growth manoeuvring in nanowires. Our method opens up the possibility of engineering the growth of nanowires, thus allowing the tuning of nanowire properties for future nanowire devices.

3.5 References

(1) Cui, Y.; Lieber, C. *Science* **2001,** 291, 851.

(2) Huang, Y.; Lieber, C. *Pure. Appl. Chem.* **2004,** 76, 2051.

(3) Barth, S.; Hernandez-Ramirez, F.; Holmes, J. D.; Romano-Rodriguez, A. *Prog. Mater. Sci.* **2010,** 55, 563.

(4) Heath, J.; LeGoues, F. *Chem. Phys. Lett.* **1993,** 208, 263.

(5) Tuan, H. Y.; Lee, D. C.; Hanrath, T.; Korgel, B. A. *Chem. Mater.* **2005,** 17, 5705.

(6) Petkov, N.; Birjukovs, P.; Phelan, R.; Morris, M.; Erts, D.; Holmes, J. *Chem. Mater.* **2008,** 20, 1902.

(7) Lu, X. M.; Fanfair, D. D.; Johnston, K. P.; Korgel, B. A. *J. Am. Chem. Soc.* **2005,** 127, 15718.

(8) Andzane, J.; Petkov, N.; Livshits, A. I.; Boland, J. J.; Holmes, J. D.; Erts, D. *Nano Lett.* **2009,** 9, 1824.

(9) Ziegler, K. J.; Lyons, D. M.; Holmes, J. D.; Erts, D.; Polyakov, B.; Olin, H.; Svensson, K.; Olsson, E. *Appl. Phys. Lett.* **2004,** 84, 4074.

(10) Chockla, A. M.; Klavetter, K. C.; Mullins, C. B.; Korgel, B. A. *ACS Appl. Mater. Inter.* **2012,** 4, 4658.

(11) Seo, M. H.; Park, M.; Lee, K. T.; Kim, K.; Kim, J.; Cho, J. *Energy Environ. Sci.* **2011,** 4, 425.

(12) Chan, C. K.; Zhang, X. F.; Cui, Y. *Nano Lett.* **2008,** 8, 307.

(13) Burchhart, T.; Lugstein, A.; Hyun, Y. J.; Hochleitner, G.; Bertagnolli, E. *Nano Lett.* **2009,** 9, 3739.

(14) Garfunkel, E.; Mastrogiovanni, D.; Klein, L.; Wan, A.; Du Pasquier, A. *Abstr. Pap. Am. Chem. S.* **2008,** 236, 454.

(15) Nguyen, P.; Ng, H.; Meyyappan, M. *Adv. Mater.* **2005,** 17, 549.

(16) Cullis, A.; Canham, L.; Calcott, P. *J. Appl. Phys.* **1997,** 82, 909.

(17) Dayeh, S. A.; Picraux, S. *Nano Lett.* **2010,** 10, 4032.

(18) Givargizov, E. I., *Highly anisotropic crystals.* D Reidel Pub Co: 1987; Vol. 3.

(19) Kodambaka, S.; Tersoff, J.; Reuter, M.; Ross, F. *Phys. Rev. Lett.* **2006,** 96, 96105.

(20) Givargizov, E. I. *J. Cryst. Growth* **1975,** 31, 20.

(21) B Lewis; Anderson, J. S., *Nucleation and Growth of Thin Films.* Academic, New York: 1978.

(22) Han, N.; Wang, F.; Hou, J. J.; Yip, S. P.; Lin, H.; Fang, M.; Xiu, F.; Shi, X.; Hung, T. F.; Ho, J. C. *Cryst. Growth. Des.* **2012,** 12 6243.

(23) Xu, H.; Wang, Y.; Guo, Y.; Liao, Z.; Gao, Q.; Jiang, N.; Tan, H. H.; Jagadish, C.; Zou, J. *Cryst. Growth. Des.* **2012,** 12, 2018.

(24) Kim, B.-S.; Kim, M. J.; Lee, J. C.; Hwang, S. W.; Choi, B. L.; Lee, E. K.; Whang, D. *Nano Lett.* **2012,** 12, 4007.

(25) Kim, J. H.; Moon, S. R.; Yoon, H. S.; Jung, J. H.; Kim, Y.; Chen, Z. G.; Zou, J.; Choi, D. Y.; Joyce, H. J.; Gao, Q.; Tan, H. H.; Jagadish, C. *Cryst. Growth. Des.* **2012,** 12, 135.

(26) Jung, J. H.; Yoon, H. S.; Kim, Y. L.; Song, M. S.; Kim, Y.; Chen, Z. G.; Zou, J.; Choi, D. Y.; Kang, J. H.; Joyce, H. J.; Gao, Q.; Hoe Tan, H.; Jagadish, C. *Nanotechnology* **2010,** 21, 295602.

(27) Jung, S. J.; Lutz, T.; Boese, M.; Holmes, J. D.; Boland, J. J. *Nano Lett.* **2011,** 11 1294.

(28) Jung, S. J.; Lutz, T.; Bell, A. P.; McCarthy, E. K.; Boland, J. J. *Cryst. Growth. Des.* **2012,** 12, 3076.

(29) Ferralis, N.; Maboudian, R.; Carraro, C. *Journal of the American Chemical Society* **2008,** 130, 2681.

(30) http://www.crct.polymtl.ca/fact/documentation/SGTE/, In.

(31) Gamalski, A.; Ducati, C.; Hofmann, S. *J. Phys. Chem. C* **2011,** 115, 4413.

(32) Eisenhawer, B.; Sivakov, V.; Christiansen, S.; Falk, F. *Nano Lett.* **2013,** 13, 873.

(33) Dubrovskii, V.; Xu, T.; Lambert, Y.; Nys, J. P.; Grandidier, B.; Stiévenard, D.; Chen, W.; Pareige, P. *Phys. Rev. Lett.* **2012,** 108, 105501.

(34) Schmidt, V.; Senz, S.; Gosele, U. *Nano Lett.* **2005,** 5, 931.

(35) Sutter, E. A.; Sutter, P. W. *ACS Nano* **2010,** 4, 4943.

(36) Sutter, E.; Sutter, P. *Nano Lett.* **2008,** 8, 411.

(37) Adhikari, H.; Marshall, A.; Goldthorpe, I.; Chidsey, C.; McIntyre, P. *ACS Nano* **2007,** 1, 415.

(38) Kim, B. J.; Wen, C. Y.; Tersoff, J.; Reuter, M. C.; Stach, E. A.; Ross, F. M. *Nano Lett.* **2012,** 12, 5867.

(39) Woehl, T. J.; Evans, J. E.; Arslan, I.; Ristenpart, W. D.; Browning, N. D. *ACS Nano* **2012,** 6, 8599.

(40) Ross, F. M. *Rep. Prog. Phys.* **2010,** 73, 114501.

(41) Nikolova, L.; LaGrange, T.; Reed, B.; Stern, M.; Browning, N.; Campbell, G.; Kieffer, J.-C.; Siwick, B.; Rosei, F. *Appl. Phys. Lett.* **2010,** 97, 203102.

Controlled Growth of Germanium Nanowires from Ternary Alloy Catalysts

4

[This chapter has been prepared as an article/paper to be submitted to a peer-reviewed journal. Consequently, certain sections of the chapter such as the abstract and introduction may contain repeating paragraphs and concepts]

4.1 Abstract

We report the synthesis of germanium nanowires from Au/Ag/Ge tri-layer films deposited on SiO_2 substrates. These films were employed to simultaneously manipulate both the solute concentration (C) and equilibrium concentration (C_{eq}) of Ge in the ternary eutectic alloy catalysts during vapour-liquid-solid (VLS) nanowire growth. The manipulation of C and C_{eq} during nanowire evolution positively influenced the nanowire growth rate, resulting in the generation of high aspect ratio structures. Unique substrates, consisting of three separate sections, *i.e.* a Au film, a Au/Ag bi-layer film and a Au/Ag/Ge tri-layer film, were used to compare nanowire growth to standard Au, Au/Ag and Au/Ag/Ge seeds respectively. The use of a Au/Ag/Ge tri-layer lowered C_{eq} and increased C, thus increasing the supersaturation of Ge in the ternary alloy during VLS nanowire growth. Simultaneous manipulation of C and C_{eq} in the eutectic alloys to enhance the nanowire growth rate was also achieved by using colloidal $Au_{0.75}Ag_{0.25}$ alloy nanoparticles deposited on a Ge film. The use of nanoparticles instead of Au/Ag/Ge films yielded nanowires with lengths of almost 10 μm and mean uniform diameters of approximately 40 nm. Manifestation of the Gibbs-Thomson effect, resulting from a dependence of the mean nanowire length as a function of diameter, was observed for all of the nanowires grown from $Au_{0.75}Ag_{0.25}$ nanoparticles. In-situ TEM heating experiments performed on the as-grown nanowires enabled direct determination of Ge solute and equilibrium concentrations in the Au/Ag/Ge ternary alloy and allowed determination of the growth characteristics of nanowires cultivated from $Au_{0.75}Ag_{0.25}$ seeds.

4.2 Introduction

Germanium nanowires are regarded as promising materials for a number of applications, including nanoelectromechanical systems [1, 2], lithium-ion batteries [3-5] and field-effect transistors [6]. However, such devices require nanowires with consistent and reproducible dimensions, *e.g.* length and diameter. Tailoring nanowire dimensions by manipulating their vapour-liquid-solid (VLS) growth kinetics, allows the synthesis of micrometer and even millimetre long nanowires with uniform diameters. The VLS approach usually makes use of Au catalyst particles to seed Ge nanowires, due to the low eutectic melting temperature of the binary Au/Ge alloy and the high solubility of Ge in Au. During the VLS growth process, supersaturation acts as the driving force for layer-by-layer crystallisation at the triple phase boundary (TPB)[7]. Assuming the crystallisation of Ge nanowires is rate limiting, the enhanced rate of nanowire growth can be achieved by increasing the supersaturation of Ge in the eutectic alloy system. Tailoring the supersaturation of an alloy seed can be done by controlling either the equilibrium concentration (C_{eq}) or solute concentration (C) of the semiconductor material in the eutectic alloy system, according to equation 1 [8]:

$$\Delta\mu = kT \ln\left[\frac{C}{C_{eq}}\right] \quad (1)$$

where $\Delta\mu$ is the supersaturation of Ge in the binary alloy and k is the Boltzmann constant and T is the temperature. Supersaturation ($\Delta\mu$) of Ge in a eutectic growth system can be raised by increasing C and/or decreasing C_{eq}. Manipulation of supersaturation to influence GaAs nanowire growth has been accomplished by Han

et al. [9] by tuning the concentration of the growth species (solute concentration, *C*) during nanowire growth. Manipulation of the supersaturation by varying the solute concentration in the eutectic Au/Ga alloy seeds was achieved by altering the thickness of the Au film used to seed the nanowires. Additionally, we have previously reported the manipulation of the solute concentration (*C*), and thus the supersaturation of Ge in Au/Ge alloy systems, by using Au/Ge bi-layer films as an alternative to pure Au films for synthesising Ge nanowires [10]. Increasing the thickness of the Ge layer increased the supersaturation and yielded elevated nanowire growth rates and lengths. Another approach to increase the supersaturation ($\Delta\mu$) of Ge in the Au/Ge system, to influence the nanowire growth kinetics, is to lower the equilibrium concentration (C_e) (according to equation 1) of Ge in the liquid eutectic alloy. A feasible way to manipulate C_{eq} is to incorporate a foreign element into the collector phase, *i.e.* the metal seed particle, which can shift the liquidus phase boundary of the growth species towards a lower equilibrium concentration. For the Au/Ge binary alloy system, Ag is a preferred choice as a foreign element as it is completely miscible with Au, does not form intermetallic compounds and the bimetallic system of Au_xAg_{1-x} forms a low temperature eutectic with Ge. Biswas *et al.*[11, 12] and Chou *et al.* [13] have used Ag in the Au/Ge system to synthesise Ge nanowires. In particular, Biswas *et al.* used Ag to lower C_{eq} of Ge in the Au/Ge system to produce millimeter-long Ge nanowires [12]. Ternary alloys of Ge have been utilised to manipulate the supersaturation and hence have been investigated for several systems [14-17], which suggests their potential as future growth promoters of one-dimensional nanostructures. Moreover, the use of ternary alloys may allow doping of nanowires through the alloy seed particle [18], ensuring the incorporation of dopants into the lattice of the wire instead of along the sidewalls. Eutectic point

depression and the change in the Ge liquidus content due to nanoscale size effects [19] should also be considered for nanowire systems. Several groups have investigated nanoscale Au/Ge systems via in-situ temperature studies inside a transmission electron microscope (TEM) [8, 19-24]. These studies make use of and expand upon the nanoscale phase diagram of the Au/Ge system which was established by Sutter *et al.* [25, 26] and which compares the eutectic behaviour of the nanosystem to its bulk counterpart.

The two methods of manipulating the Ge solute concentration (C) and equilibrium concentration (C_{eq}) have been respectively detailed in our previous reports [10, 12], but as separate techniques. In this article, we report the successful combination of both approaches, increasing the Ge solute concentration and decreasing the Ge equilibrium concentration in the eutectic melts, to enhance nanowire growth kinetics through the use of Au/Ag/Ge tri-layer films. The manipulation of both C and C_{eq} respectively is subsequently extended to include the use of Au_xAg_{1-x} nanoparticle seeds along with a Ge buffer layer (instead of using a tri-layer film) to produce long nanowires with uniform diameters. Finally, the established Gibbs-Thomson relationship and in-situ TEM heating experiments are used to explain the diameter-dependent nanowire lengths for the ternary eutectic system.

4.3 Results and Discussion

4.3.1 Growth of Ge Nanowires from Au/Ag/Ge Tri-layer Films

Our experiments consisted of utilising a 3-part substrate (shown schematically in figure 4.1) to grow Ge nanowires. The substrate consisted of a Au film, a Au/Ag bi-layer and a Au/Ag/Ge tri-layer. Figure 4.2 shows SEM images of Ge nanowires grown from each of the three sections of the substrate. Nanowires grown from the Au film (10 nm), Au/Ag bi-layer (10 nm/3 nm) and the Au/Ag/Ge tri-layer (10 nm/3 nm/6 nm) are shown in figures 4.2(a), (b) and (c) respectively.

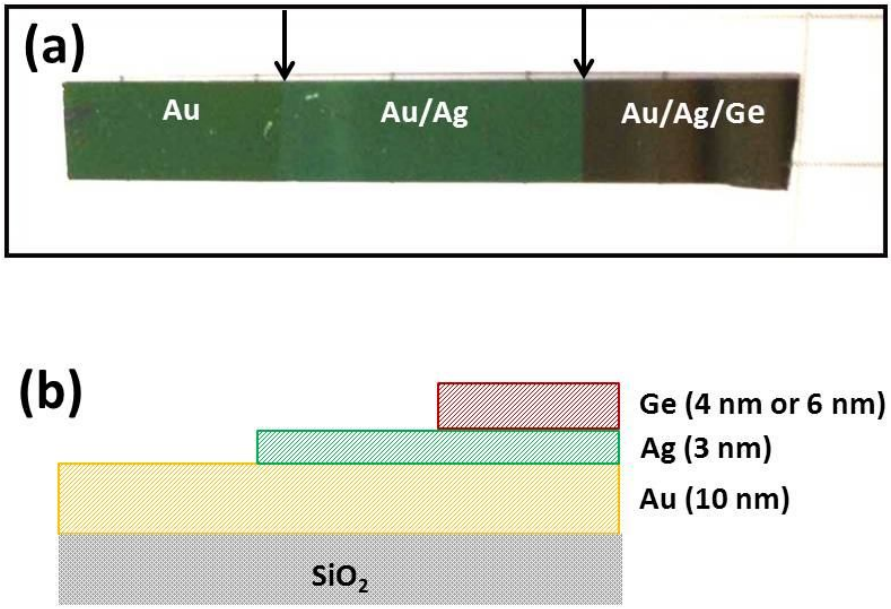


Figure 4.1 A 3-part substrate used in our experiments. The substrate consists of a 10 nm Au film deposited on a Si/SiO_2 wafer, a 3 nm Ag film deposited on one half of the substrate forming a Au/Ag bi-layer and a 4 or 6 nm Ge buffer film deposited on one-third, forming a Au/Ag/Ge tri-layer. (a) Top-down photograph of the substrate. The interfaces between the 3 sections are highlighted by black arrows. (b) Cross-sectional schematic of the substrate.

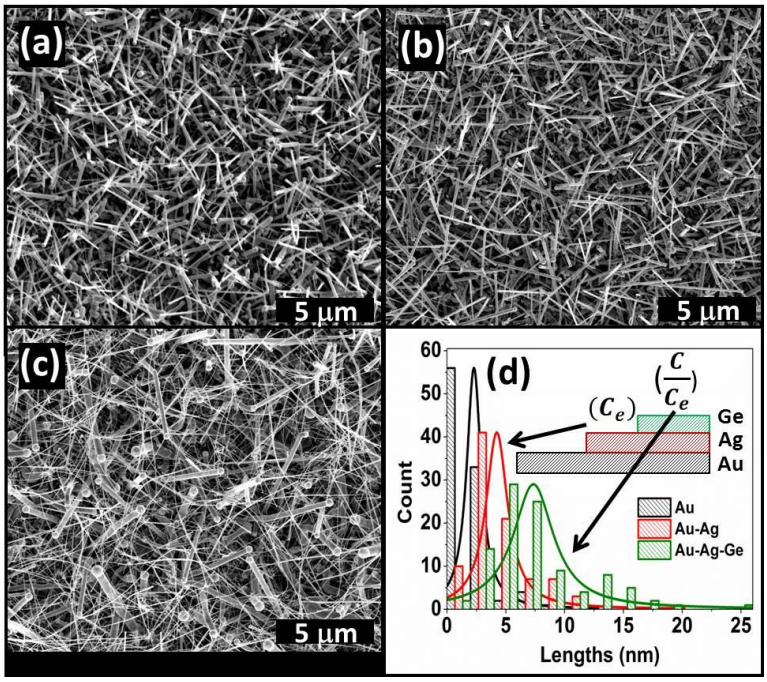


Figure 4.2 SEM images of Ge nanowires grown using a 3-part substrate. (a) Ge nanowires grown on the Au part of the 3-part substrate, (b) Ge nanowires grown on the Au/Ag bi-layer part of the 3-part substrate and (c) Ge nanowires grown on the Au/Ag/Ge part of the 3-part substrate. (d) Nanowire length distributions from the Au film, Au/Ag bi-layer and Au/Ag/Ge tri-layer showing how the mean nanowire length increases on proceeding from the Au film to the Au/Ag bi-layer and finally, to the Au/Ag/Ge tri-layer. The inset illustrates how each part of the substrate influences the growth kinetics, with the addition of Ag reducing C_{eq} in the bi-layer and the addition of Ge to Au/Ag increasing the solute concentration in the tri-layer.

Nanowires with relatively uniform diameters were synthesized from the Au and Au/Ag sections of the substrate (figures 4.2(a) and (b)) and had mean diameters of 80.2 ± 37 nm and 100.5 ± 66 nm respectively. In contrast, the Au/Ag/Ge tri-layer showed a clear bimodal distribution in radial dimensions with a mean diameter of 265.4 ± 148 nm for the thicker regime and a mean diameter of 41.3 ± 11 nm for the thinner nanowires (figure 4.2 (c)). Figure 4.2(d) compares the nanowire length distributions, with the mean lengths increasing progressively from 2.0 ± 0.9 µm for the Au film to 5.0 ± 4.2 µm for the Au/Ag bi-layer and finally, to 7.3 ± 4.2 µm for

the Au/Ag/Ge tri-layer (Ge layer is 6 nm). Figure 4.3 shows SEM images of Ge nanowires grown on the two extremes of the substrate, *i.e.* the Au and Au/Ag/Ge layers, and confirms (via cross-sectional SEM imaging 90 degrees to the beam) that different growth regimes exist on opposite sides of the substrate, *i.e.* longer nanowires on the Au/Ag/Ge layer were observed. Thus, adding a Ag layer to the conventional Au film (Au/Ag bi-layer) produced longer nanowires than standard Au seeded nanowire growth. Moreover, further addition of a Ge layer to the Ag/Au films, *i.e.* to form a Au/Ag/Ge tri-layer, produces even longer nanowires.

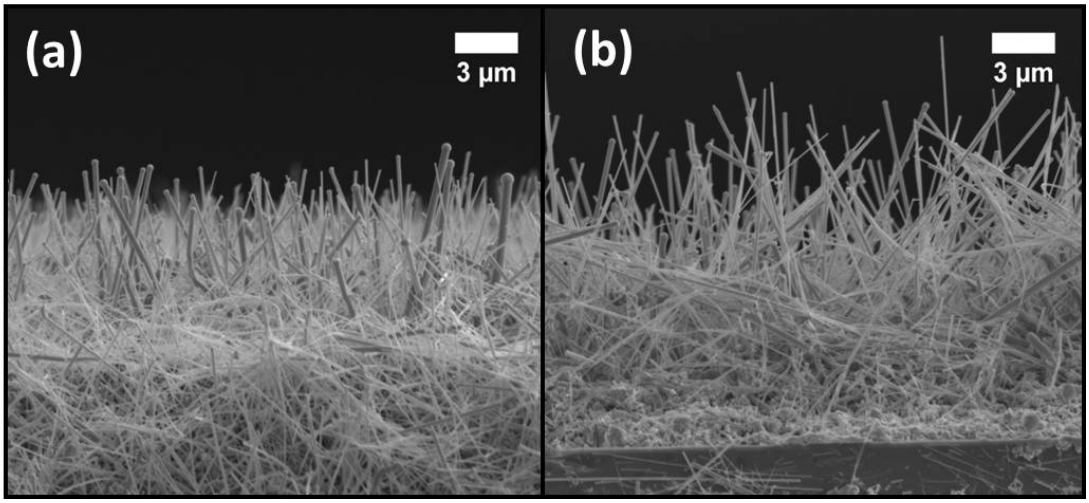


Figure 4.3 SEM images showing Ge nanowire growth at an angle of 90 degrees to the electron beam. (a) SEM image showing Ge nanowires grown on the Au side of a 3-part substrate (shown in figure S1). (b) SEM image showing Ge nanowires grown on the Au/Ag/Ge side of a 3-part substrate.

Figure 4.4 shows high-resolution TEM micrographs of typical nanowires grown on all 3 sections of the substrate. Monocrystalline Ge is confirmed with a [111] growth orientation for all of the nanowires analysed by SAED. These nanowires are representative of the majority of the nanowires grown on the 3-part substrates, with negligible differences in structure and orientation between the Au film, the Au/Ag bi-layer and the Au/Ag/Ge tri-layer.

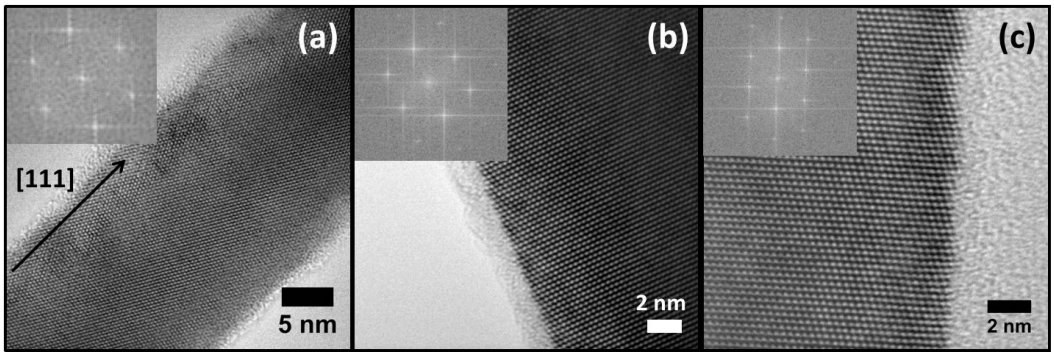


Figure 4.4 TEM images of Ge nanowires grown from a 3-part substrate. (a) A nanowire grown from the Au film. (b) A Ge nanowire grown from the Au/Ag bi-layer and (c) a nanowire grown from the Au/Ag/Ge tri-layer. The images all show monocrystalline Ge nanowires with a [111] growth orientation. Insets are the fast fourier transforms (FFTs) taken of the respective nanowires confirming the growth direction.

Figure 4.5 shows a high-angle-annular-dark-field (HAADF) STEM image of one such nanowire grown on the Au/Ag/Ge side of the substrate. The EDX scans confirm the presence of both Ag (24.6 %) and Au (75.4 %) in the seed particle.

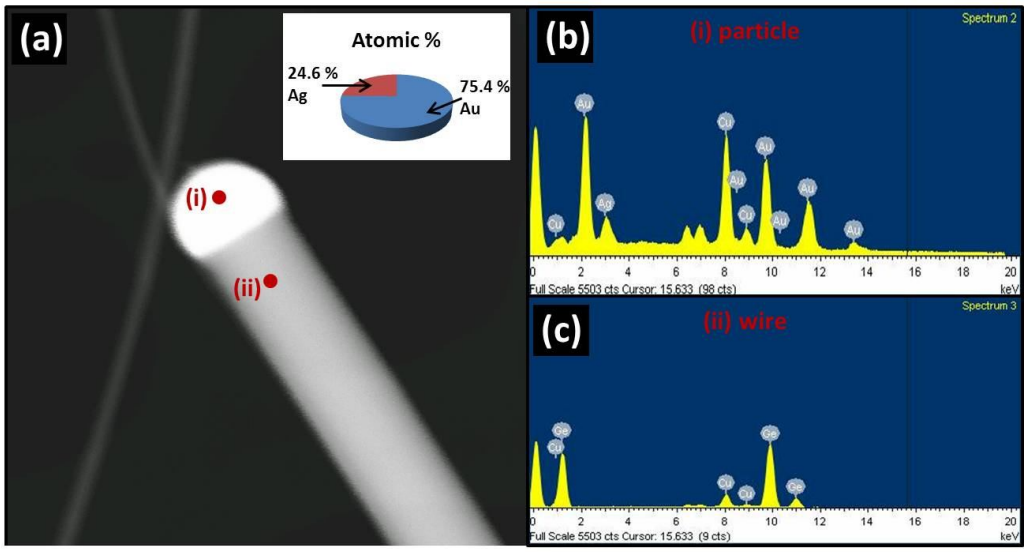


Figure 4.5 STEM analysis of a Ge nanowire grown from a Au/Ag seed. (a) High angle annular dark field (HAADF) STEM image of a Ge nanowire grown from a Au/Ag seed. Inset shows the atomic % of Ag and Au in the seed particle on top of the nanowire. (b) EDX spectrum of the seed taken at point (i) in (a). (c) EDX spectrum of the wire taken at point (ii) in (a).

STEM mode rasters the beam across the area of interest (much like an SEM) and builds up the image point-by-point. It is used for the EDX scans because it narrows the electron beam to a small probe which can be employed to accurately scan precise points for determining elemental composition. Using regular TEM mode would spread the beam, and so would likely include Ge from the nanowire in the seed scans.

4.3.2 Manipulation of the Equilibrium Concentration

The addition of Ag as a foreign element into the phase pure Au system in order to reduce the equilibrium concentration and produce very long nanowires has already been demonstrated [12]. Figure 4.6(a) displays the partial phase diagram of the Au-Ge and $Au_{0.75}$-$Ag_{0.25}$-Ge system [28, 29] and shows how adding Ag to the Au/Ge binary system shifts the Ge-liquidus curve towards lower equilibrium concentrations.

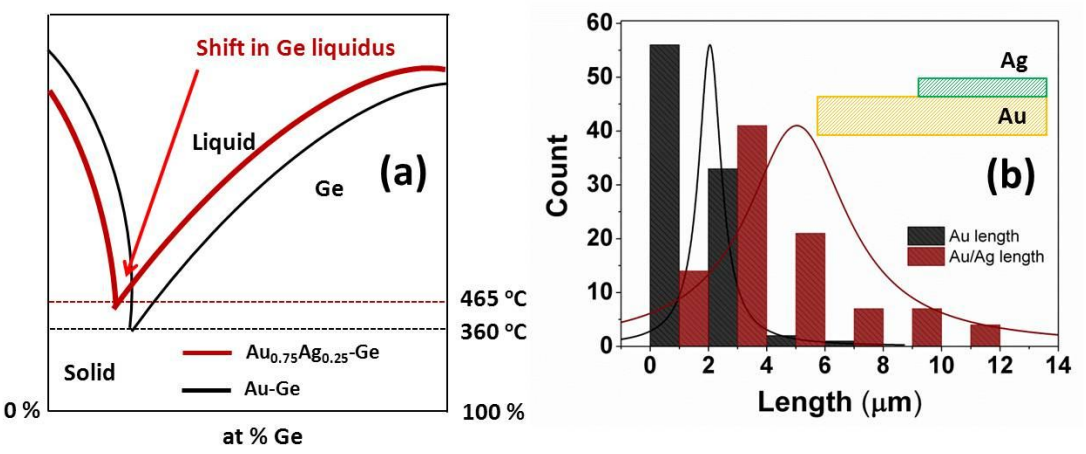


Figure 4.6 Diameter distribution highlighting the difference in lengths of nanowires grown on a Au film and a Au/Ge bilayer. (a) Phase diagram showing the shift in equilibrium concentration in the Au/Ag/Ge ternary alloy system when compared with the Au/Ge system. (b) Length distribution data comparing the lengths between nanowires grown from a Au film and a Au/Ag bi-layer.

The black line in figure 4.6(a) represents the liquidus curve for the Au/Ge binary system. At our growth temperature of 465 ^{o}C, the equilibrium concentration (C_{eq}) of Ge in the Au/Ge binary eutectic alloy is approximately 33 at.%. The red line represents the liquidus curve for the $Au_{0.75}Ag_{0.25}$/Ge ternary alloy system. Addition of Ag to the Au/Ge binary system reduces C_{eq} for a given temperature (22 at.% at the growth temperature of 465 ^{o}C) with a minimal change in eutectic temperature, thus suggesting higher supersaturation ($\Delta\mu$) of Ge in the eutectic alloy (according to equation 1) for the ternary eutectic system. As a consequence of the higher supersaturation, the nanowire growth rate increases and yields longer nanowires according to the growth model proposed by Givargizov [30]; as shown in equation 2:

$$v = b\left(\frac{\Delta\mu}{kT}\right)^2 \qquad (2)$$

where $\Delta\mu$ is the supersaturation, v is the growth rate, b is the kinetic coefficient of crystallisation and k is the Boltzmann constant and T is the temperature. We have considered the $Au_{0.75}Ag_{0.25}$-Ge binary phase diagram to explain the nanowire growth scenarios with the Au/Ag/Ge tri-layer film, as the atomic ratio of Ag (23 at %) in the bi-layer film estimated from the Au and Ag film thickness nearly matches with the $Au_{0.75}Ag_{0.25}$ system. Also, EDX studies confirmed the presence of Ag and Au in the growth seeds with a 1:3 ratio (see figure 4.5). Length distributions of nanowires grown from Au films and the Au/Ag bi-layer films, shown in figure 4.6(b), support the above argument of lowering the C_{eq} of Ge with Au/Ag alloy seeds. An increase in the mean length of the nanowires from 2.0 ± 0.9 μm for the Au seeds to 5.0 ± 4.2 μm with the Au/Ag alloy seeds clarifies the participation of higher supersaturation with the Au/Ag alloy seeds to promote faster nanowire growth.

4.3.3 Simultaneous Manipulation of both Solute and Equilibrium Concentration

To further increase the nanowire growth rate, a Ge film was introduced to the Au/Ag bi-layer. Figure 4.7(a) shows the nanowire length distributions for the Au/Ag/Ge tri-layer side of the substrate with two different Ge layer thicknesses. The distribution reveals longer nanowires for the 6 nm Ge film when compared to a 4 nm film (mean lengths of 7.5 ± 4.3 μm and 4.1 ± 2.3 μm respectively).

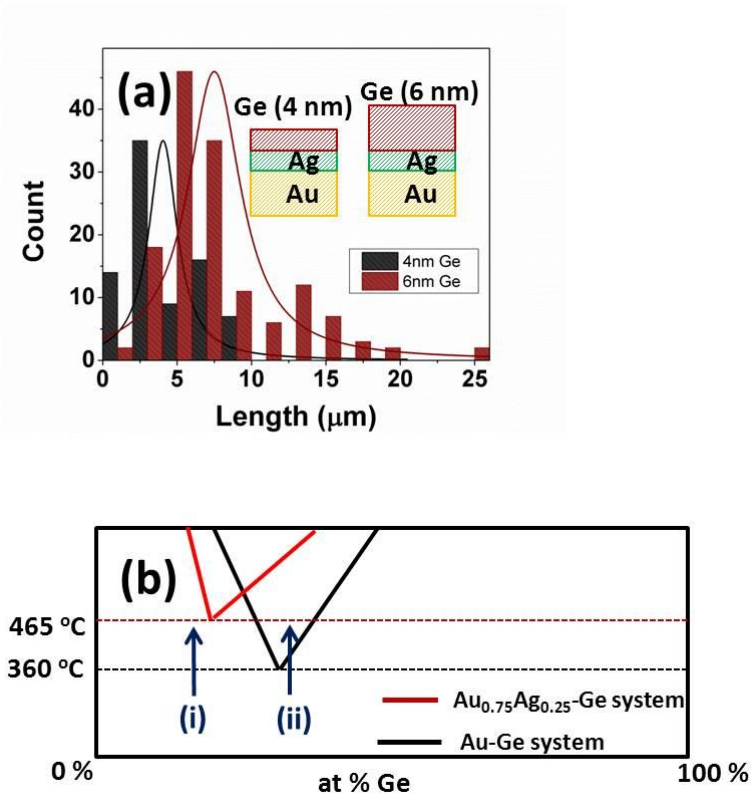


Figure 4.7 The influence of Ge film thickness on nanowire growth. (a) Length distribution data for nanowires for Ge nanowires grown from 6 and 4 nm Ge films. (b) Magnified schematic of the eutectic region of the Au/Ag/Ge phase diagram. The black curve represents the liquidus for the Au/Ge binary alloy system at the eutectic temperature of 360 ^{o}C and equilibrium composition, C_e of 28 %. The red curve represents the shift in the liquidus to a C_e of 22 % Ge in Au when Ag is added to the system, forming a Au/Ag/Ge ternary alloy.

Adding Ge to the Au/Ag film creates Au/Ag/Ge ternary eutectic alloy particles upon annealing before any Ge precursor is introduced. Consequently, this raises the Ge solute concentration (*C*) in the Au/Ag/Ge system which in turn raises the supersaturation according to equation 1, as detailed in our previous report [10]. Briefly, increasing the solute concentration of Ge in the alloy seed is associated with increasing the chemical potential of the growth species, thus increasing the driving force responsible for nanowire growth. Increasing the solute concentration through the addition of Ge films is equivalent to increasing the partial pressure of the vapour source, which has been performed previously [8] in order to increase the supersaturation of Ge. When the Ge precursor is introduced, the incubation time for Ge nucleation (and thus nanowire growth) to occur is therefore lessened according equation 3 below [20]:

$$\tau = \exp\left(\frac{b}{\Delta\mu^2}\right) \qquad (3)$$

where τ is the incubation time for growth. Figure 4.7(b) shows an enhancement of the eutectic region of the phase diagrams of the Au-Ge binary (black line) and $Au_{0.75}$-$Ag_{0.25}$-Ge ternary (red line) systems [28, 29] and traces the progression of the physical behavior of $Au_{0.75}Ag_{0.25}Ge$ ternary alloy system as the concentration of Ge in the alloy increases. The red line represents the Ge liquidus of the $Au_{0.75}$-$Ag_{0.25}$-Ge system and is shifted towards reduced equilibrium concentration as a result of incorporating Ag into the Au/Ge alloy. Further addition of a Ge film helps to pre-form Au/Ag/Ge ternary eutectic alloy particles during the annealing stage prior to nanowire growth. The annealing process creates ternary alloy catalyst melts only on the Au/Ag/Ge side of the substrate, which participate as the promoter in the

nanowire growth process. For a pure Au film or Au/Ag bi-layer, there is no Ge present and so the system remains on the far left of the phase diagram (0 % Ge). Assuming the absence of a Ge precursor, the Au and Au/Ag films do not form an eutectic alloy upon annealing at the growth temperature prior to the actual nanowire growth. On the Au/Ag/Ge side, the introduction of a 4 nm Ge film (21.3 at.%) in the Au/Ag system, places the ternary alloy system at point (i) (marked with a blue arrow in figure 4.7(b)) on the phase diagram. The Ge layer places the ternary alloy system extremely close to the equilibrium concentration for the $Au_{0.75}$-$Ag_{0.25}$-Ge system, C_e (marked by the red arrow) for supersaturation to occur. A further increase in the Ge film thickness to 6 nm, which corresponds to 29 at.% Ge in Au/Ag alloy, places the solute concentration above C_{eq} of Ge, (point (ii) in figure 4.7 (b)) resulting in a drastically reduced incubation time for nucleation (due to the increase in supersaturation). The reduced incubation time for Ge nanowire growth with the thicker (6 nm) Ge layer is reflected in the experimental results shown in figure 4.7(a), with longer nanowires being generated from the 6 nm compared to the 4 nm Ge film.

4.3.4 Growth of Ge nanowires from Au_xAg_{1-x} nanoparticles

Figure 4.8(a) shows an SEM image of the Au/Ag/Ge film after annealing for 30 min at 465 ^oC and clearly highlights a bimodal distribution in particle diameters. Ge nanowires were subsequently grown from these particles, thus also giving a bimodal distribution in nanowire diameters (265.4 ± 148 nm and 41.3 ± 11 nm), as seen in figure 4.8(b). The insets in both figures are plots of the diameter distribution confirming the bimodal diameter regime. The formation of bi-modal distributions has been reported previously in the literature [31, 32]. Barth *et al.* have reported the

formation of bimodal distributions for Ge nanowires grown from Ni:Fe films [31] and attributed the bi-modal regime to differences in the phase of small and large particles found at the tips of the wires. Also, they suggested that Ge in the ternary alloy species may have an effect on the phases of the seed during the ternary alloy formation.

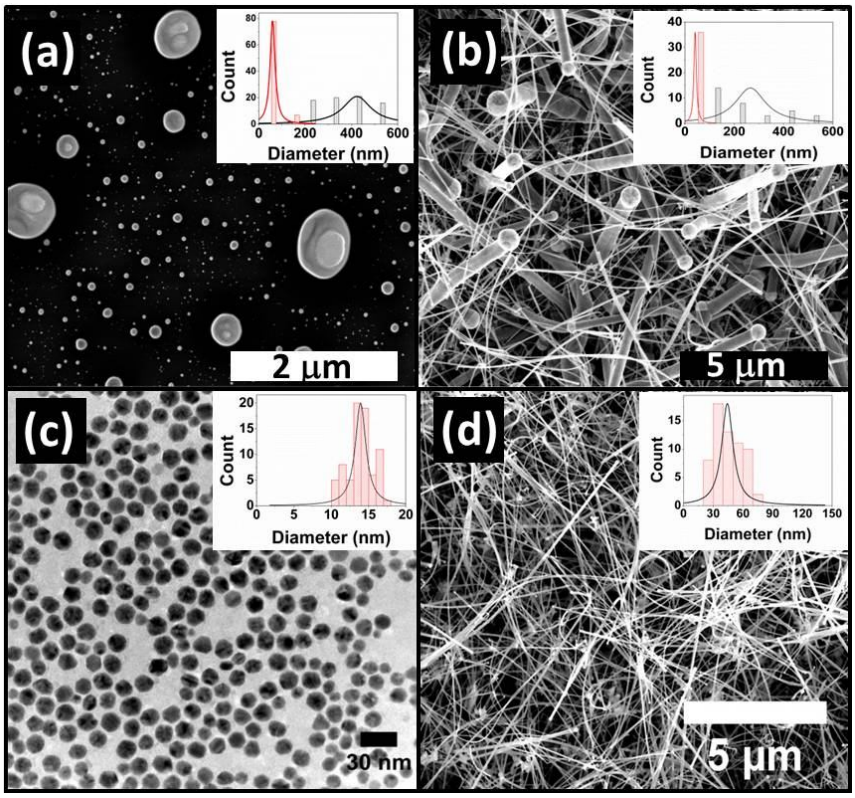


Figure 4.8 Nanowires grown from monodisperse nanoparticles. (a) SEM image of Au/Ag/Ge tri-layer after annealing for 30 min at 465 ^{o}C. (b) Ge nanowires grown from the annealed particles shown in (a). A bimodal diameter distribution is present for both the particles and nanowires. (c) TEM image of monodisperse $Au_{0.75}Ag_{0.25}$ nanoparticles dispersed on a lacey carbon grid with a mean diameter is 13.9 ± 1.9 nm. (d) SEM image of Ge nanowires grown from the $Au_{0.75}Ag_{0.25}$ nanoparticles shown in (c), with a mean diameter is 44.2 ± 14 nm. Insets in (a)-(d) are diameter distributions confirming the presence ((a) and (b)) or absence ((c) and (d)) of a bi-modal diameter regime. SEM images in (a), (b) and (d) taken using the SEM backscattered electron detector.

Similarly, Kang *et al.* also reported on the growth of Ge nanowires with a bi-modal diameter regime from Ni-Cu alloys [32]. In our case, there is no bi-modal regime on the Au film or Au/Ag bilayer portions of the substrate, as the ternary alloys do not form due to the absence of the Ge layer during annealing of the films prior to nanowire growth. Figure 4.9 shows an SEM image of both a Au film and a Au/Ag bi-layer after annealing for 30 min at 465 ^{o}C and confirms the absence of a bimodal diameter regime.

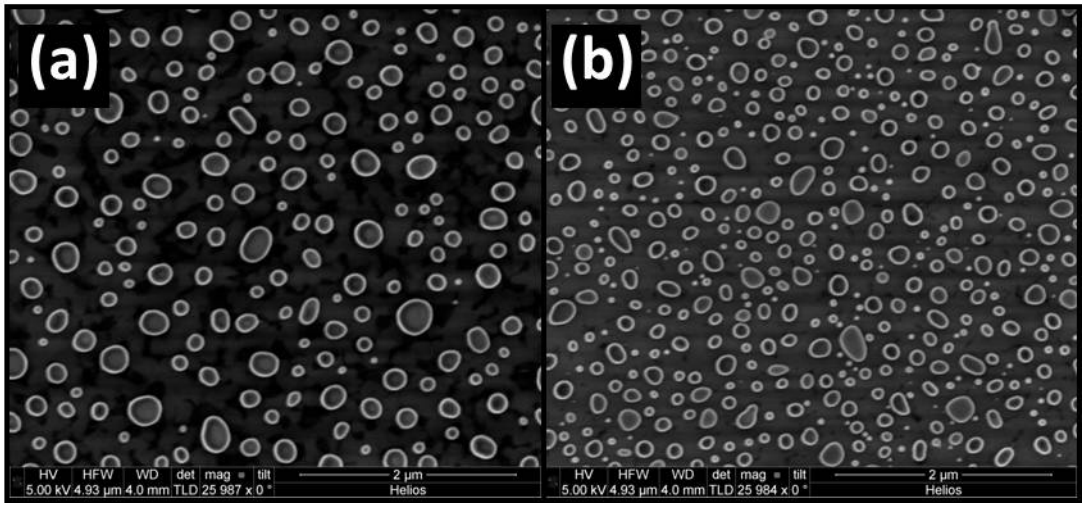


Figure 4.9. SEM images of (a) the Au/Ag bilayer and (b) the Au film after annealing for 30 min at 465 ºC. Both (a) and (b) taken using the SEM backscattered electron detector.

An in-depth study on the formation of the bi-modal diameter distribution is beyond the scope of this work and will be required to conclusively determine the exact method by which it forms. However, regardless of the mechanism of formation, bimodal diameters are generally undesirable due to the drastic differences in the Ge nanowire properties that inevitably result from such a large difference in radial dimensions. Additionally, the diameters of the nanowires obtained from the Au film and Au/Ag bi-layer were quite pronounced (mean wire diameters were

approximately 80 and 100 nm respectively), figures 4.2(a) and (b)). These large nanowire diameters are likely a result of Ostwald ripening due to surface diffusion of atoms at the relatively high temperature of 465 ^{o}C [33, 34]. Consequently, we have attempted to remove the bimodal distribution to produce nanowires with more uniform diameters and to yield thin nanowires with high aspect ratios. To this end, we have extended the above argument of manipulating both C and C_{eq} to include the synthesis of Ge nanowires from monodisperse colloidal nanoparticles (instead of evaporated films). The growth of Ge nanowires from these nanoparticles was accomplished by drop-casting $Au_{0.75}Ag_{0.25}$ alloy particles onto a Si/SiO_2 substrate that was coated in 6 nm of evaporated Ge. This combination of using a Ge layer with $Au_{0.75}Ag_{0.25}$ nanoparticles enabled us to continue influencing both the equilibrium concentration (by using Au/Ag alloy nanoparticles) and the solute concentration (by dropping the particles onto a Ge film). Figure 4.8(c) shows a TEM image showing the colloidal $Au_{0.75}Ag_{0.25}$ particles that were used to seed nanowire growth. The particles were monodisperse with a mean diameter of 13.9 ± 1.9 nm (inset of figure 4.8 (c)). A single surface plasmon resonance (SPR) peak observed in the absorbance spectra, as seen in figure 4.10 (a), confirmed the formation of a Au/Ag alloy instead of two different phases of Ag and Au in the sample. A blue shift of the SPR peak from similar sized Au nanoparticles (TEM image shown in figure 4.10(b)) also confirmed the formation of Au/Ag alloy nanoparticles [27].

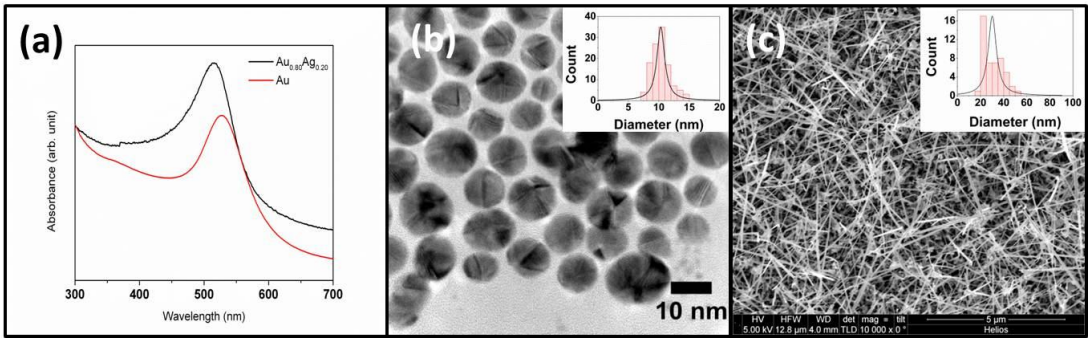


Figure 4.10. (a) UV-visible spectra of $Au_{0.75}Ag_{0.25}$ and Au nanoparticles. (b)TEM images of Au nanoparticles used to seed Ge nanowire growth. (c) SEM image of nanowires grown from the Au seeds shown in (b). The insets in (b) and (c) reveal the diameter distribution of the Au particles and Au seeded Ge nanowires respectively.

The Ge nanowires that were grown from these $Au_{0.75}Ag_{0.25}$ seeds are shown in figure 4.8(d). The SEM image and corresponding inset of the nanowire diameter distribution reveal the absence of a bimodal regime, with highly uniform diameters. The mean diameter of the Ge nanowires grown from the alloy nanoparticle seeds was 44.2 ± 14 nm, which is much smaller than the mean diameter obtained from the evaporated films. The atomic percentage of Au and Ag at the metal tip of the nanowire is confirmed by EDX analysis (72.3 at% Au and 27.7 at% Ag) as shown in figure 4.11 and it should be noted that this composition is nearly identical to the composition of the Au/Ag metal tip at the end of the nanowires grown from the Au/Ag/Ge trilayer film (figure 4.5). To compare the growth kinetics of $Au_{0.75}Ag_{0.25}$-seeded Ge nanowires with the phase pure Au seeded nanowires, we also used colloidal Au nanoparticles to seed Ge nanowire growth (figure 4.10(c)), for a comparison of the length scale between the two different seeds.

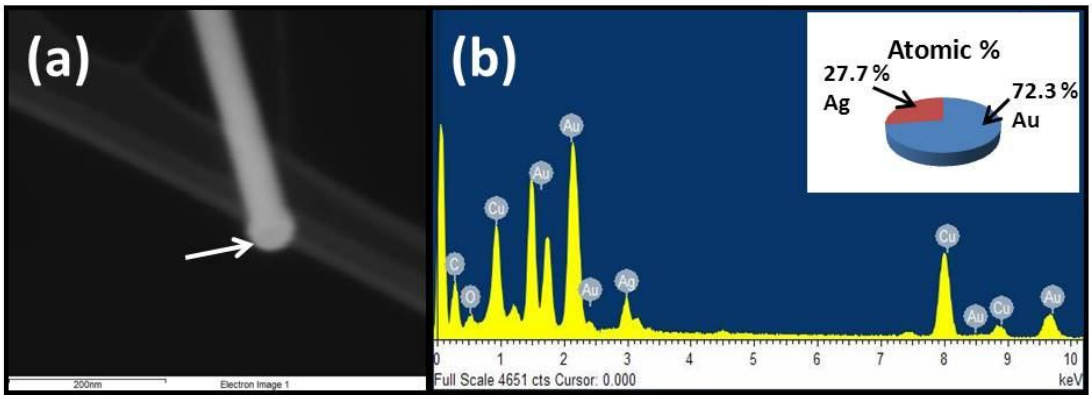


Figure 4.11 STEM analysis of a Ge nanowire grown from a $Au_{0.75}Ag_{0.25}$ nanoparticle. (a) Dark field STEM image of a Ge nanowire grown from a $Au_{0.75}Ag_{0.25}$ nanoparticle. (b) EDX spectrum of the seed marked by the white arrow in (a). Inset shows the atomic % of Ag and Au in the seed particle on top of the nanowire.

Figure 4.12(a) shows the comparison of the length distributions of nanowires synthesised from Au seeds deposited on a bare SiO_2 substrate (2.3 ± 0.9 μm), nanowires synthesised from Au seeds deposited on a 6 nm Ge film (4.4 ± 1.7 μm) and nanowires grown from $Au_{0.75}Ag_{0.25}$ seeds deposited on a 6 nm Ge film (8.7 ± 5.2 μm). The increase in length from 2.3 ± 0.9 μm for Au-nanoparticle seeded Ge nanowires to 4.4 ± 1.7 μm for Au-film seeded growth, with a Ge buffer layer, confirms the participation of the Ge film in the growth process by increasing the Ge solute concentration in the Au/Ge alloy and hence positively influencing Ge supersaturation. The further increase in the nanowire length to 8.7 ± 5.2 μm for nanowires synthesised from the $Au_{0.75}Ag_{0.25}$ seeds deposited on the 6 nm Ge layer is due to the reduction in the equilibrium concentration (C_{eq}) as a result of adding Ag to the Au/Ge system, along with the increase in the solute concentration (with Ge buffer layer).

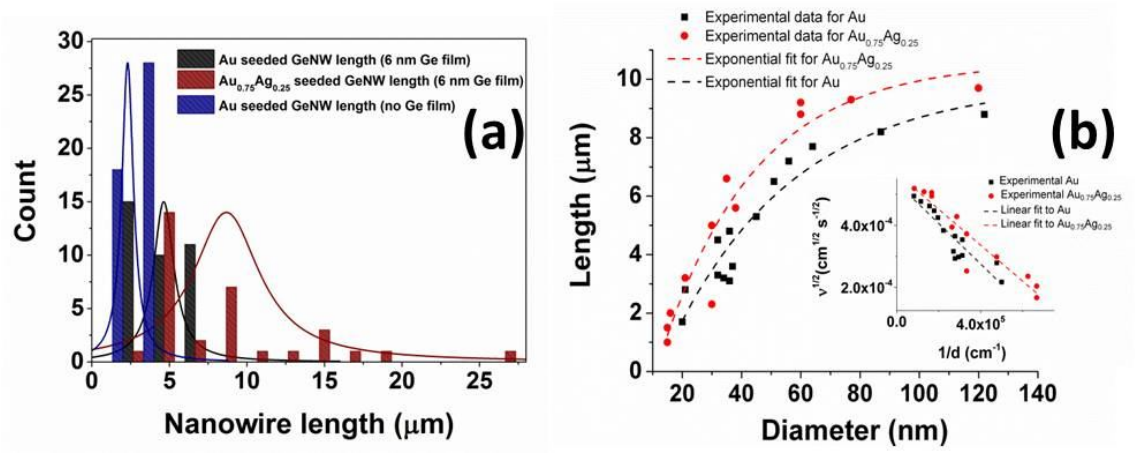


Figure 4.12. Plots of nanowire length and growth rate showing the applicability of the Gibbs-Thompson effect (a) Length distribution comparing the lengths of Ge nanowires grown from Au and $Au_{0.75}Ag_{0.25}$ nanoparticles. (b) Plot of nanowire length as a function of diameter for nanowires grown from Au and $Au_{0.75}Ag_{0.25}$ nanoparticles. Inset is a plot of the square root of growth rate against the inverse of diameter for the data shown in (b).

The growth rates and lengths of the nanowires grown from the Au, Au/Ag and Au/Ag/Ge evaporated films (figure 4.2), as well as those nanowires grown from the Au and $Au_{0.75}Ag_{0.25}$ nanoparticles (figure 4.8), are summarised in table 1. The table identifies the system which yields the highest growth rate and longest nanowires as the $Au_{0.75}Ag_{0.25}$ nanoparticles deposited on a 6 nm Ge buffer layer. While we have quoted growth rates in this article, it is important to clarify that our calculations of growth rate include both the incubation time for nanowire growth and the time for normalised nanowire growth in a nucleation mediated layer-by-layer growth process.

	Length (μm)	Growth Rate (x 10^{-3} μm s^{-1})
Au	2.0	1.1
Au/Ag	5.0	2.7
Au/Ag/Ge (4 nm Ge)	5.7	3.2
Au/Ag/Ge (6 nm Ge)	7.3	4.1
Au particles (on bare SiO_2)	2.3	1.3
Au particles (Ge film)	4.4	2.4
$Au_{0.75}Ag_{0.25}$ particles (Ge film)	8.7	4.8

Table 1 Summary of lengths and growth rates of Ge nanowires

In other words, we have not separated the incubation time from the actual nanowire growth time [10]. It should be noted that it is difficult to compare the time scales for a single nucleation event in a 2D layer-by-layer growth on the 3 parts of our substrate. Millisecond timescales for the incubation time for a single nucleation event were previously predicted through a time resolved simulation study of a VLS-nanowire growth process [35], thus it is beyond the scope of our experiments to compare the timescale of a single crystallisation. However a 30 min time interval allows comparison of multiple nucleation events, which contribute together in the overall nanowire growth process [22]. In other words, quantifying each nucleation and lateral growth separately is beyond the scope of this work, but has been investigated elsewhere [36]. For nanowire growth near the eutectic temperature, where simultaneous multiple nucleation events contribute together towards nanowire growth kinetics [22], the nucleation time of each step at the TPB is influential [35]. The incubation time for a single nucleation event mainly depends on the supersaturation

and hence on the equilibrium composition of the eutectic alloys [20]. The enhanced supersaturation with the Ge buffer layer and Au/Ag alloy seeds reduces the incubation time and increases the nucleation rate for each step, resulting in an overall faster nanowire growth rate.

4.3.5 Diameter Dependent Studies and the Gibbs-Thomson Effect

Figure 4.12 (b) presents nanowire lengths as a function of diameter for the Au and $Au_{0.75}Ag_{0.25}$ nanoparticle seeded Ge nanowires. The mean nanowire lengths decreased progressively with diameter, with nanowires grown from the $Au_{0.75}Ag_{0.25}$-seeds yielding longer nanowires than those grown from the Au seeds over a similar diameter range. Diameter-dependent nanowires lengths can be explained by the Gibbs-Thomson effect, which provides a relationship between the curvature of the alloy particle surface and its chemical potential [30, 37]. As the difference in the chemical potential between the seed and the wire is what governs Ge supersaturation in the eutectic seed and thus the driving force behind nanowire growth, an understanding of how the Gibbs-Thomson relationship affects Ge nanowire growth using the Au/Ge binary and Au/Ag/Ge ternary alloy systems is important. The Gibbs-Thomson relationship states that at nanoscale dimensions, the growth velocity becomes diameter dependent according to equation 4 [38]:

$$\Delta\mu = \Delta\mu_0 - \left(\frac{4\Omega\alpha_{vs}}{d}\right) \quad (4)$$

where $\Delta\mu$ (supersaturation) is the chemical potential difference of Ge in the vapour phase compared to the nanowire, d is the diameter, $\Delta\mu_0$ is the difference between the chemical potentials of Ge at a planar boundary, Ω is the atomic volume of the

semiconductor species and α is the specific free energy of the nanowire surface. Increasing the nanowire diameter causes an overall increase in the supersaturation (according to equation 4) and consequently, an increase in the driving force behind nanowire growth. Also, small diameter nanowires tend to grow more slowly than large diameter wires due to increased stabilisation of the particle seed as a result of capillary effects [39], resulting in longer lengths for large diameter nanowires, which is reflected in figure 4.12(b). An interesting result from figure 4.12(b) is shown in the inset, which is a plot of the square root of growth rate against the inverse of diameter for nanowires grown using the Au and $Au_{0.75}Ag_{0.25}$ nanoparticle seeds. The linear dependence shows that increasing the growth rate (by increasing the supersaturation) decreases the theoretical cut-off diameter below which nanowire growth rate should cease, according to Dayeh *et al.* [8] The inset in figure 4.12(b) gives a lower cut-off diameter for the $Au_{0.75}Ag_{0.25}$ seeded GeNWs than for the Au seeded GeNWs. This is expected, as adding Ag to the Au/Ge system lowers C_{eq} and increases the supersaturation. The cut-off diameters are 13.6 nm and 10.8 nm for the Au and $Au_{0.75}Ag_{0.25}$ seeded nanowires respectively in our growth scenario. Dayeh *et al.* identified several mechanisms that lower the cutoff diameter to achieve very thin nanowires, including adding dopant precursors to lower the surface tension of the nanowire facets [8]. Our results show that the addition of a foreign element such as Ag could also potentially be utilised to lower the cutoff diameter of GeNWs, thus yielding even higher aspect ratios.

4.3.6 In-Situ TEM Heating and the Gibbs-Thomson Effect

To further investigate the supersaturation behaviour of Ge in the Au/Ge and Au/Ag/Ge alloy systems, as a function of nanowire dimensions, and to support the nanowire growth characteristics, as a function of Ge equilibrium concentration (C_{eq}), in-situ TEM heating experiments were performed on nanowires of varying diameters. The Gibbs-Thomson effect, discussed above is summarised in equation (5) [8] below in terms of Ge solute concentration in nanoscale and bulk equilibrium concentrations:

$$C = C_{eq} \exp(4\Omega\alpha / dkT) \qquad (5)$$

where C is the Ge solute concentration in the alloy for a nanowire of radial dimension d, C_{eq} is the equilibrium concentration for the bulk counterpart, α is the surface energy, Ω is the molar volume of Au and kT is the Boltzmann distribution. Figure 4.13(a) shows a TEM image of a Ge nanowire grown from Au/Ag/Ge ternary alloy catalysts. Figure 4.13(b) represents the same nanowire after heating to the growth temperature of 465 ^{o}C.

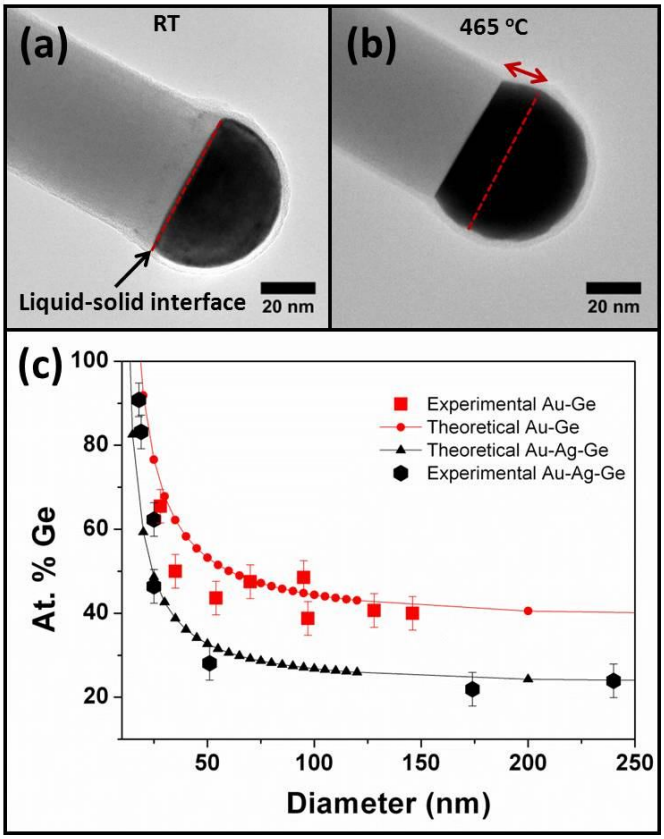


Figure 4.13. Data obtained from in-situ TEM heating of Ge nanowires grown from $Au_{0.75}Ag_{0.25}$ and Au nanoparticle seeds. (a) TEM image of a $Au_{0.75}Ag_{0.25}$ nanoparticle seeded Ge nanowire at room temperature. (b) TEM of the same nanowire after heating to the growth temperature of 465 ^{o}C. (a) and (b) show the expansion of the nanowire liquid-solid interface as a result of Ge uptake into the seed. (c) Plot of the equilibrium Ge atomic % calculated from particle expansion as a function of nanowire diameter for the Au/Ge (red squares) and Au/Ag/Ge (black hexagons) alloy systems. Simulated curves for the experimental data for the Au/Ge (red line) and Au/Ag/Ge (black line) of the supersaturation of Ge in Au and $Au_{0.75}Ag_{0.25}$ nanoparticles are included.

The expansion of the liquid-solid interface into the nanowire as a result of Ge uptake into the seed upon heating is obvious and was shown previously by Sutter *et al.*[40] Additional TEM images of the in-situ TEM heating of nanowires grown from both Au and $Au_{0.75}Ag_{0.25}$ nanoparticle seeds are presented in figure 4.14.

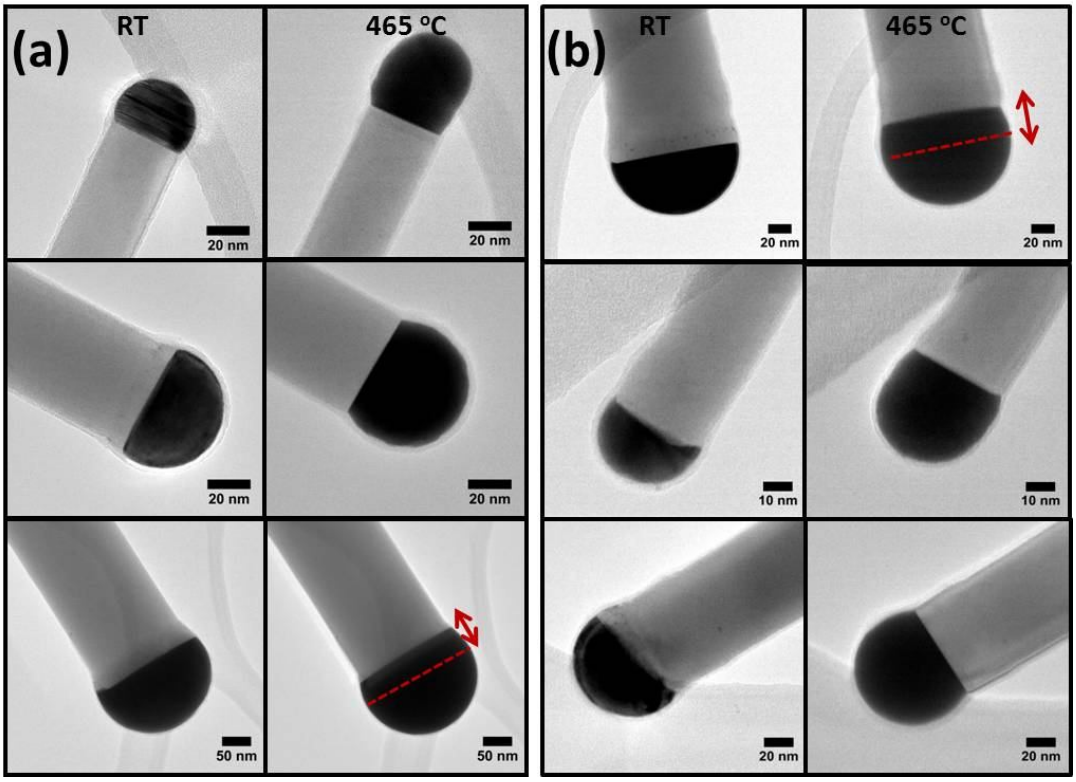


Figure 4.14 In-situ TEM heating of Ge nanowires grown from monodisperse nanoparticles. (a) Ge nanowires grown from $Au_{0.75}Ag_{0.25}$ seeds. (b) Ge nanowires grown from Au seeds. In both (a) and (b), the panels on the left represent nanowires at room temperature and the panels on the right are the same nanowires after heating to the growth temperature of 465 ºC. The expansion of the liquid-solid interface into the nanowire is clearly evident.

The expansion of the seed particle was used to calculate the Ge concentration in the seed, following the approaches outlined by Sutter *et al.* [25, 26] and these calculations are summarised in Appendix 2. Figure 4.13(c) depicts the equilibrium Ge concentration in the metal containing tip of the nanowires as a function of nanowire diameter for both the Au/Ge and Au/Ag/Ge systems. The diameter dependence on the nanoscale equilibrium concentration showed a clear increase in the equilibrium Ge atomic fraction (C_{eq}) for nanowires of decreasing diameter with both seeds. This increase in C_{eq} leads to a lowering of the supersaturation and growth kinetics

according to the Givagizov model [30]. The plot shown in figure 4.13(c) infers a lower equilibrium concentration (higher supersaturation) for the Au/Ag/Ge system compared to the Au/Ge system for a given diameter range, thus supporting the role of a lowered equilibrium concentration in yielding higher nanowire growth rates and longer lengths; observed for nanowires grown using the Au/Ag/Ge ternary system. Considering the diameter dependence on equilibrium concentration, equation (5) above gives a theoretical Ge concentration curve as shown by the black (Au/Ag/Ge) and red (Au/Ge) lines in figure 4.13(c), similar to that obtained by Han *et al.* for the Au-Ga system [9]. The red squares and black hexagons on the plot represent the experimental results for the Au/Ge and Au/Ag/Ge systems respectively. The experimental trend agrees well with the simulated fits for both systems, especially at higher nanowire diameters. The diameter dependent growth rate shown in figure 4.12 (b) and the size-dependent equilibrium concentration in figure 4.13(c) can both be explained by the Gibbs-Thomson effect, which is summarised by equation (6) in terms of nanoscale and bulk Ge equilibrium concentration:

$$\frac{\Delta\mu}{kT} = \frac{\Delta\mu_0}{kT} - \frac{1}{\kappa}\ln\left(\frac{C}{C_{eq}}\right) \qquad (6)$$

This equation, as reported by Dayeh *et al.* [8] and obtained by combining equation (4) and (5) clarifies that for a fixed bulk equilibrium Ge concentration (C_{eq}), a lower equilibrium Ge concentration at the nanoscale results in a higher supersaturation ($\Delta\mu$) and hence a higher nanowire growth rate. A similar equation was also utilised by Wu *et al.* to reflect diameter dependent supersaturation [41]. The in-situ TEM heating experiments showing lower nanoscale equilibrium concentration for larger diameter nanowires supports the observation of diameter-dependent nanowire

growth rates, as shown in figure 4.12. Moreover, the addition of a Ge layer to increase the solute concentration (C) also increases the supersaturation according to equation (6).

4.4 Conclusions

To conclude, we report for the first time the successful manipulation of both the Ge solute concentration (C) and equilibrium concentration (C_{eq}) in the Au/Ag/Ge ternary alloy system, to produce high aspect ratio Ge nanowires. A 3-part substrate consisting of a Au film, a Au/Ag bi-layer and a Au/Ag/Ge tri-layer was utilised to compare nanowire growth. Nanowire lengths were found to progressively increase with the addition of Ag and Ge films to the Au coated substrate. A bi-modal diameter distribution was observed for nanowires grown from the Au/Ag/Ge tri-layer film and was subsequently eliminated through the combination of colloidal $Au_{0.75}Ag_{0.25}$ nanoparticle seeds and a Ge reaction layer. Size-dependent properties of Ge nanowires seeded from Au and $Au_{0.75}Ag_{0.25}$ nanoparticles were explained and compared through the Gibbs-Thompson relationship for nanowires grown from Au and $Au_{0.75}Ag_{0.25}$ nanoparticles. Finally, in-situ TEM heating experiments were conducted on the nanowires post-growth to support the size dependent growth kinetics observed for both Au/Ge binary and Au/Ag/Ge ternary alloy seeds used to catalyse Ge nanowire growth. The combination of adding a Ge film to increase the solute concentration in the Au/Ge system, while simultaneously reducing the equilibrium concentration through the incorporation of Ag, may yield a highly ideal growth scenario in future work when combined with other growth kinetic influencing parameters such as temperature and pressure.

4.5 References

(1) Andzane, J.; Petkov, N.; Livshits, A. I.; Boland, J. J.; Holmes, J. D.; Erts, D. *Nano Lett.* **2009,** 9, 1824.

(2) Ziegler, K. J.; Lyons, D. M.; Holmes, J. D.; Erts, D.; Polyakov, B.; Olin, H.; Svensson, K.; Olsson, E. *Appl. Phys. Lett.* **2004,** 84, 4074.

(3) Chockla, A. M.; Klavetter, K. C.; Mullins, C. B.; Korgel, B. A. *ACS Appl. Mater. Inter.* **2012,** 4, 4658.

(4) Seo, M. H.; Park, M.; Lee, K. T.; Kim, K.; Kim, J.; Cho, J. *Energy Environ. Sci.* **2011,** 4, 425.

(5) Chan, C. K.; Zhang, X. F.; Cui, Y. *Nano Lett.* **2008,** 8, 307.

(6) Burchhart, T.; Lugstein, A.; Hyun, Y. J.; Hochleitner, G.; Bertagnolli, E. *Nano Lett.* **2009,** 9, 3739.

(7) B Lewis; Anderson, J. S., *Nucleation and Growth of Thin Films.* Academic, New York: 1978.

(8) Dayeh, S. A.; Picraux, S. *Nano Lett.* **2010,** 10, 4032.

(9) Han, N.; Wang, F.; Hou, J. J.; Yip, S. P.; Lin, H.; Fang, M.; Xiu, F.; Shi, X.; Hung, T. F.; Ho, J. C. *Cryst. Growth. Des.* **2012,** 12 6243.

(10) O'Regan, C.; Biswas, S.; O'Kelly, C.; Jung, S. J.; Boland, J. J.; Petkov, N.; Holmes, J. D. *Chem. Mater.* **2013,** 25, 3096.

(11) Biswas, S.; Singha, A.; Morris, M. A.; Holmes, J. D. *Nano Lett.* **2012,** 12, 5654.

(12) Biswas, S.; O'Regan, C.; Petkov, N.; Morris, M. A.; Holmes, J. D. *Nano Lett.* **2013**.

(13) Chou, Y.-C.; Wen, C.-Y.; Reuter, M. C.; Su, D.; Stach, E. A.; Ross, F. M. *ACS Nano* **2012,** 6, 6407.

(14) Wang, J.; Liu, Y. J.; Tang, C. V.; Liu, L. B.; Zhou, H. Y.; Jin, Z. P. *Thermochim. Acta.* **2011,** 512, 240.

(15) Wang, J.; Leinenbach, C.; Roth, M. *J. Alloy. Compd.* **2009,** 481, 830.

(16) Wang, J.; Leinenbach, C.; Roth, M. *J. Alloy. Compd.* **2009,** 485, 577.

(17) Jin, S.; Duarte, L. I.; Huang, G.; Leinenbach, C. *Monatsh. Chem.* **2012,** 143, 1263.

(18) Sutter, E.; Sutter, P. *Appl. Phys. A-Mater.* **2010,** 99, 217.

(19) Edwin J. Schwalbach; Voorhees, P. W. *Nano Lett.* **2008,** 8, 3739.

(20) Kim, B. J.; Wen, C. Y.; Tersoff, J.; Reuter, M. C.; Stach, E. A.; Ross, F. M. *Nano Lett.* **2012,** 12, 5867.

(21) Gamalski, A.; Tersoff, J.; Sharma, R.; Ducati, C.; Hofmann, S. *Phys. Rev. Lett.* **2012,** 108, 255702.

(22) Gamalski, A.; Ducati, C.; Hofmann, S. *J. Phys. Chem. C* **2011,** 115, 4413.

(23) Ross, F. M. *Rep. Prog. Phys.* **2010,** 73, 114501.

(24) Kodambaka, S.; Tersoff, J.; Reuter, M.; Ross, F. *Science* **2007,** 316, 729.

(25) Sutter, E. A.; Sutter, P. W. *ACS Nano* **2010,** 4, 4943.

(26) Sutter, E.; Sutter, P. *Nano Lett.* **2008,** 8, 411.

(27) Liu, S.; Chen, G.; Prasad, P. N.; Swihart, M. T. *Chem. Mater.* **2011,** 23, 4098.

(28) Okamoto, H.; Massalski, T. *Bull. Alloy. Phase. Diagr.* **1984,** 5, 601.

(29) Borzone, G.; Hassam, S.; Bros, J. *Metall. Mater. Trans. A* **1989,** 20, 2167.

(30) Givargizov, E. I. *J. Cryst. Growth* **1975,** 31, 20.

(31) Barth, S.; Kolesnik, M. M.; Donegan, K.; Krstic, V.; Holmes, J. D. *Chem. Mater.* **2011,** 23, 3335.

(32) Kang, K.; Gu, G. H.; Kim, D. A.; Park, C. G.; Jo, M. H. *Chem. Mater.* **2008,** 20, 6577.

(33) Schmidt, V.; Wittemann, J. V.; Senz, S.; Gösele, U. *Adv. Mater.* **2009,** 21, 2681.

(34) Lotty, O.; Hobbs, R.; O'Regan, C.; Hlina, J.; Marschner, C.; O'Dwyer, C.; Petkov, N.; Holmes, J. D. *Chem. Mater.* **2012**, 25, 215.

(35) Eisenhawer, B.; Sivakov, V.; Christiansen, S.; Falk, F. *Nano Lett.* **2013,** 13, 873.

(36) Dubrovskii, V.; Xu, T.; Lambert, Y.; Nys, J. P.; Grandidier, B.; Stiévenard, D.; Chen, W.; Pareige, P. *Phys. Rev. Lett.* **2012,** 108, 105501.

(37) Laocharoensuk, R.; Palaniappan, K.; Smith, N. A.; Dickerson, R. M.; Werder, D. J.; Baldwin, J. K.; Hollingsworth, J. A. *Nature Nanotech.* **2013**.

(38) Givargizov, E. I., *Highly anisotropic crystals*. D Reidel Pub Co: 1987; Vol. 3.

(39) Homberg, V. C.; Panthani, M. G.; Korgel, B. A. *Science* **2009,** 326, 405.

(40) Sutter, E.; Sutter, P. *Nanotechnology* **2011,** 22, 295605.

(41) Wen, C. Y.; Reuter, M. C.; Tersoff, J.; Stach, E. A.; Ross, F. M. *Nano Lett.* **2009,** 10, 514.

Electrical Properties of Platinum Interconnects Deposited by Electron Beam Induced Deposition of the Carbon-Free Precursor, $Pt(PF_3)_4$

5

[This chapter has been published as a peer-reviewed paper in the Journal of Vacuum Science and Technology B.Consequently, certain sections of the chapter such as the abstract and introduction may contain repeating paragraphs and concepts]

O'Regan, C.; Lee, A.; Trompenaars, P.; Mulders, H.; R. J.; Holmes, J. D.; Petkov, N. (2013) ***J. Vac. Sci. Technol. B****, 31 :021807(1)-021807(8).*

5.1 Abstract

Comprehensive analysis of the electrical properties, structure and composition of Pt interconnects, developed via mask-less, electron beam induced deposition (EBID) of the carbon-free Pt precursor, $Pt(PF_3)_4$, is presented. The results demonstrate significantly improved electrical performance in comparison with that generated from the standard organometallic precursor, $(CH_3)_3Pt(C_pCH_3)$. In particular, the carbon-free Pt interconnects exhibited perfect ohmic behavior and resistivity that can be diminished to 0.24×10^{-3} Ω cm, which is only one order of magnitude higher than bulk Pt, in comparison to 0.2 Ω cm for the standard carbon-containing interconnects. A maximum current density of 1.87×10^{7} A cm^{-2} was achieved for the carbon-free Pt, compared to 9.44×10^{5} A cm^{-2} for the standard Pt precursor. The enhanced electrical properties of the as-deposited materials can be explained by the absence of large amounts of carbon impurities, and their further improvement by post-deposition annealing in N_2. In-situ TEM heating experiments confirmed that the annealing step induces sintering of the Pt nanocrystals and improved crystallinity which contributes to the enhanced electrical performance. Alternative annealing under reducing conditions resulted in improved performance of the standard Pt interconnects, while the carbon-free deposit suffered electrical and structural breakage due to formation of larger Pt islands.

5.2 Introduction

Reports thus far have made extensive use of lithographic, resist-based methods such as optical or electron beam lithography (EBL) followed by metal evaporation and lift-off to make electrical contacts to semiconducting nanowires [1-3] and nanotubes[4], allowing single nanowire or nanotube devices such as field-effect-transistors (FETs)[5, 6], nanoelectromechanical systems (NEMS)[7-10], and chemical sensors[11] to be demonstrated. Although successful, the process of contact definition to nanowires by metal evaporation through a lithography mask tends to be very time-consuming, with many processing steps, and normally is not applicable to fragile or flexible substrates. For rapid and flexible prototyping of single nanowire or nanotube based devices on a diverse range of substrates, direct-writing of electrical contacts via mask-less methods is more practical and poses significant advantages[12].

Among direct write techniques for metal-containing interconnects such as laser direct write and others[13], the methods based on using scanning focused electron or ion beam deposition offer necessary nanometer resolution and precision for contacting nanowires and nanotubes. Briefly, a gaseous precursor, typically organometallic, is injected into the chamber where a focused ion or electron beam is used to decompose the precursor into volatile and non-volatile species. The non-volatile species are deposited while the volatile species are pumped away into the vacuum chamber[14]. The decomposition process is a result of the interaction of surface emitted secondary electrons (SEs) in the irradiated area with locally adsorbed gas molecules delivered by a gas injector system (GIS). As a result, using either electron beam induced deposition (EBID)[15, 16] or ion beam induced deposition (IBID)[17-20], nanowire interconnects can be deposited in a single step, making it a

very facile process. Furthermore, the technique has the potential to surpass the resolution limits posed by top-down lithographic methods[21]. The IBID and EBID processes have so far been used to deposit metal-containing contacts on Si [22, 23], ZnO[24], GaN[25] and Ge[26] nanowires and carbon nanotubes[4]. Generally, the EBID process has the advantage of being less damaging for the underlying materials in comparison to the IBID process.

Unfortunately, a major disadvantage of the EBID developed metal-containing interconnects is that the metal-containing deposits are highly resistive. The standard Pt precursor used in dual-beam FIB systems is the organometallic trimethyl(methylcyclopentadienyl)platinum(IV), $(CH_3)_3Pt(C_pCH_3)$. This precursor is used for Pt layers on TEM samples being prepared for cross-sections in order to protect the sample from the damaging ion beam[27]. However, when the same precursor is used to develop interconnects, the result is a highly resistive deposit. This is due to the high carbon content, with reports quoting a carbon content as high as 80 per cent[28]. Therefore, the interconnects suffer a deterioration in resistivity which can be up to 5 orders of magnitude higher than the resistivity of pure bulk Pt (10.6×10^{-6} Ω cm). More importantly, the reported resistivity values vary significantly from one report to another, having a variation of at least several orders of magnitude. The lowest reported resistivity value for Pt interconnects deposited by using the standard ($(CH_3)_3Pt(C_pCH_3)$) precursor is $1.4 (\pm 0.2) \times 10^{-2}$ Ω cm and it is obtained after thermal annealing of the material[15].

A useful alternative to the organometallic based precursor is tetrakis (trifluorophosphine) platinum, $Pt(PF_3)_4$. This is a carbon-free liquid precursor which has not been studied in great detail until now. The carbon-free structure means that

no carbon from the precursor will contribute to carbon contained in the deposits, thus minimising carbon content while improving overall performance. While studies of the electron scattering[29], annealing[28] and structure[30] of $Pt(PF_3)_4$ have been reported previously, comprehensive studies on the electrical properties of interconnects deposited using this precursor have not. The first reported resistivity values demonstrated the immediate advantage of using this carbon-free precursor for the EBID of Pt material. Resistivity values are at least one or two orders of magnitude lower (lowest resistivity reported is at 6.9×10^{-4} Ω cm) than the lowest reported values for the $(CH_3)_3Pt(C_pCH_3)$ precursor [37]. Similarly to the $(CH_3)_3Pt(C_pCH_3)$ deposits, it is postulated that these values can be further lowered by thermal annealing, though such studies have yet to be carried out.

Herein, we report on the electrical performance and thermal evolution of individual Pt interconnects deposited using EBID of $Pt(PF_3)_4$. The improved properties of the carbon-free deposits in terms of higher breakdown currents and lower resistivity are comprehensively compared and contrasted to the standard organometallic precursor. The influence of two different thermal treatment processes over the electrical and structural properties of both types of Pt interconnects were studied. Advanced electron microscopy methods such as high angle annular dark field (HAADF) imaging coupled with electron energy loss spectroscopy (EELS) measurements of device cross-sections complement the electrical analysis data by identifying the impurities of the deposition process. TEM cross-sections (the performance of which, are described elsewhere[31]) were used to study the structure and cross-sectional area of the deposits. Additionally, in-situ TEM annealing studies of the deposits on electron transparent membranes revealed the dynamics of the post-deposition

thermal treatment and highlighted the key structural changes responsible for the improved electrical performance of the interconnects.

5.3 Results and Discussion

5.3.1 Pt Interconnect Deposition and Initial Electrical Characterisation

Before developing Pt interconnect lines, the performance of the GIS and corresponding deposition rates were monitored by developing 1 μm^2 square patterns at 5 kV and varying beam currents at constant deposition times as described in our previous report[32]. These results were used to estimate the thickness of the deposits and to calibrate the time needed to obtain the desired thickness of the Pt lines. Figure 5.1 (a) shows *I-V* curves for two devices, prepared using carbon-free and standard Pt precursors with their corresponding SEM images, used to measure the electrical performance of the interconnects. The Pt interconnects were deposited on the same substrate under identical conditions (base pressure and beam current). Initial electrical characterisation was carried out on as-prepared devices. Initially, the devices were measured in a four-point configuration to determine if there was any contact resistance contributions coming from the Pt-Au electrode contacts. For these measurements, a current is forced between two outer terminals while the potential drop between the two inner terminals is measured, enabling separation of the wire (interconnect) resistance R_{wire} from the contact resistance $R_{contact}$. Contact resistance values were obtained by comparing the resistance values obtained from the 2- and 4-probe measurements, where the 2-probe measurements allow the total resistance between the 2 inner terminals ($R_{2\text{-}probe}$) to be determined while the 4-probe

set-up allows the resistance of the Pt interconnect between the inner terminals ($R_{4\text{-}probe}$) to be obtained.

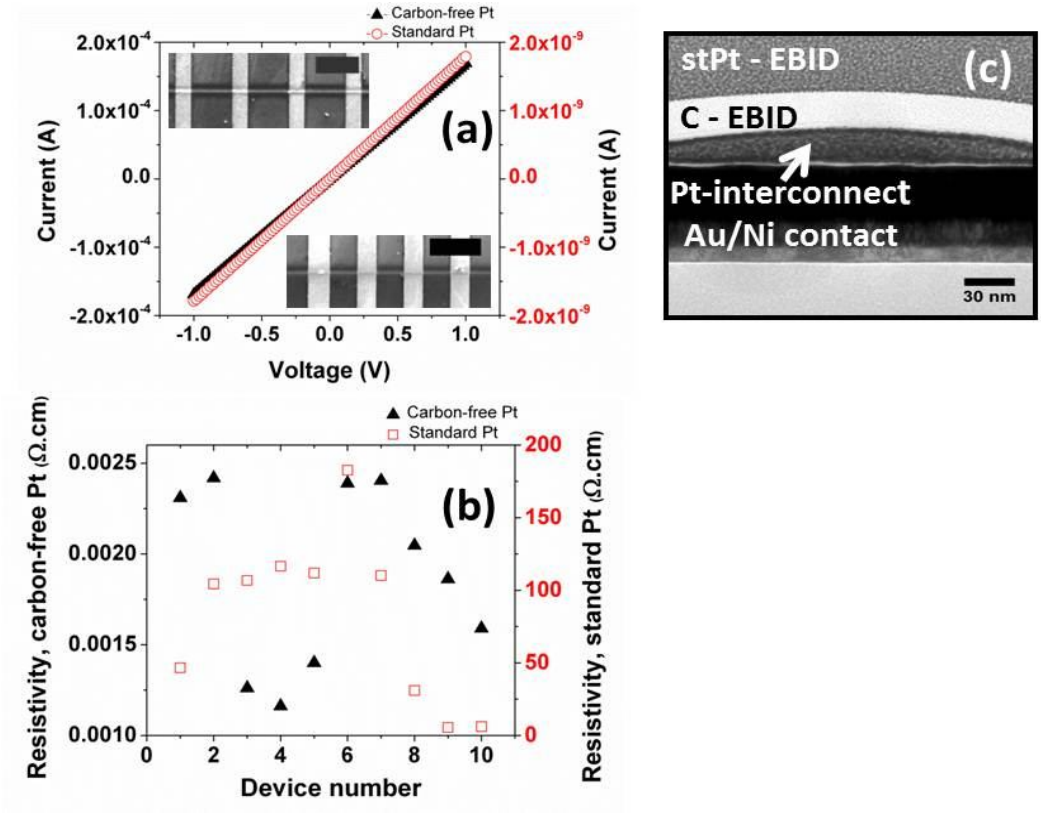


Figure 5.1 Room temperature electrical measurements of carbon-free and standard Pt interconnects. (a) 2-point I-V curves for a Pt interconnect deposited using the $Pt(PF_3)_4$ precursor and $(CH_3)_3Pt(C_PCH_3)$ precursor. The left (black) y-axis corresponds to the carbon-free Pt while the right (red) y-axis corresponds to the standard Pt. Insets are SEM images of the carbon-free Pt (top) and standard Pt (bottom) interconnects deposited across four Au/Ni contact pads. Scale bar in both is 5 μm. (b) Scatter plot showing the distribution of resistivities calculated for several devices deposited under identical conditions. Right hand (red) y-axis corresponds to standard Pt and the left hand (black) y-axis corresponds to the carbon-free Pt. (c) TEM cross-section micrograph of a carbon-free Pt interconnect. Scale bar is 30 nm.

The contact resistance ($R_{contact}$) can then be calculated from Eq. (1): $2R_{contact} + R_{4\text{-}probe} = R_{2\text{-}probe}$ [20]. The difference in slope between the 2- and 4-point measurements is due to the contact resistance. However, as can be seen in Figure 5.2, the slopes are almost identical, suggesting that the contact resistance is negligible (assumed to be

less than 100 Ω) compared to the Pt wire resistance (5.0 kΩ) and does not contribute to a significant fraction of the total resistance. As a result, 2-point measurements were used in the rest of the study. For the two-point measurement configuration, a voltage was applied between the two inner contacts as the current flowing through them was measured. As can be seen in figure 5.1 (a), the room temperature current-voltage (I-V) plots of both carbon-free and standard Pt deposits exhibited well defined linear regimes up to 1 V, suggesting that the wire-electrode contacts were ohmic.

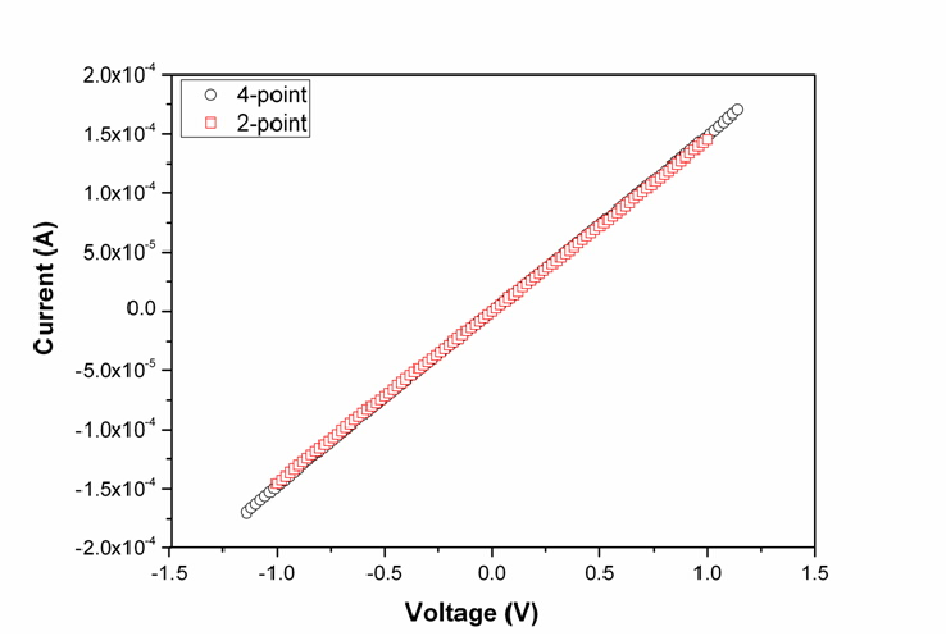


Figure 5.2 2- and 4-point I-V measurements of a liquid Pt precursor which suggest negligible contact resistance due to identical slopes.

Figure 5.1 (b) shows a scatter plot which illustrates the distribution of resistivities of both the standard and carbon-free Pt depositions (10 devices from each precursor are represented). The resistivities for the carbon-free Pt interconnects ranged from 1.2 × 10^{-3} to 2.4 × 10^{-3} Ω cm, suggesting a very high reproducibility for this specific precursor. However, the resistivities obtained for the standard Pt precursor are less consistent, ranging between 1 and 180 Ω cm. The mean resistivity (1.88 ± 0.5×10^{-3}

Ω cm) obtained for interconnects produced using the carbon-free Pt precursor is still about two orders of magnitude higher than that of bulk Pt, but almost 4 orders of magnitude lower than the obtained mean resistivity of standard Pt (82.12 ± 57.35 Ω cm). This enormous difference in resistivity confirms the advantage of using the carbon-free $Pt(PF_3)_4$ as a precursor for the EBID of Pt in a dual-beam FIB system. Overall, these results are not surprising and reflect our previous study where we show that the deposits obtained using the carbon-free Pt precursor are composed of a continuous network of polycrystalline Pt nanoparticles embedded in an amorphous matrix[32]. A detailed investigation of the composition of these structures by HAADF imaging and EELS spectral imaging is given below.

The cross-sections of the individual interconnects were obtained via cross-sectional TEM imaging, as shown figure 5.1 (c). These cross-sections provided important information regarding the structure of the Pt wires. It is clearly shown that the structures have no sharp edges and that the overall cross-section is not rectangular, a factor which affects the overall calculated resistivity ($\rho = R \times A/L$, where ρ is the resistivity, R is the resistance, A is the cross-sectional area and L is the channel length between the two inner terminals). The nominal cross-sectional area, used in the majority of the reports to calculate the resistivity of a metal-containing interconnect developed by EBID, is much smaller than the one observed by TEM cross-sections due to increased width of the deposit, as shown in figure 5.3, thus underestimating the calculated resistivity. For example, the nominal cross-section of our deposits is set at 4000 nm^2, whereas the "true" area of the cross-sectioned Pt line used in the calculations above and seen by TEM is almost 6000 nm^2. If we use the nominal cross-section area of the interconnect to calculate the resistivity, this will

decrease the calculated resistivity for the best performing device (1.2×10^{-3} Ω cm) to 0.8×10^{-3} Ω cm, which compares favorably to the already reported value of 0.69×10^{-3} Ω cm[37].

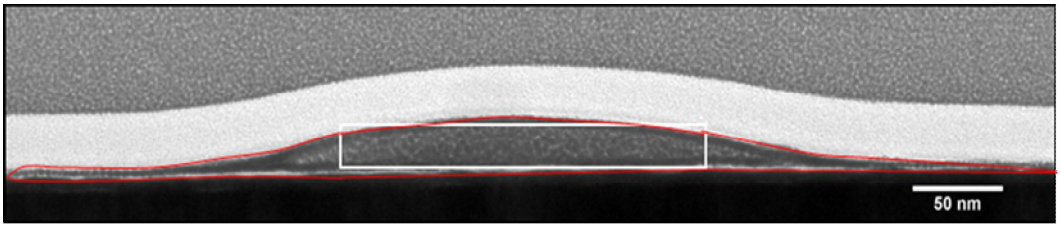


Figure 5.3 Cross-sectional TEM image of a carbon-free interconnect before annealing outlining the nominal area (in white) of the interconnect set to 4000 nm^2 and the actual cross-sectional area of the interconnect (in red) that is estimated to be 6000 nm^2. The latter is used to calculate the "true" resistivity of the material instead of the widely used nominal cross-sectional area.

In this study, a relatively low beam current of ~1.4 nA allows adequate decomposition of the Pt precursor over a time period of approximately 3 min, which compares favorably to the very high currents used by Ervin and co-workers (13 - 46 nA) to decompose the same precursor [33]. While deposition times can be reduced at high beam currents, beam sensitive samples may suffer beam damage resulting in higher resistivities. The only varying parameter in our experiments during deposition was the fluctuating residual gas in the vacuum chamber, which should be kept to a minimum to ensure reproducible results and to minimise contamination of the deposited Pt structures. A chamber pressure of 6.0×10^{-7} mbar was achieved prior to Pt deposition at all times, to minimise contamination from residual gas in the chamber.

5.3.2 Maximum Current Density Measurements

In order to further explore the interconnects formed from the carbon-free Pt precursor as possible interconnects for nanowire devices, we carried out maximum current density (J_{max}) measurements using a 2-terminal set-up on individual interconnects and compared the results with those obtained for standard Pt, as shown in figure 5.4 (a).

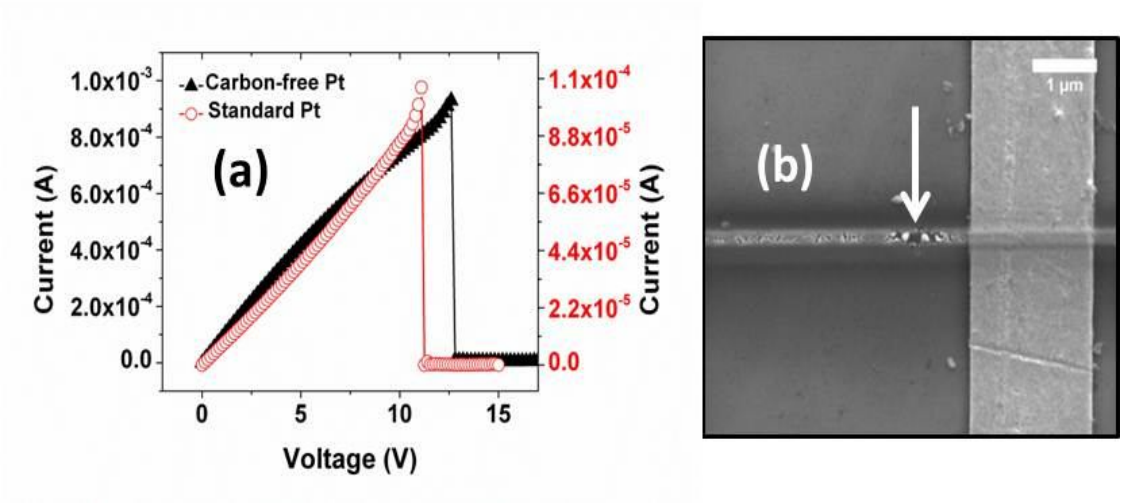


Figure 5.4 Electrical transport measurements performed on carbon-free and standard Pt interconnects. (a) I-V measurements recorded at higher applied voltages for standard Pt (open red cirlces) and carbon-free Pt (solid black triangles) interconnects. The rapid drop in current around 12 V for both interconnects is due to electrical breakdown of the wire. (b) SEM image showing the point of breakdown of the wire between the two inner electrodes. Scale bar is 1 µm.

Our measurements show that a single interconnect can carry a current of approximately 1.1 mA before electrical breakdown, compared to 0.11 mA for the standard Pt, corresponding to a maximum current density of 1.87×10^7 A cm^{-2} for the carbon-free Pt and 9.44×10^5 A cm^{-2} for the standard Pt. J_{max} for interconnects formed from the carbon-free Pt is two orders of magnitude higher than those formed from the standard Pt precursor, confirming the superiority of $Pt(PF_3)_4$ as a candidate for Pt interconnect formation. Figure 5.4 (b) shows an SEM image of a failed

interconnect where the point of electrical breakdown occurs consistently between electrodes two and three (closer to one than the other) where you would expect to find the least heat dissipation and highest temperature due to Joule heating[34, 35]. Additionally, this fact serves as an indirect indication that the Pt deposition at the edges of the Au/Ni contact lines is conformal, and does not form sharp steps and breakages (often seen for the metal evaporation process) that can result in higher resistivity of the interconnects.

5.3.3 Annealing studies under Nitrogen on deposited Pt

Figure 5.5 (a) shows I-V measurements for a standard Pt interconnect before and after annealing at 400 ^{o}C under nitrogen gas for 1 min. Before annealing, the I-V plot (black) displays perfect ohmic behavior with a resistivity of 115 Ω cm. After annealing, the Pt interconnect demonstrates a resistivity of 93.4 Ω cm. This small decrease in resistivity is possibly due to particles sintering together and a decrease in the impurities content. Previously, annealing in an oxidative atmosphere has been used to purify standard Pt interconnects[15]. This type of a treatment showed decreased interconnect resistivity of about two orders of magnitude in comparison to the as-deposited material but still much higher than bulk Pt, most probably, due to surface oxidation. In contrast to this, N_2 annealed carbon-free Pt demonstrates a much larger decrease in resistance (about 5 times) when compared to the pre-annealed sample (figure 5.5 (b)). This translates into a similar decrease in the resistivity. Taking into account the calculated resistivity using the "true" cross-sectional area of the best performing untreated sample (1.2×10^{-3} Ω cm), the N_2 annealed analogue will show a resistivity of 0.24×10^{-3} Ω cm. If we use the nominal cross-sectional area in calculating the resistivity, this will further decrease the value

to 0.16×10^{-3} Ω cm which is only one order of magnitude higher than bulk Pt and to the best of our knowledge, the lowest reported resistivity for Pt developed by EBID.

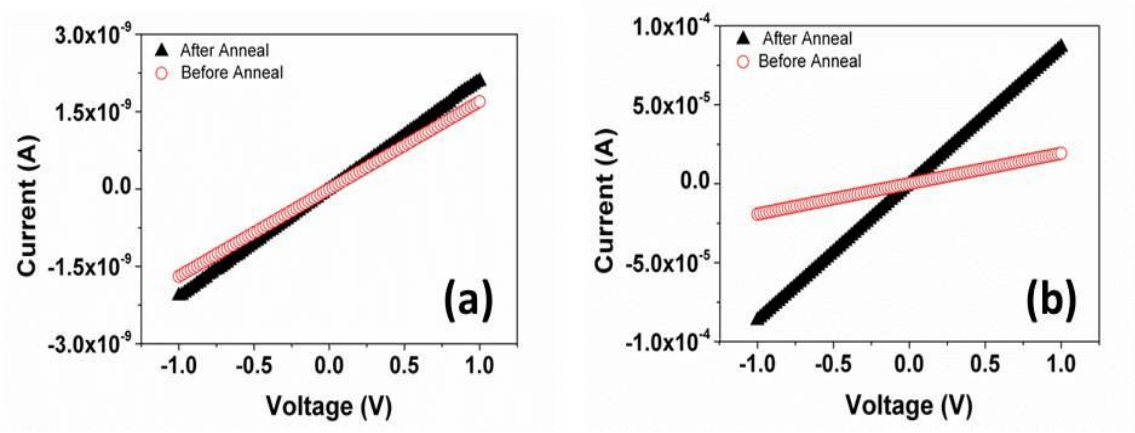


Fig 5.5 I-V measurements of Pt interconnects before and after annealing. (a) I-V curve for a standard Pt interconnect before and after annealing under nitrogen for 1 min. (b) I-V curve for carbon-free Pt interconnect before and after annealing under nitrogen for 1 min.

5.3.4 Annealing Studies under Forming Gas

To explore the effect of a reducing environment on thermal treatment of both types of Pt interconnects, rapid thermal annealing under forming gas was performed at 400 ^{o}C for 1 min. Figure 5.6 (a) shows I-V measurements for a standard Pt interconnect before and after the forming gas anneal. In comparison to the pure N_2 anneals, annealing in the reducing atmosphere introduced changes in the interconnect that decreased the resistivity by about 2 orders of magnitude. Before annealing, the interconnect demonstrated a resistivity of 19.5 Ω cm, while after annealing there is a resistivity of 0.2 Ω cm. This value is one order of magnitude higher than the best reported resistivity for the standard Pt precursor[15] but is still among the lowest values reported. In comparison, the Pt interconnect developed by the carbon-free precursor showing a resistivity of about 1.2×10^{-3} Ω cm before the forming gas annealing, after thermal treatment showed almost no current flow (picoamps range). Additionally,

the interconnect demonstrated electrical behavior that departs severely from typical ohmic I-V behavior (figure 5.6 (b)). These drastically different results can be explained by looking at the integrity of both types of interconnects after annealing. The structure of the Pt interconnects developed by the standard precursor remained smooth and intact on the electrodes (inset in figure 5.6 (a)). TEM images (not shown) show that the overall volume remains the same, even though an increase of the overall Pt particle size is seen. In comparison, the SEM image of the carbon-free Pt interconnect after the forming gas anneal shows that the body of the interconnect is disjointed and broken into separate metal islands. The reason why the carbon-free interconnects broke apart during the forming gas anneal and the standard Pt deposits remained intact can be explained by the dissimilar composition and internal nano-structure of both materials that followed different transformation routes upon forming gas annealing.

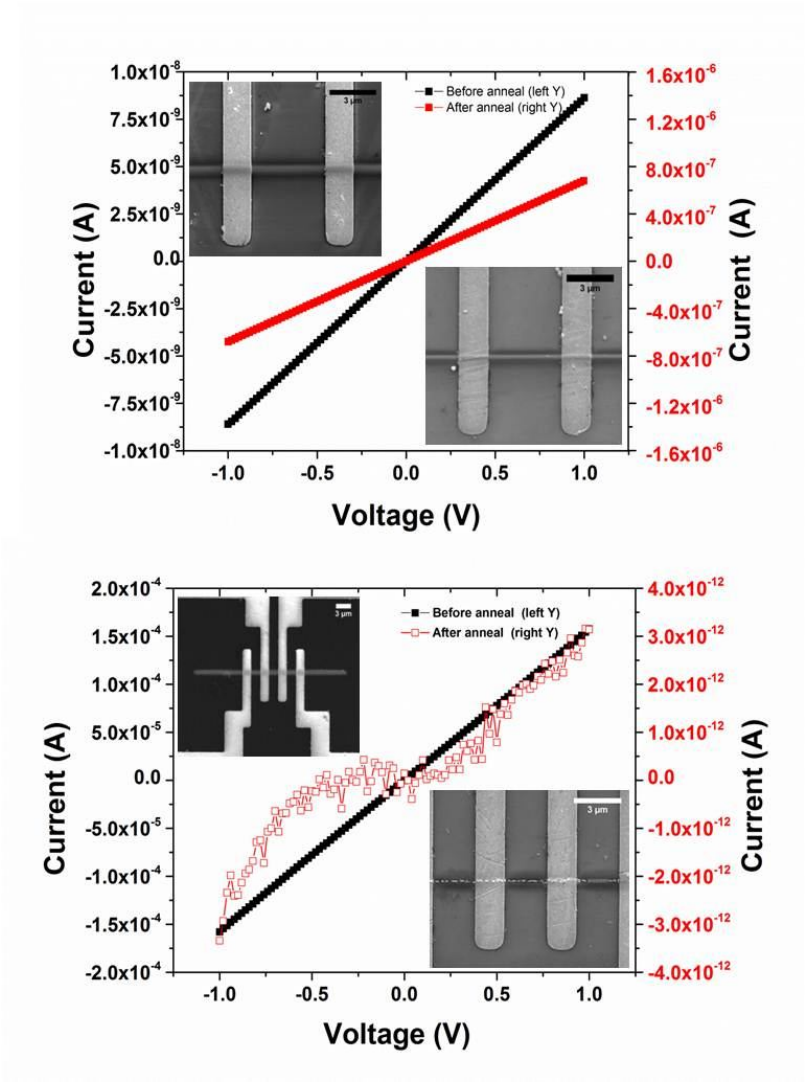


Figure 5.6 I-V measurements of Pt interconnects before and after annealing in forming gas (H_2/Ar). Right (red) Y axis corresponds to current values after annealing. Top and bottom insets in both show Pt wire before and after annealing respectively. Scale bar for insets is 3µm. (a) I-V curve for standard Pt interconnect before and after annealing under H_2/Ar for two minutes. (b) I-V curve for liquid Pt interconnect before and after annealing under H_2/Ar for two minutes.

Normally, when heated under reducing conditions, thin films of noble metals form larger well-faceted and well-crystalline metal nano-crystals in contrast to the materials thermally treated under inert conditions[36]. Evidently, this type of process is happening to a greater extent for the carbon-free deposits. One explanation for this behaviour is that the carbon-free deposits exhibit no amorphous interwoven carbon matrix surrounding the nanoparticles that can keep the structural integrity of

the material and at the same time prevent the formation of larger crystallites. Additionally, previous studies in the literature [37] and our elemental analysis studies (shown below) show that the deposits encompass large phosphorous-containing clusters, which may accelerate the process causing the rest of the structure to break apart. Milder thermal conditions and deposits with minimised phosphorous content might result in preserving the structural integrity of the $Pt(PF_3)_4$ interconnects under forming gas annealing. In comparison, the organometallic Pt deposits are experiencing large improvements in the crystallinty resulting in enhanced electrical performance while the structural integrity is preserved by the surrounding amorphous carbon matrix. We postulate that a valuable route for further enhancement of the electrical performance of the standard Pt deposits can be a two-step annealing process where mild oxidative conditions are used to purify the deposits (decrease the carbon-content) which should be followed by annealing in reducing conditions to improve the grain size and crystallinity of the Pt framework. This two-step procedure is currently under investigation in our group. However, as the work is in its early stages, no significant results have yet been obtained and consequently, have not been presented in this article. Such an investigation is of significant value due to the impressive electrical results obtained thus far and any further enhancement of the electrical performance of carbon-free depositions is highly desirable. Despite this, the two-step procedure would require significant additional experimentation and is therefore beyond the scope of this article.

5.3.5 Elemental and Compositional Analysis of the Carbon-free Pt

As demonstrated previously, the electrical performance of the developed interconnects is a paramount function of the nano-scale structure and composition of the Pt deposits. We and others reported previously, that the carbon-free material deposited via EBID is composed of nanocrystalline Pt particles and an amorphous matrix surrounding the nanoparticles. In order to determine the detailed elemental composition of the interconnects formed from the carbon-free Pt precursor, cross-sections of the Pt wires were obtained and examined by STEM imaging and line-scan EELS analysis (Figures 5.7 (a) and (b)). Line-scan EELS data presented in figure 5.7 (b) depicts the spatial distribution of the elements in a cross-section of a carbon-free Pt deposit before annealing. The elemental content averaged from the signals obtained across the whole section of the deposit are: 61 % Pt, 14 % P, 15 % O and 10 % C. The inclusion of phosphorous in the deposits has already been observed in the form of amorphous material, forming islands of increased phosphorous content along the length of the deposits[33].

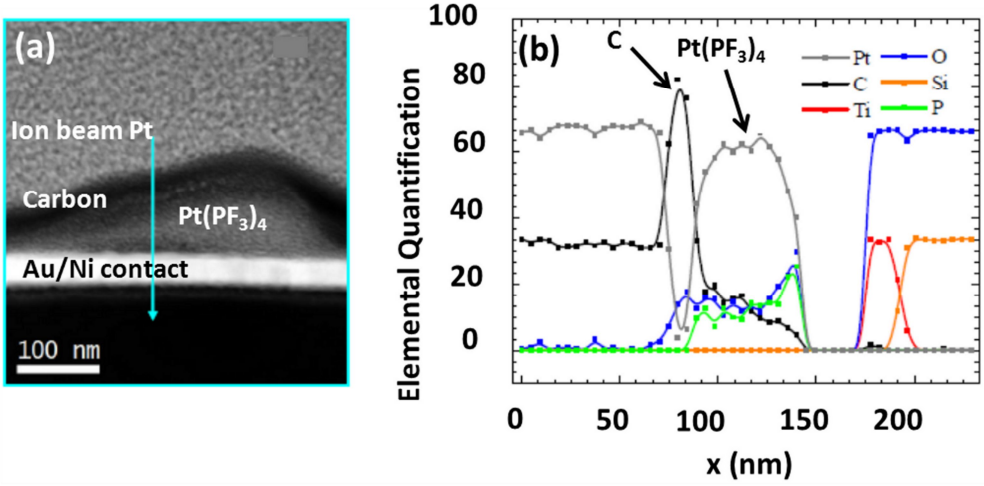


Figure 5.7 Cross-sectional TEM micrograph and EELS analysis of interconnect deposited from $Pt(PF_3)_4$. (a) Low-resolution cross-sectional TEM micrograph of the interconnect deposited on Au/Ni electrode (b) EELS profile taken along the blue arrow shown in (a).

Here, we observe that such islands are formed closer to the bottom of the deposits as seen on Figure 5.7 (b), with elemental content increasing to 20 %. Interestingly, the oxygen profile follows the same trend, reaching 23 % close to the bottom of the deposit. The Pt content is almost constant across the deposit, while carbon content is diminished in the region of higher phosphorous and oxygen content. The origin of the carbon and oxygen inclusion in the deposits cannot be a result of the decomposition of the carbon-free precursor molecules. There are several routes for carbon and oxygen incorporation e.g. (i) from the residual gases in the microscope chamber as the electron beam is scanned during the deposition process, or (ii) from the residual gases during the elemental analysis itself. The latter will be extremely prominent if the samples were left in ambient air for a long time before analysis, adsorbing large amounts of carbon-based contaminants. Oxygen is likely incorporated as a result of exposure to atmospheric conditions after deposition. Finally, it should be noted that the line scan in figure 5.7 (b) shows a higher Pt content in the standard Pt deposited on top of the $Pt(PF_3)_4$ precursor. However, it is important to clarify that this is ion-beam deposited Pt and thus is likely to demonstrate a higher Pt concentration anyway as a result of more efficient cracking of the Pt precursor.

To explore the origin of the carbon content in the deposits, EDX measurements were performed on both carbon-free Pt and standard Pt deposits, without breaking the chamber vacuum. As shown in figure 5.8 and table 1, the EDX point scans were taken at exactly the same conditions on both the interconnect and on the nearby bare substrate to account for the carbon build-up during elemental analysis. As expected, table 1 shows that the carbon content of the interconnects produced using the

standard Pt precursor (C/Si ratio of 1.15 ± 0.1) was almost double that of those produced using the carbon-free Pt precursor (C/Si ratio of 0.57 ± 0.1). Furthermore, the carbon content, measured on the surface of the bare substrate (C/Si ratio of 0.45 ± 0.1) is very close to the content measured for the carbon-free Pt deposit, suggesting that the measured carbon content within the deposits obtained by the Pt $(PF_3)_4$ is solely due to the carbon build-up during the elemental analysis itself. These results also suggest that the carbon content measured by EELS shown in figure 5.7 (b) could be overestimated due to the carbon build-up during analysis. Finally, although fluorine is part of the precursor molecule, its content is below the limit of detection of both EDX and EELS measurements. We speculate that fluorine, being a volatile species, is removed by vacuum during the deposition process and so was not detected during the elemental analysis.

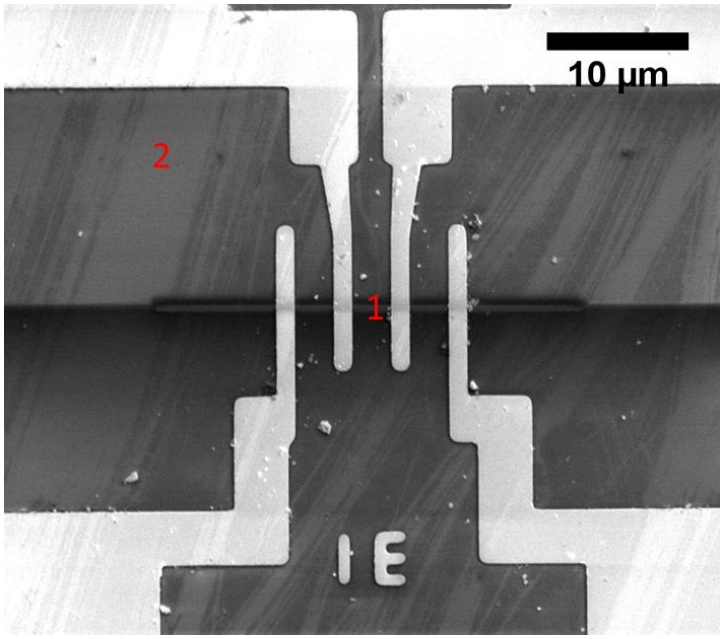


Figure 5.8 SEM micrograph of a carbon-free Pt interconnect deposited on Au/Ni contact pads for EDX analysis. Points 1 and 2 represent the locations of the EDX scans which were taken on both the carbon-free and standard Pt interconnects. Point 1 represents the interconnect while point two is the underlying substrate. The EDX data is given in Table 1 and 2 below.

	C/Si ratio (atomic%)
Standard Pt	1.15 ± 0.1
Carbon-free Pt	0.57 ± 0.1
Substrate	0.45 ± 0.1

Table 1 C/Si atomic ratios before annealing for corresponding Pt interconnect devices and the nearby substrate. The measurements are done on the same chip.

In order to evaluate the composition of the developed Pt interconnects after N_2 annealing, EDX measurements were performed immediately after re-heating the substrate on a hot plate at 120 ^{o}C for 60 mins under atmospheric conditions, taking care that samples are exposed to ambient atmosphere for a very short time after re-heating. Table 2 reveals that the absolute values of the carbon content in the standard and carbon-free precursors have increased after re-heating, most probably due to excessive transient contamination from the laboratory environment.

	C/Si ratio (atomic%)
Standard Pt	3.86± 0.1
Carbon-free Pt	2.21± 0.1
Substrate	2.73± 0.1

Table 2 C/Si atomic ratios after N_2 annealing for corresponding Pt interconnect devices and the nearby substrate. The measurements are done on the same chip.

However, comparing the ratios between the standard Pt and the substrate (1.15:0.45 before annealing and 3.86:2.73 after annealing) we can see an overall decrease in C as the Si remains constant. This conclusion is based on the fact that the difference in

the C/Si ratio calculated from a point measurement on the surface of the Pt deposit and on the bare substrate is less than two fold as it was measured for the samples before annealing (see table 1). As expected for the deposits obtained by the carbon-free Pt material, the carbon content is at similar levels both on the deposits and on the bare substrate (0.57:0.45 before annealing and 2.21:2.73 after annealing). Interestingly, we observed the formation of larger clusters (figure 5.9 (a)) along the length of the interconnect which showed an increase in the phosphorous content. This is probably due to the diffusion of the amorphous material into phosphorus-containing clusters and islands by a process which was enhanced by the thermal treatment. Note that the overall integrity of the interconnects is preserved, in contrast to the samples annealed under forming gas. Figure 5.9 (b) is an EDX spectrum of the carbon-free interconnect shown in figure 5.9 (a). Specifically, it is a point and id scan of one of the clusters highlighted by the white arrows in (a), confirming the presence of P. It is important to quote the melting and boiling points of elemental phosphorous (44 ^{o}C and 280 ^{o}C respectively) as this may provide some insight into the annealing behaviour. The 400 ^{o}C annealing temperature (discussed earlier) is well above both the melting and boiling point of phosphorus. In comparison, the 120 ^{o}C annealing step is below the boiling point and so this difference in temperatures may form the basis of a future investigation into the formation of phosphorous clusters within the carbon-free deposits. Additionally, the possible existence of volatile P-H compounds such as PH_3 (boiling point of -87.7 ^{o}C) may affect the P content of the interconnects through hydrogen contamination. This will prove a useful study in future work, possibly providing a method to further decrease the resistivity of carbon-free Pt contacts.

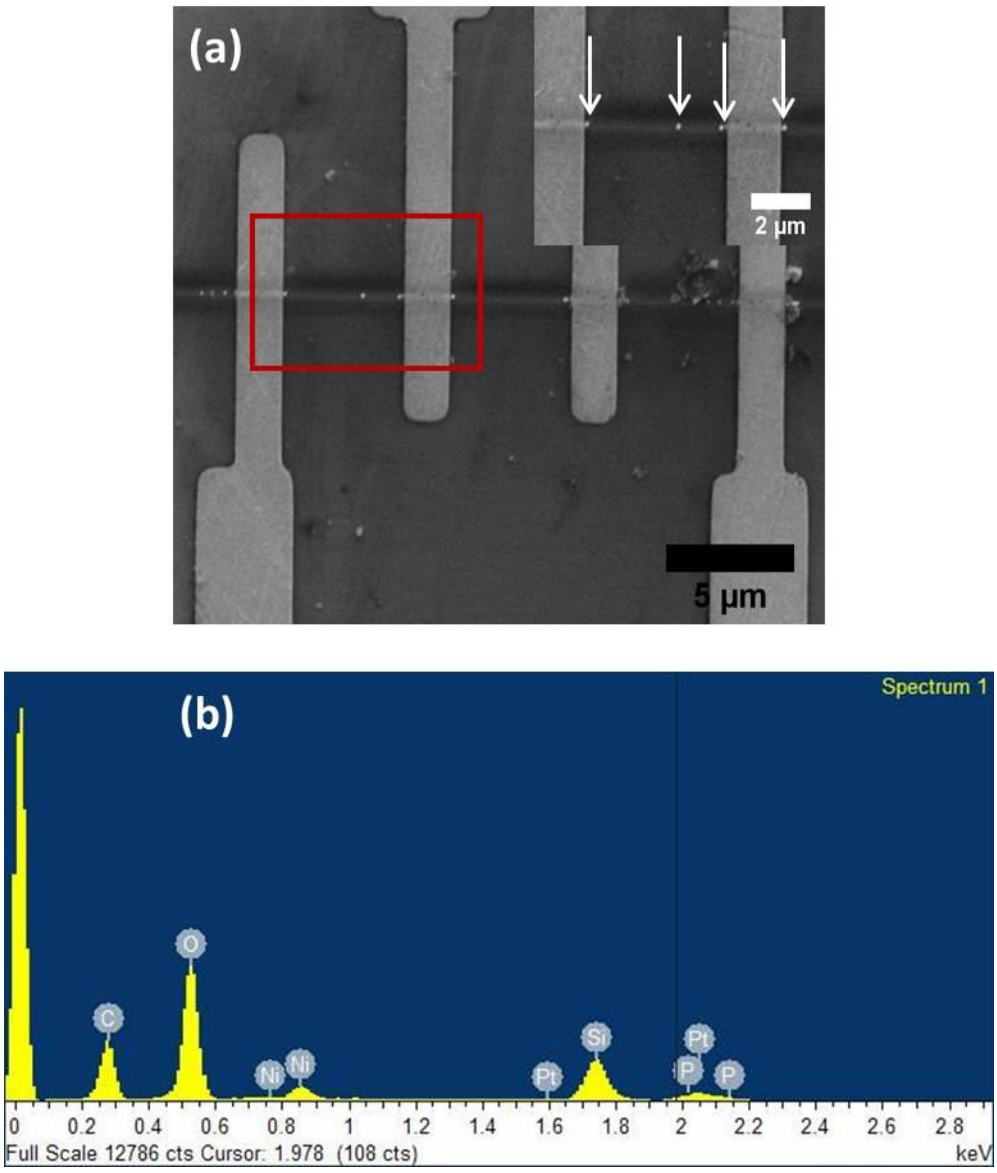


Figure 5.9 (a) SEM micrograph of a carbon-free interconnect deposited on Au/Ni electrodes after additional annealing at 120 ^{o}C for 60 minutes under atmospheric conditions. Inset shows the area highlighted in the red box and illustrates the formation of phosphorous clusters (shown by white arrows) along the length of the interconnect**.** (b) EDX spectrum of the cluster highlighted by the red arrow in (a). The analysis confirms the presence of phosphorous in the clusters. The nickel peaks are from the sample holder in the SEM.

Additionally, in-situ TEM annealing of a deposit formed from the carbon-free Pt precursor on an 80 nm thick silicon nitride membrane was performed. The deposition process on a very thin membrane differs from deposition on a substrate by the amount of deposited material due to the much lower number of secondary

electrons emitted. Moreover, the interaction area of the incoming electron beam with the underlying substrate is minimised and can result in Pt structures as small as several nanometers[38]. Figure 5.10 (a) illustrates the deposition of Pt nanoparticles on the thin silicon nitride membrane, with a size distribution similar to that obtained for the deposits on the $Au/SiO_2/Si$ substrate (the depositions are performed using the same nominal dimensions and conditions). Most importantly, the mean particle diameter for the as-deposited material of 2.7 ± 0.5 nm increases to 3.7 ± 0.7 nm after vacuum annealing at 250 ºC for 10 mins in the TEM (figure 5.10 (b) and (c)). This observation is indicative of coalescence and sintering of the Pt nanoparticles as recently investigated by aberration corrected STEM at room temperature[39]. Theoretical studies predict an increased rate of sintering for nanoscale metal particles in comparison to micron-sized metal powders[40-42]. Furthermore, experimental results demonstrate that metal nanoparticles sinter at temperatures far lower than those predicted from conventional scaling models [43, 44]. Here, we observe Pt nanoparticles sintering at temperatures as low as 250 ºC.

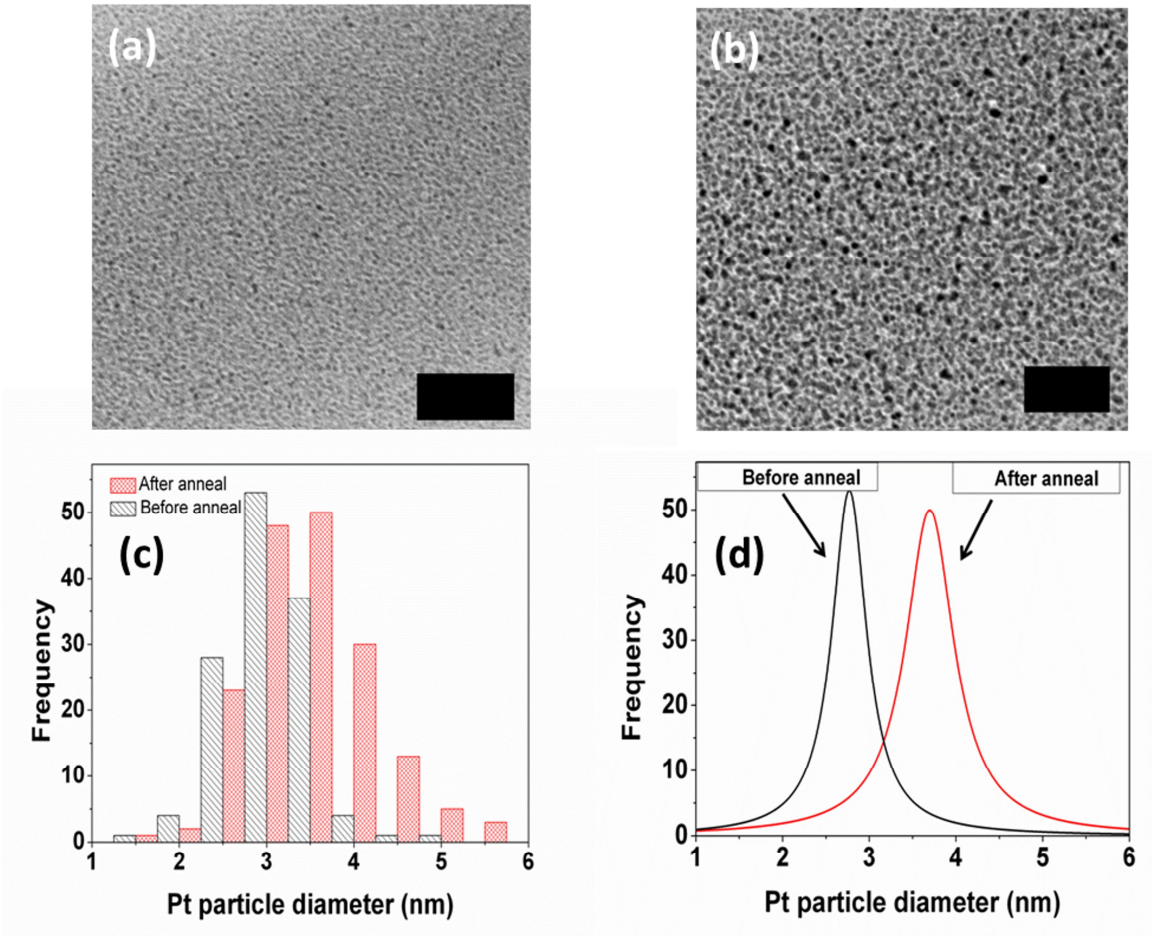


Figure 5.10 Transmission electron micrographs and diameter distributions of platinum particles deposited using $Pt(PF_3)_4$. (a) TEM micrograph of Pt particles before in-situ TEM annealing at 250 ^oC. (b) TEM micrograph of Pt particles after in-situ TEM annealing at 250 ^oC. Scale bars in (a) and (b) are 50 nm. (c) Diameter distribution of Pt particles before and after annealing. The distribution shows a clear increase in particle size after annealing, suggesting the sintering of particles together which can be correlated to the decrease in resistivity after annealing. (d) Lorentzian fit to the distribution in (c), which highlights the difference in particle sizes more clearly.

Most significantly, the obtained in-situ annealing data, together with the elemental analysis before and after N_2 annealing, are important in understanding the decreased resistivity of the interconnects after annealing and the obtained high break-down currents. Increased conductivity of several orders of magnitude in ink-jet printed nanoparticulate Ag interconnects has been attributed to increased particle size by

electrical sintering[45]. Similarly, our interconnects increase their conductivity by applying higher potential until break-down at which point the interconnect is transformed into large isolated islands of Pt. This behavior is likely due to localized Joule heating. A method for determining the spatial distribution of the temperature gradients due to Joule heating around a metal-containing interconnect on a silicon nitride membrane has been demonstrated[46]. Their results indicated the formation of larger metallic nanoparticles as a function of the applied electrical power. Our results suggest that the Pt interconnects developed from the carbon-free precursor show improved performance after N_2 annealing mainly due to nanoparticle sintering, improved crystallinity and locally minimised amorphous impurities.

5.4 Conclusions

Pt interconnects deposited from the carbon-free precursor, $Pt(PF_3)_4$, using EBID demonstrated very low resistivities compared to interconnects produced using a standard Pt precursor. After devising two different annealing procedures and measuring the "true" cross-sectional area of the interconnects, we demonstrate that low resistivity Pt interconnects showing resistivities of about 0.24×10^{-3} Ω cm and 0.2 Ω cm can be obtained for the carbon-free and standard precursors, respectively. A maximum current density (J_{max}) of 1.87×10^{7} A cm^{-2} was achieved for the $Pt(PF_3)_4$ precursor. This was 2 orders of magnitude higher than the maximum current density achieved for the standard $(CH_3)_3Pt(C_pCH_3)$ precursor. Additionally, the enhanced electrical properties of the as-deposited carbon-free Pt materials are explained by the absence of large amounts of carbon impurities, and their further improvement by post-deposition annealing under inert gases. N_2 annealing of these interconnects proved very effective at lowering their resistivity. In comparison interconnects formed from the standard Pt precursor demonstrated an improvement in resistivity of 2 orders of magnitude after annealing in forming gas. Our in-situ TEM results and elemental composition studies suggest that the Pt interconnects developed from the carbon-free precursor show improved performance after N_2 annealing mainly due to nanoparticle sintering, improved crystallinity and locally minimised amorphous impurities. Due to the higher current density and lower resistivity of Pt interconnects formed from the carbon-free Pt precursor, in comparison to the structures formed from the standard Pt precursor, the $Pt(PF_3)_4$ is likely to become a preferred precursor for EBID deposition of Pt metal for fast and effective prototyping of devices.

5.5 References

(1) Contreras, A. M.; Grunes, J.; Yan, X.; Liddle, A.; Somorjai, G. A. *Catal. Lett.* **2005,** 100, 115.

(2) Drouin, D.; Beauvais, J.; Lemire, R.; Lavallée, E.; Gauvin, R.; Caron, M. *Appl.Phys. Lett.* **1997,** 70, 3020.

(3) Jin, S.; Whang, D.; McAlpine, M. C.; Friedman, R. S.; Wu, Y.; Lieber, C. M. *Nano Lett*. **2004,** 4, 915.

(4) Gopal, V.; Radmilovic, V. R.; Daraio, C.; Jin, S.; Yang, P.; Stach, E. A. *Nano Lett*. **2004,** 4, 2059.

(5) Wang, D.; Wang, Q.; Javey, A.; Tu, R.; Dai, H.; Kim, H.; McIntyre, P. C.; Krishnamohan, T.; Saraswat, K. C. *Appl. Phys. Lett*. **2003,** 83, 2432.

(6) Zhang, L.; Tu, R.; Dai, H. J. *Nano Lett.* **2006,** 6, 2785.

(7) Andzane, J.; Petkov, N.; Livshits, A. I.; Boland, J. J.; Holmes, J. D.; Erts, D. *Nano Lett*. **2009,** 9, 1824.

(8) Ziegler, K. J.; Lyons, D. M.; Holmes, J. D.; Erts, D.; Polyakov, B.; Olin, H.; Svensson, K.; Olsson, E. *Appl. Phys. Lett.* **2004,** 84, 4074.

(9) Kim, P.; Lieber, C. M. *Science* **1999,** 286, 2148.

(10) Kinaret, J. M.; Nord, T.; Viefers, S. *Appl. Phys. Lett*. **2003,** 82, 1287.

(11) Mazeina, L.; Perkins, F. K.; Bermudez, V. M.; Arnold, S. P.; Prokes, S. M. *Langmuir* **2010,** 26, 13722.

(12) Arnold, D. C.; Hobbs, R. G.; Zirngast, M.; Marschner, C.; Hill, J. J.; Ziegler, K. J.; Morris, M. A.; Holmes, J. D. *J. Mater. Chem*. **2009,** 19, 954.

(13) Cacouris, T.; Krchnavek, R. R.; Gilgen, H. H.; Osgood Jr, R. M.; Kulick, S.; J. Schoen, (IEEE, 1985), 594.

(14) Silvis-Cividjian, N.; Hagen, C. W.; Kruit, P.; vd Stam, M. A. J.; Groen, H.

B. *Appl. Phys. Lett.* **2003,** 82, 3514.

(15) Botman, A.; Mulders, J. J. L.; Weemaes, R.; Mentink, S. *Nanotechnology* **2006,** 17, 3779.

(16) Utke, I.; Hoffmann, P.; Dwir, B.; Leifer, K.; Kapon, E.; Doppelt, P. *J. Vac. Sci. Technol. B* **2000,** 18, 3168.

(17) Nam, C. Y.; Kim, J. Y.; Fischer, J. E.; *Appl. Phys. Lett.* **2005,** 86, 193112.

(18) Tao, T.; Ro, J. S.; Melngailis, J.; Xue, Z.; Kaesz, H. D. *J. Vac. Sci. & Technol.B* **1990,** 8, 1826.

(19) Cronin, S. B.; Lin, Y. M.; Rabin, O.; Black, M. R.; Ying, J. Y.; Dresselhaus, M. S.; Gai, P. L.; Minet, J. P.; Issi, J. P. *Nanotechnology* **2002**, 13, 653.

(20) Ho, C. Y.; Chiu, S. H.; Ke, J. J.; Tsai, K. T.; Dai, Y. A.; Hsu, J. H.; Chang, M. L.; He, J. H. *Nanotechnology* **2010,** 21, 134008.

(21) Vieu, C.; Carcenac, F.; Pepin, A.; Chen, Y.; Mejias, M.; Lebib, A.; Manin Ferlazzo, L.; Couraud, L.; Launois, H. *Appl. Surf. Sci*. **2000,** 164, 111.

(22) Hochbaum, A. I.; Chen, R.; Delgado, R. D.; Liang, W.; Garnett, E. C.; Najarian, M.; Majumdar, A.; Yang, P.; *Nature* **2008,** 451, 163.

(23) Qi, C.; Goncher, G.; Solanki, R.; Jordan, J. *Nanotechnology* **2007,** 18, 075302.

(24) He, J. H.; Chang, P. H.; Chen, C. Y.; Tsai, K. T.; *Nanotechnology* **2009,** 20, 135701.

(25) Nam, C. Y.; Tham, D.; Fischer, J. E. *Nano Lett.* **2005,** 5, 2029.

(26) Hanrath, T.; Korgel, B. A. *Proc. Inst. Mech. Eng. N J. Nanoeng. Nanosyst.* **2004,** 218, 25.

(27) Thompson, K.; Lawrence, D.; Larson, D. J.; Olson, J. D.; Kelly, T. F.; Gorman, B. *Ultramicroscopy* **2007,** 107, 131.

(28) Ervin, M. H.; Chang, D.; Nichols, B.; Wickenden, A.; Barry, J.; Melngailis, J. *J. Vac. Sci. Technol. B* **2007,** 25, 2250.

(29) Allan, M. *J. Chem. Phys.* **2011,** 134, 204309.

(30) Takeguchi, M.; Shimojo, M.; Furuya, K. *Appl. Phys. A.* **2008,** 93, 439.

(31) Giannuzzi L. A.; Stevie, F. A. *Micron* **1999,** 30, 197.

(32) Dias, R. J.; O'Regan, C.; Thrompenaars, P.; Romano-Rodriguez, A.; Holmes, J. D.; Mulder, J. J. L. H.; Petkov, N. *J. Phys.: Conf. Ser.* **2012,** 371, 012038.

(33) Barry, J. D.; Ervin, M.; Molstad, J.; Wickenden, A.; Brintlinger, T.; Hoffman, P.;Meingailis, J. *J. Vac. Sci. Technol B* **2006,** 24, 3165.

(34) Lin, Y. C.; Lu, K. C.; Wu, W. W.; Bai, J.; Chen, L. J.; Tu, K. N.; Huang, Y. *Nano Lett.* **2008**, 8, 913.

(35) Wu, Y.; Xiang, J.; Yang, C.; Lu, W.; Lieber, C. M. *Nature* **2004,** 430, 61.

(36) Kang, C. Y.; Chao, C.; Shiu, H. S. C.; Chou, L. J.; Chang, M. T.; Lin, G. R.; Lin, C. F. *J. Appl. Phys.* **2007,** 102, 073508.

(37) Botman, A.; Hesselberth, M.; Mulders, J. J. L. H. *J. Vac. Sci. Technol. B.* **2008,** 26, 2464.

(38) van Dorp, W. F.; van Someren, B.; Hagen, C. W.; Kruit, P.; Crozier, P. A. *Nano Lett.* **2005** 5, 1303.

(39) Asoro, M. A.; Kovar, D.; Shao-Horn, Y.; Allard, L. F.; Ferreira, P. J. *Nanotechnology* **2010,** 21, 025701.

(40) Herring, C. *J. Appl. Phys.* **1950,** 21, 301.

(41) Coble, R. L. *J. Am. Ceram. Soc.* **1958,** 41, 55.

(42) Kingery W. D.; Berg, M. *J. Appl. Phys.* **1955,** 26, 1205.

(43) Groza, J. R. *Nanostruct. Mater.* **1999,** 12, 987.

(44) Champion, Y.; Bernard, F.; Guigue-Millot, N.; Perriat, P. *Mater. Sci. Eng., A*

2003, 360,258.

(45) Allen, M. L.; Aronniemi, M.; Mattila, T.; Alastalo, A.; Ojanperä, K.; Suhonen, M.; Seppä, H. *Nanotechnology* **2008,** 19, 175201.

(46) Reguer, A.; Bedu, F.; Nitsche, S.; Chaudanson, D.; Detailleur, B.; Dallaporta, H. *Ultramicroscopy* **2009,** 110, 61.

.

Conclusions

6

Ge nanowires have been the subject of intense research over the last few decades, due to the unique properties they exhibit as a result of their one-dimensional nature [1-3]. In order for these structures to be utilised to their full potential, their growth behaviour needs to be completely understood; being able to control nanowire dimensions during growth will facilitate the integration of these structures into device applications.

The Lieber group first demonstrated that semiconducting nanowires can be integrated into functional optoelectroninc and electronic applications such as lasers [4], logic gates [5] and memory devices [6]. Each of these devices requires conductive electrical contacts to the nanowires. Consequently, research into nanowire interconnects is vital in order to understand how these structures can be connected in nanoscale applications[7-9]. In particular, interconnects with low electrical resistivity are very desirable for nanowire applications [9]. The data reported in this thesis has demonstrated both the growth and kinetic adjustment of Ge nanowire aspect ratios, as well as the characterisation of Pt interconnects, which may be utilised in the future to connect such nanowires for nanoscale device integration.

Chapter 1 reviewed the most significant progress made in Ge nanowire growth over the last 6-7 years. Specifically, the chapter discussed the aspects that are most crucial to nanowire growth in terms of dimensional control; including the growth methods themselves, growth kinetics and thermodynamics and the control of nanowire morphology.

Chapter 2 summarised the experimental methods employed to synthesise and characterise Ge nanowires. Liquid injection chemical vapor deposition (LICVD) was the method of choice for nanowire synthesis due to its facile methodology and

its ability to control nanowire dimensions via a vapour-liquid-solid (VLS) mechanism. Characterisation techniques used in this study included SEM, FIB, TEM (including bright-field, dark-field, and in-situ heating TEM), EDX and UV-Vis absorbance spectroscopy. Additionally, the methods of fabricating and characterising (both electrically and structurally) Pt interconnects via EBID of $Pt(PF_3)_4$ and $(CH_3)_3Pt(C_pCH_3)$ was outlined.

Chapter 3 detailed the growth and characterisation of Ge nanowires which were synthesised from Au/Ge bi-layer films. Specifically, the length and growth rates of the nanowires were tuned by increasing the thickness of the Ge layer in the bi-layer part of the substrate. The resulting nanowire growth was directly compared with standard Au-seed mediated growth on the same substrate. Longer nanowires with uniform diameters and orientations increased the aspect ratios of the Ge nanowires, which is desirable for maximising their potential applications in device architectures. This chapter presented SEM results which clearly conveyed the difference in growth regimes on both sides of the 2-part substrate (Au/Ge bi-layer and Au). Additionally, the kinetic studies and analysis of the binary alloy seeded nanowires were supported by electron microscopy studies; including in-situ TEM heating experiments on the Au/Ge bi-layers. The method of increasing the solute concentration in the Au/Ge binary alloy using bi-layer films opens up the possibility of engineering the growth of Ge nanowires (and thus tuning of nanowire properties) for future devices. A possible avenue for future work in this area would be the application of Ge substrates to grow epitaxial Ge nanowires from Au/Ge bi-layer films. Epitaxial substrates would produce aligned nanowires of a uniform orientation (determined by the crystallographic orientation of the substrate) and would also facilitate easier determination of nanowire length and growth rates, as the nanowires would no

longer be entangled in a mesh on the substrate surface. Additional future work might include the use of bi-layer films to manipulate the supersaturation of Ge in the Au/Ge alloy in combination with other critical growth parameters, *i.e.* pressure, temperature, dopant concentration, precursor decomposition chemistry *etc*. to realise nanowires with tunable properties.

Chapter 4 extended the work of Chapter 3 by introducing Ag as a foreign element into the Au/Ge alloy system in order to reduce the equilibrium concentration of Ge. The solute concentration was also increased through the use of Ge films. Simultaneously altering both parameters in the Au/Ag/Ge ternary alloy system [10-12], through the use of a Au/Ag/Ge tri-layer, increased the length and growth rate of Ge nanowires to a greater extent than what was observed in Chapter 3. A bi-modal diameter distribution was observed for nanowires grown from these tri-layers, which was subsequently removed through the use of $Au_{0.75}Ag_{0.25}$ nanoparticles deposited on a Ge film, yielding nanowires with more uniform diameters. Diameter dependent properties of the Ge nanowires as a result of the Gibbs-Thomson effect were also investigated and these were supported using in-situ TEM heating of nanowires in order to calculate the equilibrium concentration, as a function of diameter from the alloy seed expansion. The combination of adding a Ge film to increase the solute concentration in the Au/Ge system (while also reducing the equilibrium concentration through the incorporation of Ag) and using monodisperse alloy nanoparticles with uniform diameters deposited onto a Ge buffer layer to synthesise Ge nanowires may yield a highly ideal growth scenario in future work, when combined with other growth kinetic influencing parameters such as temperature and pressure. As with the data presented in Chapter 3, future work in this area could include the application of Au/Ag alloy particles to produce epitaxially grown

nanowires from Ge substrates. As the lengths and growth rates would be more easily determined compared to the non-epitaxial wires achieved in this work, the error associated with such distributions and the Gibbs-Thomson arguments would be less significant.

Chapter 5 presented the electrical and structural characterisation of Pt interconnects deposited using the carbon-free precursor $Pt(PF_3)_4$ [13-15]. This precursor has the potential of becoming the standard chemical for the fabrication of Pt interconnects for future nanowire based devices. There was minimal carbon content present in the resulting deposits, which translates into much improved resistivity [9] and maximum current density, when compared to interconnects deposited via the standard organometallic precursor, $(CH_3)_3Pt(C_pCH_3)$ [16]. Additionally, post-deposition annealing of the interconnects further improved their electrical performance and in-situ TEM annealing of the interconnects suggested that this improved performance was due to nanoparticle sintering and locally minimised amorphous impurities. Due to the much improved resistivity and minimal carbon content, this carbon-free precursor is likely to become the preferred choice for the EBID of Pt metal for the contacting of Ge nanowires with controlled dimensions, which has been detailed in Chapters 3 and 4. Future work would be concerned with further decreasing the resistivity of the carbon-free interconnects through additional annealing experiments in different atmospheres. Moreover, the investigation of different currents and device dimensions (both of which can be controlled directly via EBID with a focused electron beam) for precursor deposition would be useful in determining the ideal conditions to maximise conductivity in the resulting interconnects.

References

(1) Cui, Y.; Lieber, C. *Science* **2001,** 291, 851.

(2) Huang, Y.; Lieber, C. *Pure. Appl. Chem.* **2004,** 76, 2051.

(3) Barth, S.; Hernandez-Ramirez, F.; Holmes, J. D.; Romano-Rodriguez, A. *Prog. Mater. Sci.* **2010,** 55, 563.

(4) Duan, X.; Huang, Y.; Agarwal, R.; Lieber, C. M. *Nature* **2003,** 421, 241.

(5) Huang, Y.; Duan, X.; Cui, Y.; Lauhon, L.; Kim, K.; Lieber, C. *Science* **2001,** 294, 1313.

(6) Duan, X.; Huang, Y.; Lieber, C. *Nano Lett.* **2002,** 2, 487.

(7) Contreras, A.; Grunes, J.; Yan, X. M.; Liddle, A.; Somorjai, G. *Catal. Lett.* **2004,** 100.

(8) Jin, S.; Whang, D.; McAlpine, M. C.; Friedman, R. S.; Wu, Y.; Lieber, C. M. *Nano Lett.* **2004,** 4, 915.

(9) Botman, A.; Hesselberth, M.; Mulders, J. J. L. *J. Vac. Sci. Technol. B* **2008,** 26, 2464.

(10) Borzone, G.; Hassam, S.; Bros, J. *Metall. Mater. Trans. A* **1989,** 20, 2167.

(11) Wang, J.; Liu, Y. J.; Tang, C. V.; Liu, L. B.; Zhou, H. Y.; Jin, Z. P. *Thermochim. Acta.* **2011,** 512, 240.

(12) Chou, Y.-C.; Wen, C.-Y.; Reuter, M. C.; Su, D.; Stach, E. A.; Ross, F. M. *ACS Nano* **2012,** 6, 6407.

(13) Ervin, M. H.; Chang, D.; Nichols, B.; Wickenden, A.; Barry, J.; Melngailis, J. *J. Vac. Sci. Technol. B* **2007,** 25, 2250.

(14) Allan, M. *J. Chem. Phys.* **2011,** 134, 204309.

(15) Takeguchi, M.; Shimojo, M.; Furuya, K. *Appl. Phys. A* **2008,** 93, 439.

(16) Botman, A.; Mulders, J. J. L.; Weemaes, R.; Mentink, S. *Nanotechnology* **2006,** 17, 3779.

Appendix - Dissemination

Publications

O'Regan, C.; Lee, A.; Trompenaars, P.; Mulders, H.; R. J.; Holmes, J. D.; Petkov, N. "Electrical properties of platinum interconnects deposited by electron beam induced deposition of the carbon-free precursor, $Pt(PF_3)_4$". *J. Vac. Sci. Technol. B* **2013,** 31, 021807(1)-021807(8). (***Chapter 5)***

O'Regan, C.; Biswas, S.; O'Kelly, C.; Jung, S.J.; Boland, J.J.; Petkov, N.; Holmes, J.D. "Engineering the Growth of Germanium Nanowires by Tuning the Supersaturation of the Au/Ge Binary Alloy Catalyst". *Chem. Mater.* **2013,** 15, 3096. ***(Chapter 3)***

O'Regan, C.; Biswas, S.; Petkov, N.; Holmes, J.D. "Controlled Growth of Germanium Nanowires from Ternary Alloy Catalysts". In preparation. ***(Chapter 4)***

O'Regan, C.; Biswas, S.; Petkov, N.; Holmes, J.D. "Recent Advances in the Growth of Germanium nanowires: Synthesis, Growth Dynamics and Morphology Control". ". *J. Mater. Chem. C*, **2013**, DOI: 10.1039/C3TC31736F ***(Chapter 1)***

Varghese, J.; **O'Regan, C.;** Petkov, N.; Deepak, N.; Whatmore, R.W.; Holmes, J.D.; "Surface roughness assisted growth of vertically oriented ferroelectric SbSI nanorods" *Chem. Mater.* **2012**, 24, 3279−3284

Biswas, S.; **O'Regan, C**.; Petkov, N.; Morris, M. A.; Holmes, J. D. 'Manipulating the growth kinetics of vapor-liquid-solid propagated Ge nanowires'. *Nano. Lett.* **2013**, 13 (9):4044-4052

Biswas, S.; **O'Regan, C**.; Morris, M.A.; Holmes, J.D. "Exploring Nanosize effects for Vapour-Liquid-Solid Nanowire Growth with Binary and Ternary Eutectic Alloys". In preparation.

Dias, R.J.; **O'Regan**, **C.;** Thrompenaars, P.; Romano-Rodriguez, A.; Holmes, J.D.; Mulder, J.J.L.; and Petkov, N. "Low resistivity Pt interconnects developed by electron beam assisted deposition using novel gas injector system", *J. Phys.: Conf. Ser.* **2012,** 371, 012038

Armstrong, M. J.; Paneerselvam, A.; **O'Regan, C.**; Morris, M. A.; Holmes, J. D. "Supercritical-fluid synthesis of FeF2 and CoF2 Li-ion conversion materials". *J. Mater. Chem. A*, **2013,** 1, 10667.

Armstrong. M. J.; Burke, D. M.; Gabriel, T.; **O'Regan, C**.; O'Dwyer, C.; Petkov, N.; Holmes, J. D. 'Carbon nanocage supported synthesis of V2O5 Nanorods and V2O5/TiO2 Nanocomposites for Li-ion Batteries'. *J. Mater. Chem. A*, **2013** 1 (40):12568-12578..

Lotty, O.; Hobbs, R.; **O'Regan, C**.; Hlina, J.; Marschner, C.; O'Dwyer, C.; Petkov, N.; Holmes, J. D. "Self-seeded Growth of Germanium Nanowires: Coalescence and Ostwald Ripening". *Chem. Mater.* **2013,** 25, 215.

Varghese, J.; Ghoshal, T.; Deepak, N.; **O'Regan, C**.; Whatmore, R. W.; Morris, M. A.; Holmes, J. D. "Fabrication of arrays of PZT nanodots via block copolymer self-assembly". *Chem. Mater.* **2013,** 25, 1458.

Presentations

Electron Microscopy and Analysis Group (EMAG) conference, Birmingham, September 2011, *"In-situ Temperature Dependent Studies of the Au/Ge Nanowire Nucleation, Metal/Ge Nanowire Contact Formation and Ge Nanowire Surface Faceting"*

Microscopy Society of Ireland (MSI) Symposium, Cork, Ireland, August 2012. *"Electron Microscopy of Nanoscale Materials"*

European Materials Research Society (EMRS) Spring Meeting, May 2013, "*Engineering the Growth of Germanium Nanowires by Tuning the Supersaturation of the Au/Ge Binary Alloy Catalyst"*

Posters

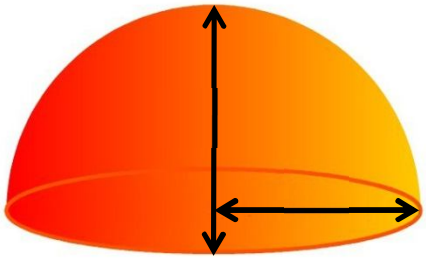
Advanced Materials and Technologies Summer School, Palanga Lithuania, August 2010, *"Electron Microscopy Analysis of Nanoscale Materials"*

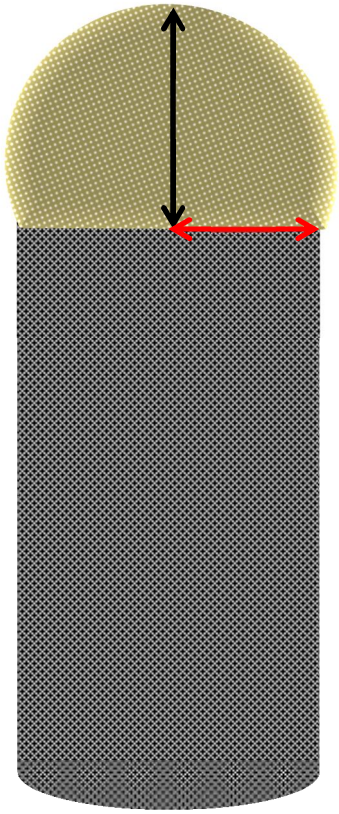
Nanoweek Conference, Kildare Ireland, Jan 2011, *"Electron Microscopy Analysis of Nanoscale Materials"*

MRS Spring Meeting, San Francisco, April 2012, *"Diameter Controlled Germanium Nanowires Grown From Au/Ge Bi-layer Films"*

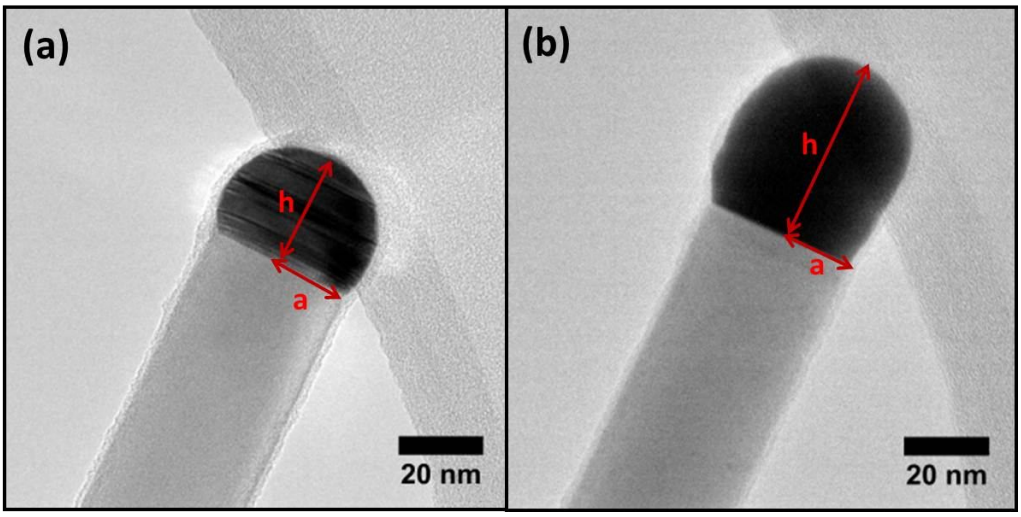
Appendix 2 – Calculation of Ge atomic %

These calculations follow the general method outlined by Sutter *et al.*[1, 2]





Taking **h** as the height of the particle and **a** as the radius before expansion (Figure 1 (a)), we first use the formula for the volume of a hemispherical cap to calculate the volume of Au in the seed particle:



As an example, taking **a** as 54.525 and **h** as 54.97, we can input these values into the equation:

$$V\,(RT) = \frac{\pi}{6} \times (54.97) \times [3(54.525)^2 + (54.97)^2] = 343677$$

Multiplying this by 53.21 (takes into account density and atomic number of Au) to calculate the number of Au atoms:

$$N_{Au} = 343677 \times 53.21 = 18287097$$

Next, we calculate the volume of the particle <u>after</u> expansion due to heating to the growth temperature of 480 ^{o}C (figure 1 (b)), using the same formula:

$$V\,(480\,^{o}C) = \frac{\pi}{6} \times (80.81) \times [3(50.68)^2 + (80.81)^2] = 598062$$

Hence, the expansion volume due to Ge uptake is:

$$598062 - 343677 = 254385$$

Hence, the amount of Ge atoms:

$$N_{Ge} = 254385 \times 45.54 = 11584692.9$$

Finally:

$$At\%\ Ge = \frac{N_{Ge}}{(N_{Au} + N_{Ge})} \times 100$$

$$= \mathbf{38.78}\ \%$$

The above calculation was performed for a nanowire from the Au/Ge system with a diameter of 97 nm. It is repeated for several nanowires of varying diameters for both the Au/Ge and Au/Ag/Ge system.

References

(1) Sutter, E. A.; Sutter, P. W. *ACS Nano* **2010,** 4, 4943.

(2) Sutter, E.; Sutter, P. *Nano Lett.* **2008,** 8, 411.